

# **Application of Tissue Equivalent Proportional Counter (TEPC) in Intercalibration with NaI (Tl) Spectrometer**

- Part of the Cosmic-ray Dose Monitoring Network Project with Health Canada's Fixed Point  
Surveillance (FPS) Network

By

Haiqian Ma

A thesis submitted to Faculty of Graduate and Postdoctoral Affairs  
in partial fulfillment of the requirements for the degree of

Master of Science

in

Particle Physics

Carleton University

Ottawa, Ontario

© 2021, Haiqian Ma

## ABSTRACT

---

Name: Haiqian Ma

Date: September 29, 2021

Application of Tissue Equivalent Proportional Counter (TEPC) in Intercalibration with NaI (TI) Spectrometer

- Part of the Cosmic-ray Dose Monitoring Network Project with Health Canada's Fixed Point Surveillance (FPS) Network

Tissue equivalent proportional counters (TEPCs) are recognized as the standard instrument for cosmic radiation dose measurement because they can separate gamma and neutron spectra in mixed field microdosimetry. HAWK TEPC was employed in the project as a reference instrument to measure the cosmic radiation exposure in terms of dose equivalent and ambient dose equivalent ( $H^*(10)$ ) at ground level, calibrate and compare the analytical doses calculated from the overflow channel of Canada's Fixed Point Surveillance (FPS) spectrometers. The TEPC performance has been investigated, and side-by-side measurements between HAWK and FPS detectors have been conducted at eight different locations. Experimental  $H^*(10)$  obtained with TEPC is consistent with the analytical dose results; the minimum and maximum discrepancies are 3.8 % and 26.7 % respectively. The work will be further evaluated and applied to other FPS stations.

## ACKNOWLEDGMENTS

---

First, I would like to express my sincere appreciation to my supervisor, Dr. Weihua Zhang, for his guidance and dedicated involvement at every stage of the research project. I would also like to thank my co-supervisor, Dr. Tong Xu for his invaluable support and encouragement through my undergraduate and graduate study; his insightful feedback takes my work to the next level. Their mentorship and confidence in me were significant to my research growth. Special thanks to Dr. Chuanlei Liu for being critical of my data analysis and driving me to improve everything and dig deep into the underlying physics of cosmic rays and the TEPC detector. I would like to extend my thanks to Dr. Kurt Ungar and Dr. Eric Pellerin for providing me with the opportunity to work on such an exciting topic. I would like to thank Dr. Ron Miller and Dr. Jesse Heilman for being my thesis examiners, thank you for their valuable feedback. This work would have been impossible without their support.

I would like to acknowledge the funding supporting the thesis research from Carleton University and Health Canada. I would like to make a special acknowledgment to the Royal Military College of Canada (RMC), Dr. Brent Lewis and Dr. Paul Chan, for their help, advice, software, and the HAWK TEPC device provided to us through the courtesy. In addition, I would like to thank Dr. Aslam Ibrahim from Canadian Nuclear Safety Commission for assisting in the neutron calibration during the provincial lock-down. I extend my gratitude to the technical support from Dr. Thomas Conroy from Far west technology and Dr. F. Hennig from XIA technology.

To my beautiful family,

thank you for your continuous encouragement, unconditional support, and unwavering love throughout all these years.

# TABLE OF CONTENTS

---

ABSTRACT .....	2
ACKNOWLEDGMENTS .....	3
LIST OF TABLES .....	7
LIST OF FIGURES .....	9
EQUATIONS .....	13
LIST OF APPENDICES .....	16
NOMENCLATURE .....	17
ACRONYMS .....	18
<b>1 INTRODUCTION .....</b>	<b>19</b>
<b>1.1 NATURAL BACKGROUND RADIATION AND COSMIC RAY .....</b>	<b>19</b>
<b>1.2 PHYSICAL ASPECTS .....</b>	<b>23</b>
1.2.1 <i>Protection and Operational Quantity</i> .....	23
1.2.2 <i>Linear Energy Transfer (LET) and Lineal Energy (y)</i> .....	24
<b>1.3 TISSUE EQUIVALENT PROPORTIONAL COUNTER (TEPC).....</b>	<b>28</b>
<b>1.4 HEALTH CANADA'S FIXED POINT SURVEILLANCE (FPS) NETWORK.....</b>	<b>34</b>
1.4.1 <i>Introduction to FPS</i> .....	34
1.4.2 <i>FPS Spectrometer (RS250) and the Analytical Model</i> .....	37
<b>1.5 OBJECTIVES .....</b>	<b>41</b>
<b>1.6 SUMMARY OF THE CONTENTS OF THIS WORK.....</b>	<b>42</b>
<b>2 TEPC DATA PROCESSING AND ANALYSIS.....</b>	<b>43</b>
<b>2.1 INTRODUCTION TO HAWK TEPC.....</b>	<b>43</b>
2.1.1 <i>Introduction to HAWK TEPC</i> .....	43
2.1.2 <i>Detector Specification</i> .....	45
<b>2.2 DATA ANALYSIS .....</b>	<b>47</b>
<b>2.3 UNCERTAINTIES AND CORRECTIONS.....</b>	<b>50</b>
2.3.1 <i>Inherent Statistical Counting Uncertainty</i> .....	50
2.3.2 <i>Deadtime Correction</i> .....	52
<b>3 TEPC CALIBRATION WITH IMPROVED METHODS.....</b>	<b>53</b>
<b>3.1 LINEAL ENERGY CALIBRATION .....</b>	<b>54</b>
3.1.1 <i>Manufacturer Setting</i> .....	54
3.1.2 <i>Proton and Electron Edge Calibration</i> .....	54
<b>3.2 DOSE DISTRIBUTION SPECTRUM .....</b>	<b>69</b>
3.2.1 <i>Generating the Dose Distribution Spectrum</i> .....	69
3.2.2 <i>The Complete Dose Distribution Spectrum</i> .....	70
<b>3.3 EXTRAPOLATING BELOW THE ELECTRONIC THRESHOLD .....</b>	<b>72</b>
3.3.1 <i>Electronic Threshold</i> .....	72
3.3.2 <i>Comparison Between Experimental Measurements &amp; FLUKA Simulations</i> .....	73
3.3.3 <i>RMC Method</i> .....	82
3.3.4 <i>Improved Methods (MD-1 &amp; MD-2)</i> .....	87

<b>3.4</b>	<b>NON-NEUTRON AND NEUTRON SEPARATION .....</b>	<b>106</b>
3.4.1	<i>Mixed Radiation Doses with Lineal Energy Around 10 keV/μm .....</i>	<i>106</i>
3.4.2	<i>Methods .....</i>	<i>106</i>
3.4.3	<i>Results &amp; Discussion .....</i>	<i>108</i>
<b>4</b>	<b>COSMIC RADIATION DOSE MEASUREMENT .....</b>	<b>109</b>
<b>4.1</b>	<b>CONVERSION COEFFICIENT EXPERIMENT .....</b>	<b>109</b>
4.1.1	<i>Design Idea .....</i>	<i>109</i>
4.1.2	<i>Dock-Boat Experiment .....</i>	<i>112</i>
4.1.3	<i>Dock-Park Experiment .....</i>	<i>114</i>
4.1.4	<i>Results .....</i>	<i>116</i>
4.1.5	<i>Conclusion and Discussion .....</i>	<i>119</i>
<b>4.2</b>	<b>INTERCALIBRATING EXPERIMENTAL MEASUREMENTS WITH ANALYTICAL DOSE RESULTS.....</b>	<b>120</b>
4.2.1	<i>Introduction .....</i>	<i>120</i>
4.2.2	<i>Method .....</i>	<i>121</i>
4.2.3	<i>Results From the Measurements Done at the Ottawa FPS Station.....</i>	<i>123</i>
4.2.4	<i>Analytical Results (RS250) &amp; Experimental Results by Using the RMC Method .....</i>	<i>126</i>
4.2.5	<i>Results by Using MD-1 and MD-2 Methods .....</i>	<i>132</i>
4.2.6	<i>Conclusion and Discussion .....</i>	<i>140</i>
<b>5</b>	<b>CONCLUSION AND DISCUSSION.....</b>	<b>143</b>
	<b>REFERENCES .....</b>	<b>148</b>
	<b>APPENDICES .....</b>	<b>154</b>

## LIST OF TABLES

Table 1. The summary table including the count rate, fitted fermi-like equation, the three marker points ( <i>iflex</i> , $i\delta\delta$ , <i>iTC</i> ) and the calibration factor generated from the <i>AmBe</i> high LET spectrum at 0.5 m. ....	62
Table 2. The summary table including the count rate, fitted fermi-like equation, the three marker points ( <i>iflex</i> , $i\delta\delta$ , <i>iTC</i> ) and the calibration factor generated from the <i>AmBe</i> high LET spectrum at 1.0 m. ....	63
Table 3. The summary table includes the count rate, fitted fermi-like equation, the three marker points ( <i>iflex</i> , $i\delta\delta$ , <i>iTC</i> ) and the calibration factor generated from the <i>AmBe</i> low LET spectrum at 0.5 m. ....	67
Table 4. The summary table includes the count rate, fitted fermi-like equation, the three marker points ( <i>iflex</i> , $i\delta\delta$ , <i>iTC</i> ) and the calibration factor generated from the <i>AmBe</i> low LET spectrum at 1.0 m. ....	68
Table 5. The summary of the dose equivalent rates (H) calculated from gamma rays' ( $^{137}\text{Cs}$ ) spectra by using the experimental measurements (TEPC_EXP.) and FLUKA simulation; the percentage differences between the underestimated dose (raw experimental measurements) and the simulated dose result.....	78
Table 6. The summary of the dose equivalent rates (H) calculated from gamma rays' ( $^{137}\text{Cs}$ ) spectra by using the experimental measurements (TEPC_EXP.) and the RMC method; the percentage differences between the underestimated dose (raw experimental measurements) and the result after extrapolation below the low LET threshold.....	83
Table 7. The summary of the dose equivalent rates (H) calculated from natural background radiation's spectra by using the experimental measurements (TEPC_EXP.) and the RMC method; the percentage differences between the underestimated dose (raw experimental measurements) and the results after extrapolations below the low LET threshold.....	84
Table 8. The summary of the dose equivalent rates (H) calculated from the FLUKA spectra using the simulated data and MD-1; the percentage differences between the raw FLUKA doses, and the results after extrapolations.....	91
Table 9. The summary of the dose equivalent rates (H) calculated from the FLUKA spectra using the simulated data and the MD-2 method; the percentage differences between the raw FLUKA doses and the results after extrapolations.....	92
Table 10. The summary of the dose equivalent rates (H) calculated from the FLUKA spectra using the simulated data and MD-1; the percentage differences between the raw FLUKA doses, and the results after extrapolations.....	95
Table 11. The summary of the dose equivalent rates (H) calculated from the FLUKA spectra using the simulated data and the MD-2 method; the percentage differences between the raw FLUKA doses, and the results after extrapolations.....	96
Table 12. The summary of the dose equivalent rates (H) calculated from the gamma rays' ( $^{137}\text{Cs}$ ) spectra by using the experimental measurements (TEPC_EXP.), MD-1 and MD-2 methods; the percentage differences between the underestimated dose (raw experimental measurements) and the results after extrapolations below the low LET threshold.....	100
Table 13. The summary of the dose equivalent rates (H) calculated from natural background radiation's spectra using the experimental measurements (TEPC_EXP.), MD-1 and MD-2 methods; the percentage differences between the underestimated dose (raw	

experimental measurements) and the results after extrapolations below the low LET threshold. ....	101
Table 14. The summary of the ambient dose equivalent rates $H^*(10)$ contributed from terrestrial radiation ( $H^*(10)_{TR}$ ) non-neutron cosmic radiation ( $H^*(10)_{Non-n. CR}$ ) and cosmic radiation including neutron ( $H^*(10)_{With n. CR}$ ) measured at different times and locations by using the counts collected from RS250 in 15 min. ....	116
Table 15. The dose equivalent rates $H$ contributed from non-neutron radiation measured at different time and locations by using HAWK 2 and four different analysis methods (RMC, MD-1, MD-2). ....	118
Table 16. The post-measurement calibration results of the low LET ambient dose equivalent coefficient $f$ for non-neutron cosmic radiation field by using $\Delta H^*(10)_{TRRS250}/\Delta H_{TRTEPC}$ (Equation 43). ....	119
Table 17. The eight experiments' measurement dates, geological and geographic features. ....	120
Table 18. The CC count rates, analytical $H^*10s$ and the ratio of $H^*10_{CRRS250}/H^*10_{TRRS250}$ contributed from non-neutron and with neutron cosmic radiation measured at 8 different locations by using RS250. ....	126
Table 19. The summary of experimental $H^*10$ contributed from non-neutron cosmic radiation measured at 8 different locations by using HAWK TEPC and the analysis method (RMC). ....	127
Table 20. The summary of experimental $H^*10$ contributed from cosmic radiation including neutron measured at 8 different locations using HAWK TEPC and the RMC method. ....	130
Table 21. The summary includes the experimental $H^*10$ contributed from non-neutron cosmic radiation detected at 8 different locations with HAWK and analyzed by using MD-1, the discrepancies with the analytical dose results from RS250, and the slope used for extrapolation below the electronic threshold. ....	133
Table 22. The summary includes the experimental $H^*10$ contributed from non-neutron cosmic radiation detected at 8 different locations with HAWK and analyzed by using MD-2, the discrepancies with the analytical dose results from RS250, and the slope used for extrapolation below electronic threshold. ....	134
Table 23. The summary of experimental $H^*10$ contributed from with-neutron cosmic radiation measured at 8 different locations by using HAWK TEPC and two different analysis methods (MD-1 & MD-2). ....	138
Table 24. The summary of the dose equivalent rates ( $H$ ) calculated from the FLUKA spectra by using the simulated data and RMC; the percentage differences between the raw FLUKA doses and the results after extrapolations. ....	156
Table 25. The ratios of ambient dose equivalents contributed from non-neutron cosmic radiation to terrestrial radiation ( $H^*10_{Non-n. CR}/H^*10_{TRRS250}$ ). ....	157
Table 26. The summary including the experimental $H^*10$ contributed from cosmic radiation including neutron measured at 8 different locations with HAWK and analyzed by using MD-1, the discrepancies with respect to the analytical dose results from RS250, and the slope used for extrapolation below electronic threshold. ....	158
Table 27. The summary including the experimental $H^*10$ contributed from cosmic radiation including neutron measured at 8 different locations with HAWK and analyzed by using MD-2, the discrepancies with respect to the analytical dose results from RS250, and the slope used for extrapolation below electronic threshold. ....	159

## LIST OF FIGURES

Figure 1. Major reactions involved in the collisions of cosmic radiation with air (McCall, 2000). .....	21
Figure 2. The structures of a TEPC, including the spectrum analyzer system (left) and TE sensitive volume (right). ....	30
Figure 3. The electrons are accelerated and attracted toward the anode under the electric field inside the TEPC detector. ....	31
Figure 4. A typical lineal energy spectrum produced from a TEPC after exposure to <i>AmBe</i> source for 30 minutes. ....	33
Figure 5. The stations of the Health Canada’s Fixed Point Surveillance (FPS) Network (Health Canada, 2015) .....	36
Figure 6. A typical 15 min energy spectrum produced from RS250 at the Ottawa FPS station (Radiation Protection Bureau). ....	38
Figure 7. The appearance of the HAWK TEPCs.....	44
Figure 8. Diagram showing constructional details of the HAWK electronics (spectrum analyzer system) (A) and Rossi-type detector (B) chambers. The figures are drawn based on a general description given for HAWK TEPC. ....	45
Figure 9. Qualitative illustration showing the conversion of energy spectrum to lineal energy spectrum after calibration.....	47
Figure 10. The experimental calibration set-up of HAWK 2 by exposure to a neutron source ( <i>AmBe</i> )......	58
Figure 11. The <i>AmBe</i> high LET spectrum measured from the HAWK 2 TEPC at site size $D = 2$ $\mu\text{m}$ . The proton edge region is highlighted by grey.....	59
Figure 12. Zoomed neutron spectrum of the proton-edge region of Figure 11, generated from the measurements when detector and source are 0.5 m apart. A fermi-like function was fitted to the measured data in the grey region (channel 20 to 154). ....	60
Figure 13. Zoomed view of the proton-edge region of the <i>AmBe</i> high LET spectrum (HAWK 2), generated from the measurements when detector and source are 1.0 m apart. A fermi-like function was fitted to the measured data in the grey region (channel 20 to 154). ....	61
Figure 14. The <i>AmBe</i> low LET spectrum measured from the HAWK 2 at site size $D = 2 \mu\text{m}$ . The proton edge region is highlighted by grey. ....	64
Figure 15. Zoomed view of the proton-edge region of the <i>AmBe</i> low LET spectrum (HAWK 2), generated from the measurements when detector and source are 0.5 m apart. A fermi- like function was fitted to the measured data in the grey region (channel 50 to 93).....	65
Figure 16. Zoomed view of the proton-edge region of the <i>AmBe</i> low LET spectrum (HAWK 2), generated from the measurements when detector and source are 1.0 m apart. A fermi-like function was fitted to the measured data in the grey region (channel 50 to 93).....	66
Figure 17. Dose distribution spectrum $y \cdot d(y)$ measured at two different distances after the lineal calibration with the p-edge and e-edge techniques. ....	71
Figure 18. A typical dose distribution low LET spectrum produced from HAWK TEPC using the experimental measurements for background radiation done at the Ottawa FPS station (RPB) on 22-June-2021.....	72
Figure 19. The set up of HAWK exposed to $^{137}\text{Cs}$ . ....	75
Figure 20. Set-up of the field experiment performed in Ottawa local park near Rideau Canal Lock 35-Narrows on 03-Aug-2021. ....	76

Figure 21. Comparison between the gamma dose distribution spectra (0-5 $keV/\mu m$ ) using the measurements with radioactive $^{137}Cs$ gamma source and the FLUKA simulation of 662 keV photon.....	78
Figure 22. Comparisons between the dose distribution spectra by using the field measurements and the FLUKA simulation with different monoenergetic beams. ....	80
Figure 23. Comparison of experimental and simulated logarithmic spectra of counts. The grey area shows the linear relation between $\ln(n(y))$ and $\ln(y)$ from 0.55 $keV/\mu m$ to 1.05 $keV/\mu m$ .....	81
Figure 24. Comparisons between the gamma dose distribution spectra using the experimental measurements with $^{137}Cs$ , the results after applying the RMC extrapolation method, and the FLUKA simulation with 662 keV photon after normalization.....	83
Figure 25. Comparisons between the dose distribution spectra using the field measurements with natural background radiation, the results after applying the RMC extrapolation method, and the FLUKA simulation with 662 keV photon after normalization.....	85
Figure 26. Comparison of normalized dose distribution spectra between simulations and after MD-1 & MD-2 extrapolations.....	90
Figure 27. Comparison of normalized dose distribution spectra between mixed field simulation (Counts ratio of 4 GeV $\mu$ : 662 keV $\gamma = 4:1$ ) and after MD-1 & MD-2 extrapolations. ....	93
Figure 28. The comparison between the slopes of the linear best fit equations from $\ln(ny)$ vs. $\ln(y)$ spectra of simulated mixed fields by using MD-1 and MD-2 extrapolation methods. Error bars represent the uncertainties on the slopes of $\ln(n(y))$ versus $\ln(y)$ plots (y-axis).....	94
Figure 29. Comparison of Cs-137 experimental and simulated dose distribution spectra for multiple monoenergetic particles incident on the simulated TEPC from 1 meter.....	98
Figure 30. The gamma dose distribution spectra by using the experimental measurements (Cs-137), the results after applying the MD-1 & MD-2 extrapolation methods, and the FLUKA simulation with 662 keV photon. ....	99
Figure 31. Comparison of experimental (natural background) and simulated dose distribution spectra for multiple monoenergetic particles incident on the simulated TEPC from 1 meter. ....	102
Figure 32. The dose distribution spectra of the experimental measurements with natural background radiation, the results after applying the MD-1 extrapolation method, and the FLUKA simulation with 662 keV photon and 4 GeV muon. ....	103
Figure 33. The dose distribution spectra of the experimental measurements with natural background radiation, the results after applying the MD-2 extrapolation method, and the FLUKA simulation with 662 keV photon and 4 GeV muon. ....	105
Figure 34. $^{137}Cs$ dose distribution spectrum measured by using the HAWK 2 tissue equivalent proportional counter with fermi-like equation fitted to the electron edge. ....	107
Figure 35. The dose distribution spectrum $y \cdot d(y)$ by using the measurements done in the $AmBe$ calibration experiment. ....	107
Figure 36. The separation of the non-neutron and neutron dose distribution spectra.....	108
Figure 37. The side by side measurements performed on the dock on 11-Sep-2020 inside the Britannia Yacht Club, Ottawa. A. the distance between the dock and shore is approximately 30 m. B. a photo of the three instruments.....	112

Figure 38. The set-up picture of the boat experiment performed on the centre of the Ottawa river on 16-Sep-2020. ....	113
Figure 39. The set-up picture of the field measurements performed on the dock near the Rideau Canal Lock 35-Narrows on 03-Aug-2021. ....	115
Figure 40. The set-up picture of the field measurements performed in the park near the Rideau Canal Lock 35-Narrows on 03-Aug-2021. ....	115
Figure 41. Set-up picture of the experiments performed on the hill of the Gatineau Park on 29-Jun-2021. ....	121
Figure 42. A typical dose distribution spectrum produced from HAWK TEPC by using the experimental measurements for background radiation done at the Ottawa FPS station (RPB) on 22-June-2021. ....	124
Figure 43. The comparison between experimental and analytical cosmic non-neutron $H * (10)s$ with respect to the changes along with the count rate of the CC channel in RS250. Error bars represent the uncertainties on the RS250 CC count rates detected at the 8 locations (x-axis) and $H * (10)$ (y-axis) from tables 18 and 19. ....	128
Figure 44. The comparison between experimental and analytical cosmic non-neutron $H * (10)s$ with respect to the changes along with the ratio of $H * 10Non - n. CR$ over $H * 10TR$ . Error bars represent the uncertainties on the dose ratios (CR/TR from RS250) at the 8 locations (x-axis) and $H * (10)$ (y-axis) from tables 18 and 19. ....	129
Figure 45. The comparison between experimental and analytical cosmic $H * (10)s$ (with neutron) along with the count rate of the CC channel in RS250. Error bars represent the uncertainties on the RS250 CC count rates detected at the 8 locations (x-axis) and $H * (10)$ (y-axis) from tables 18 and 20. ....	130
Figure 46. The comparison between experimental and analytical cosmic $H * (10)s$ with neutrons with respect to the changes along the ratio of $H * 10With - n. CR$ over $H * 10TR$ . Error bars represent the uncertainties on the dose ratios (CR/TR from RS250) at the 8 locations (x-axis) and $H * (10)$ (y-axis) from tables 18 and 20. ....	131
Figure 47. The comparison between experimental and analytical non-neutron cosmic $H * (10)s$ along with the count rate. Error bars represent the uncertainties on the RS250 CC count rates detected at the 8 locations (x-axis) and $H * (10)$ (y-axis) from tables 18, 21 and 22. ....	132
Figure 48. The comparison between experimental and analytical non-neutron cosmic $H * (10)s$ along with the ratio of $H * 10Non - n. CR$ over $H * 10TR$ . Error bars represent the uncertainties on the dose ratios (CR/TR from RS250) at the 8 locations (x-axis) and $H * (10)$ (y-axis) from tables 18, 21 and 22. ....	135
Figure 49. The slopes of the linear best fit equations from $ln(ny)$ vs. $ln(y)$ spectra by using experimental measurements from HAWK (MD-1 & MD-2) and FLUKA simulation along with the different ratios of $H * 10Non - n. CR$ over $H * 10TR$ . Error bars represent the uncertainties on the dose ratios (CR/TR from RS250) (x-axis) and slopes ( $ln(n(y))$ versus $ln(y)$ plots) (y-axis) from tables 18, 21 and 22. ....	136
Figure 50. The comparison between experimental and analytical cosmic $H * (10)s$ (with neutron) along with the count rate. Error bars represent the uncertainties on the RS250 CC count rates detected at the 8 locations (x-axis) and $H * (10)$ (y-axis) from tables 18 and 23. ....	138
Figure 51. The comparison between experimental and analytical $H * (10)s$ along with the ratio of $H * 10With n. CR$ over $H * 10TR$ . Error bars represent the uncertainties on the	

dose ratios (CR/TR from RS250) at the 8 locations (x-axis) and  $H * (10)$  (y-axis) from tables 18 and 23. .... 139

Figure 52. Experiment set-up using the BC408 scintillator, HAWK 3 the 4-channel all digital spectrometer Pixie-4. .... 147

Figure 53. The *AmBe* high LET spectrum measured from the HAWK 2 at site size  $D = 2 \mu\text{m}$ . .... 154

Figure 54. The *AmBe* low LET spectrum measured from the HAWK 2 at site size  $D = 2 \mu\text{m}$ . 155

## EQUATIONS

---

		Page
Equation 1	$LET_{\infty} = \left(\frac{dE}{dt}\right)_{\infty}$	25
Equation 2	$D = \frac{d\bar{\varepsilon}}{dm}$	27
Equation 3	$H = Q \cdot D$	27
Equation 4	$\dot{H} = \frac{dH}{dt}$	27
Equation 5	$Q(L) = \begin{cases} 1 & L < 10 \text{ keV}/\mu\text{m} \\ 0.32L - 2.2 & 10 \leq L \leq 100 \text{ keV}/\mu\text{m} \\ \frac{300}{\sqrt{L}} & L > 100 \text{ keV}/\mu\text{m} \end{cases}$	28
Equation 6	$H^*(10) = f \cdot H$	28
Equation 7	$\dot{H}^*(10) = \frac{dH^*(10)}{dt}$	28
Equation 8	$y = \frac{\varepsilon}{\bar{l}}$	29
Equation 9	$\bar{l} = 4 \cdot \frac{V}{A} = \frac{2}{3} d_s$	29
Equation 10	$H^*(10)_{Low\ LET} = H^*(10)_{Non-n.\ CR} + H^*(10)_{TR}$	34
Equation 11	$H^*(10)_{Low\ LET} + H^*(10)_{High\ LET} = H^*(10)_{With\ n.\ CR} + H^*(10)_{TR}$	35
Equation 12	$H^*(10)_{Non-n.\ CR}^{RS250} = 0.0148 \cdot n_{CC}^{RS250} + 5.3323$	41
Equation 13	$H^*(10)_{With\ n.\ CR}^{RS250} = 0.0297 \cdot n_{CC}^{RS250} - 14.7989$	41
Equation 14	$H^*(10)_{Non-n.\ CR}^{TEPC} = f_1 \cdot H_{Low\ LET}^{TEPC} - H^*(10)_{TR}^{RS250}$	42
Equation 15	$H^*(10)_{With\ n.\ CR}^{TEPC} = f_1 \cdot H_{Low\ LET}^{TEPC} + f_2 \cdot H_{High\ LET}^{TEPC} - H^*(10)_{TR}^{RS250}$	43
Equation 16	$\bar{y}_f = \frac{\sum_i y_i n(y_i)}{\sum_i n(y_i)}$	49

Equation 17	$\bar{y}_D = \frac{\sum_i y_i^2 n(y_i)}{\sum_i y_i n(y_i)}$	49
Equation 18	$d(y) = \frac{y \cdot f(y)}{\bar{y}_f}$	49
Equation 19	$y \cdot d(y) = \frac{y^2 \cdot f(y)}{\bar{y}_f}$	49
Equation 20	$D = \frac{d\varepsilon}{dm} = \frac{1.602 \times 10^{-13} \cdot \sum_i y_i n(y_i)}{m_{gas}}$	50
Equation 21	$D = \frac{0.204}{d^2} \sum_i y_i n(y_i)$	50
Equation 22	$H = \frac{0.204}{d^2} \sum_i q(y_i) y_i n(y_i)$	50
Equation 23	$H^*(10)_{Non-n. CR}^{TEPC} = \frac{1}{1.05} \cdot H_{Low LET}^{TEPC} - H^*(10)_{TR}^{RS250}$	51
Equation 24	$H^*(10)_{With n. CR}^{TEPC} = \frac{1}{1.05} \cdot H_{Low LET}^{TEPC} + \frac{1}{1.25} H_{High LET}^{TEPC} - H^*(10)_{TR}^{RS250}$	51
Equation 25	$\sigma_n = \sqrt{n}$	51
Equation 26	$Count\ rate = \frac{N}{t} \pm \frac{\sigma_N}{t} = \frac{N}{t} \pm \frac{\sqrt{N}}{t}$	51
Equation 27	$\sigma_D = \frac{0.204}{d^2} \sqrt{\sum_i y_i^2 \sigma_{n(y_i)}^2}$	52
Equation 28	$\sigma_H = \frac{0.204}{d^2} \sqrt{\sum_i q(y_i)^2 y_i^2 \sigma_{n(y_i)}^2}$	52
Equation 29	$\sigma_{H^*(10)} = f \cdot \sigma_H$	52
Equation 30	$\begin{cases} \sigma_{H^*(10)_{Non-n. CR}^{RS-250}} = 0.0148 \cdot \sigma_n = 0.0148 \cdot \sqrt{n} & \text{Non - n. CR} \\ \sigma_{H^*(10)_{With-n. CR}^{RS-250}} = 0.0297 \cdot \sigma_n = 0.0297 \cdot \sqrt{n} & \text{With n. CR} \end{cases}$	52
Equation 31	$DT\ factor = \frac{1}{1 - (6.42 \cdot 10^{-5} \cdot n)}$	53
Equation 32	$i \cdot d(i) = \frac{A}{1 + \exp(B \cdot (i - C))}$	57
Equation 33	$i_{flex} = C$	57
Equation 34	$i_{\delta\delta} = \frac{\ln(2 + \sqrt{3})}{B} + C$	57

- Equation 35  $i_{TC} = \frac{2}{B} + C$  57
- Equation 36  $n(y_{i=1 \text{ to } 4}) = \frac{y_5 n(y_5)}{y_{(i=1 \text{ to } 4)}}$  83
- Equation 37  $n(y_1) = \frac{y_3 n(y_3) - y_2 n(y_2)}{y_1}$  90
- Equation 38  $n(y_2) = \frac{y_3 n(y_3) + y_4 n(y_4)}{y_2}$  90
- Equation 39  $\Delta H^*(10)_{TR}^{RS250} = H^*(10)_{1,TR}^{RS250} - H^*(10)_{2,TR}^{RS250}$  111
- Equation 40  $H_{TR}^{TEPC} = H_{Low LET}^{TEPC} - H_{CR}$  111
- Equation 41  $\Delta H_{TR}^{TEPC} = (H_{Low LET}^{TEPC} - H_{CR})_1 - (H_{Low LET}^{TEPC} - H_{CR})_2$  111
- Equation 42  $\Delta H_{TR}^{TEPC} = H_{1,Low LET}^{TEPC} - H_{2,Low LET}^{TEPC}$  112
- Equation 43  $f = \frac{\Delta H^*(10)_{TR}^{RS250}}{\Delta H_{TR}^{TEPC}} = \frac{H^*(10)_{1,TR}^{RS250} - H^*(10)_{2,TR}^{RS250}}{H_{1,low LET}^{TEPC} - H_{2,low LET}^{TEPC}}$  112
- Equation 44  $H^*(10)_{Non-n. CR}^{TEPC} = 0.95 \cdot H_{Low LET}^{TEPC} - H^*(10)_{TR}^{RS250}$  123
- Equation 45  $H^*(10)_{With n. CR}^{TEPC} = 0.95 \cdot H_{Low LET}^{TEPC} + 0.80 \cdot H_{High LET}^{TEPC} - H^*(10)_{TR}^{RS250}$  123

## **LIST OF APPENDICES**

---

Appendix A. HAWK 3 Lineal Energy Calibration Results .....	154
Appendix B. Additional Experimental Results.....	156
Appendix C. Data analysis worksheet (RMC).....	160

## NOMENCLATURE

---

D	Absorbed dose
$e^-$	Electron
$e^+$	Positron
H	Dose equivalent
$H^*(10)$	Ambient dose equivalent, dose equivalent produced at 10 mm depth of the ICRU sphere
$H_{\text{Low LET}}^{\text{TEPC}}$	Dose equivalent (rate) calculated from low LET spectrum, which is measured by HAWK TEPC
$H_{\text{High LET}}^{\text{TEPC}}$	Dose equivalent (rate) calculated from high LET spectrum, which is measured by HAWK TEPC
$H^*(10)_{\text{TR}}^{\text{RS250}}$	Ambient dose equivalent (rate) contributed from the terrestrial radiation, which is measured by RS250
$H^*(10)_{\text{CR}}^{\text{RS250}}$	Ambient dose equivalent (rate) contributed from the cosmic radiation, which is measured by RS250
$\varepsilon$	Energy deposited in Rossi-type detector volume
$\bar{l}$	Mean chord length of microscopic tissue site
n	Neutron
non-n	Non-neutron
with n	Including neutron
p	Proton
Q	Quality factor
$\mu$	Muon
$\nu_\mu$	Neutrino
$\bar{\nu}_\mu$	Anti-neutrino
y	Lineal energy
$\bar{y}_D$	Dose mean lineal energy
$\bar{y}_f$	Frequency mean lineal energy
$y \cdot d(y_i)$	Fraction of total absorbed dose delivered by events in the ith lineal energy channel
$\gamma$	Gamma ray
$\pi$	Pion

## ACRONYMS

---

AmBe	Americium-Beryllium
CC	Overflow Channel, Cosmic Channel
Cf	Californium
CNSC	Canadian Nuclear Safety Commission
CFR	Canada Federal Regulators
CPS	Counts Per Second
FPS	Fixed Point Surveillance
FWT	Far West Technology Inc
IAEA	International Atomic Energy Agency
ICRP	International Commission on Radiological Protection
ICRU	International Commission on Radiation Units and Measurements
LET	Linear Energy Transfer
MCA	Multi-channel Analyzer
NORM	Naturally Occurring Radiative Material
RBE	Relative Biological Effectiveness
RMC	The Royal Military College of Canada
RPB	Radiation Protection Bureau
PNNL	Pacific Northwest National Laboratory
TE	Tissue Equivalent
TEPC	Tissue Equivalent Proportional Counter

# 1 INTRODUCTION

---

## 1.1 NATURAL BACKGROUND RADIATION AND COSMIC RAY

Natural background radiation is ubiquitous on Earth. In the long study to evaluate and reduce the radiation-induced effects on human health and non-human biota, natural background radiation monitoring plays a significant role in setting the upper limit of the radiation dose an individual can be exposed to. The maximum radiation dose received per calendar year is regulated to protect the public and nuclear energy workers from the potentially harmful radiation effects (UNSCEAR, 2008). In Canada, the Radiation Protection Regulations states that the public should not receive more than 1 mSv per year other than the occupational and natural background radiation (ICRP-103, 2007). This dose limit is set by following the recommendations of the International Commission on Radiological Protection (ICRP), the International Atomic Energy Agency (IAEA) and Canada Federal Regulators (CFR) based on research and databases on occupational radiation and natural background radiation monitoring. According to the statistics, the average Canadians receive approximately 3.7 mSv effective dose from all different radiation sources in one calendar year. The natural background radiation accounts for approximately 49% (Grasty & LaMarre, 2004).

Natural background radiation at ground level consists of cosmic radiation, terrestrial radiation, and radiation from radon gases. Terrestrial radiation refers to the gamma rays<sup>1</sup> that originated from soil and rock, which is resulted from the radioactive decay of natural materials in the earth (i.e.,  $^{238}\text{U}$ ,  $^{232}\text{Th}$  and  $^{40}\text{K}$  et al.) or from man-made contaminations (i.e.,  $^{60}\text{Co}$  or  $^{137}\text{Cs}$ ). In

---

<sup>1</sup> The usual energy range of natural gamma rays is 0.1-3 MeV (Guinn, 2003).

2004, the effective dose contributed from terrestrial radiation in Ottawa was  $0.2 \text{ mSv/yr.}$ , accounting for approximately 11% of the radiation dose from natural background radiation (Grasty & LaMarre, 2004). In addition to terrestrial radiation, cosmic radiation is also a vital part of natural background radiation. According to the report published in 2004, the effective dose from cosmic rays at ground level in Ottawa is  $0.35 \text{ mSv/yr.}$ , which accounts for approximately 22% of the radiation dose from natural background radiation (Grasty & LaMarre, 2004). Cosmic radiation dose increases with latitude because the effect of the earth's magnetic field deflects fewer cosmic ray particles at elevated locations (Shahbazi-Gahrouer, 2013).

The primary cosmic rays originally generate from supernova explosions, flares, coronal mass ejections (CME), and other violent events travel through space at nearly the speed of light (Zyla, 2020). These high-energy charged particles are mostly deflected by the earth's magnetic field and interact with the atmospheric atoms. Less than 1% of primary cosmic rays are detected at sea level (Ziegler, 1996). When the primary cosmic rays collide with the atoms in the Earth's atmosphere, the secondary cosmic rays are produced. The resulting particles either decay or continuously strike more and more atoms, which causes the cosmic ray cascade. Secondary cosmic ray particles generated in the cosmic ray cascade include neutrons, protons and pions, muons, neutrinos, gamma rays, electrons, and positrons et al. The most common reactions occurred in the cosmic ray cascade are listed in Figure 1.

	Reactions	
Electromagnetic:	$\pi^0 \rightarrow \gamma + \gamma \rightarrow e^+ + e^-$	(A)
Mesonic:	$\pi^+ \rightarrow \mu^+ + \nu_\mu$	(B)
	$\pi^- \rightarrow \mu^- + \bar{\nu}_\mu$	(C)
Nucleonic:	$p + air \rightarrow p + n + \pi^0 + \pi^\pm$	(D)
	$n + air \rightarrow p + n + \pi^0 + \pi^\pm$	(E)

Figure 1. Major reactions involved in the collisions of cosmic radiation with air<sup>2</sup> (McCall, 2000).

Gamma rays (photons,  $\gamma$ ) are mainly decayed from the short-lived neutral pions ( $\pi^0$  meson) and then electron-positron pairs are created (Figure 1. A). Gamma rays have no mass or charge; they lose energy through ionization and travel very far in the air. At ground level, the energy distribution of natural gamma rays ranges from a few keV to approximately 3 MeV (Guinn, 2003).

Muons ( $\mu^\pm$ ) are decayed from the short-lived charged pions ( $\pi^\pm$ ) (Figure 1. B & C) or kaons from high altitudes (Mok & Cheng, 2001). Muons have a mass of  $105.66 \text{ MeV}/c^2$ , which allows muons of a given energy to travel long distances in the atmosphere (Friedberg, 2011). At ground level, muons' energy distribution ranges from a few MeV to hundreds of GeV, and the mean kinetic energy is approximately 4 GeV (Atri & Melott, 2013) (Grieder, 2001). Muons are

---

<sup>2</sup>  $p$ : protons,  $n$ : neutrons,  $\pi$ : pions,  $\mu$ : muons,  $\nu_\mu$ : neutrino,  $\bar{\nu}_\mu$ : anti-neutrino,  $\gamma$ : gamma rays,  $e^-$ : electrons,  $e^+$ : positrons.

dominant in the charged secondary cosmic radiation, and their intensity vary at different altitudes (Delgado, 2001).

The most of cosmic neutrons ( $n$ ) detected on the earth result from nucleonic reactions (Figure 1. D & E). At sea level, approximately 10 % of  $H^*(10)$  are contributed from cosmic neutron (UN, 1966) (Nakamura, 2008). The cosmic neutron dose increases with altitude, for example, the neutron dose detected at 12.5 km over sea level is approximately 300 times more than that at sea level (Shahbazi-Gahrouer, 2013). Neutrons can travel hundreds or up to thousands of meters in the air. When the uncharged neutron particles penetrate biological tissues, they do not ionize electrons or atoms directly; instead, they are absorbed into atoms (i.e., nuclei), which emit proton radiation (McCall, 2000).

This project measures the radiation doses from cosmic radiation at the ground level. In other words, the cosmic particles “successfully” reach the ground, including electrons, gamma rays, muon, neutron et al., mainly coming from the secondary cosmic rays with few coming from the primary cosmic rays with energies higher than 1 *GeV* (McCall, 2000).

## 1.2 PHYSICAL ASPECTS

### 1.2.1 Protection and Operational Quantity

The International Commission on Radiological Protection (ICRP) developed the protection quantity, effective dose. Effective dose plays a significant role in determining the protection dose limits. As mentioned in Section 1.1, the average radiation dose an individual received per calendar year is quantified as an effective dose. It is a risk-adjusted dosimetric value to quantify the stochastic effect of the human body by summing the equivalent dose from different organs and tissues after exposure to internal or external ionizing radiation (ICRP, 2016). Effective dose employs tissue weighting factors for human organs and tissues according to their sensitivities when exposed to different types of radiation. The SI unit of effective dose is sievert ( $Sv$ ).

The effective dose is not directly measurable. In practice, the other quantity called the operational quantity, typically the ambient dose equivalent ( $H^*(10)$ ), can be measured by detectors.  $H^*(10)$  can be used as an approximation of the effective dose depending on the energies of incident photons (Chabot, 2015). For example, the ratio of the effective dose to  $H^*(10)$  is between 0.8 and 0.9 for photons with energy ranging from approximately 0.06 MeV to 10 MeV (Chabot, 2015).  $H^*(10)$  is invented for radiation dose measurements in individual and area monitoring. It is a conservative estimation of the energy deposited by ionizing radiation in tissues.  $H^*(10)$  is defined as the dose equivalent ( $H$ ) produced at 10 mm depth in the ICRU

defined phantom<sup>3</sup>, which has a similar atomic composition as human tissues, after exposure to external radiation (ICRP, 1991). The SI unit of  $H^*(10)$  is also sievert (Sv).

### 1.2.2 Linear Energy Transfer (LET) and Lineal Energy (y)

When evaluating the radiation-induced damages in tissues, the relative biological effectiveness (RBE) is employed to reveal the differences in the biological effects of exposure to two types of radiation. RBE is defined as the ratio of the (absorbed) dose of reference radiation to the (absorbed) dose of the radiation being examined which generates the same biological effect (Hendry, 2014). RBE is associated with dose, dose rate, the type of radiation and tissue traversed et al., as a function of linear energy transfer (LET).

Linear energy transfer, LET, is a macroscopic quantity that is defined as the average energy loss from the incoming radiation per unit length of its track when it traverses the tissue. The LET with a particular cut-off value ( $\Delta$ ) is denoted by  $LET_{\Delta}$ , which excludes all secondary ionizations that produce electrons with kinetic energy larger than  $\Delta$ . As  $\Delta$  approaches infinity,  $LET_{\Delta \rightarrow \infty}$ , the linear energy transfer becomes the unrestricted linear energy transfer (denoted by L), which is equivalent to the linear stopping power (Colautti & Magrin, 2020). LET can be calculated from:

$$LET_{\infty} = \left( \frac{dE}{dl} \right)_{\infty} \quad \text{Equation 1}$$

---

<sup>3</sup> The phantom is a 30 cm diameter ICRU tissue equivalent plastic sphere with a density of 1 g/cm<sup>3</sup> and the mass composition is 76.2 % oxygen, 11.1 % carbon, 10.1 % hydrogen and 2.6 % nitrogen (ICRP, 1991).

Where  $dE$  is the average energy loss from the incoming radiation and  $dl$  is the unit length of its track. The unit of LET is  $Jm^{-1}$  or  $keV/\mu m$ .

LET depends on both the nature of the ionizing particles<sup>4</sup> and the material traversed. When an individual is exposed to external radiation, the incoming particles penetrate human tissue, directly or indirectly interact with the cellular atoms or molecules, pose potential health impacts by damaging cells, tissues, or genetic materials. The higher the LET, the more severe the biological damages, i.e., higher RBE. Because radiation with higher LET deposits a larger amount of energy, and produces numerous ionizations in a smaller distance; these radiation-induced damages in tissues are more difficult to repair (Zyla, 2020). However, when  $LET > 100 keV/\mu m$ , RBE decreases as LET increases because the energy deposited by the ionizing particles is high enough to kill the cell; no more damage can be caused by any additional ionization events, i.e., overkill effect (Hendry, 2014).

Radiation is grouped into high LET and low LET. High LET radiation refers to the LET value greater than  $10 keV/\mu m$ , including alpha particles, neutrons, and protons with energy  $\leq 4 MeV$  (Curtis, 1992). Cosmic neutron is a source of high LET radiation because neutron with its substantial mass can interact with a medium and produce recoil protons, which deposits a large amount of energy in a short distance. For example, the LET value (track average<sup>5</sup>) for 14 MeV

---

<sup>4</sup> When the incoming radiation (for example, cosmic radiation) travels through material, it can deposit large enough energy to knock off electrons from atoms, the process is called ionization.

<sup>5</sup> LET can be calculated by using two methods: 1. the track average: the average energy deposited over a set distance, 2. the energy average: the average distance over when a set amount of energy is deposited.

neutrons is  $12 \text{ keV}/\mu\text{m}$ . While low LET radiation refers to the LET value less than  $10 \text{ keV}/\mu\text{m}$ , including electrons, positrons, photons, muons, gamma rays, x-rays, and protons with energy  $> 4 \text{ MeV}$  (Curtis, 1992). Cosmic and terrestrial gamma rays are considered as low LET radiation because they generate electrons (fast speed and low mass) in the collisions, and deposit energy less often along their path. For example, the LET value for  $1.2 \text{ MeV}$  gamma rays is  $0.3 \text{ keV}/\mu\text{m}$  and is associated with low RBE.

The physical quantity, absorbed dose ( $D$ ), is the quotient of the mean energy deposited ( $d\bar{\epsilon}$ ) divided by the unit mass of the matter ( $dm$ ) that the incoming radiation penetrates (Al-Bayati, 2012):

$$D = \frac{d\bar{\epsilon}}{dm} \quad \text{Equation 2}$$

The SI unit for  $D$  is gray ( $Gy$ ) and is equivalent to joule per kilogram ( $J/kg$ ).  $D$  can be used to calculate the dose equivalent ( $H$ ).  $H$  is a conservative estimation or a threshold dose-related to radiation exposure. Dose equivalent takes the RBE into consideration by employing a quality factor  $Q$  (ICRP, 1991):

$$H = Q \cdot D \quad \text{Equation 3}$$

Where  $D$  is the absorbed dose ( $Gy$ ) at the point of interaction and  $Q$  is the quality factor. The SI unit for dose equivalent is Sievert ( $Sv$ ). The dose equivalent rate ( $\dot{H}$ ) is the changes in dose equivalent in time ( $t$ ):

$$\dot{H} = \frac{dH}{dt} \quad \text{Equation 4}$$

The SI unit for dose equivalent rate is Sievert ( $Sv/h$ ). In the thesis, the dose equivalent rate is often simplified as dose equivalent (rate).

With the same amount of absorbed energy, the biology effects caused by different ionizing radiation will be very different. Quality factor ( $Q$ ) is utilized to characterise the biological effectiveness of a radiation and can be expressed as a function of LET, i.e.,  $Q(L)$ . The quality factor is recommended in ICRP 60 as (ICRP, 1991):

$$Q(L) = \begin{cases} 1 & L < 10 \text{ keV}/\mu\text{m} \\ 0.32L - 2.2 & 10 \leq L \leq 100 \text{ keV}/\mu\text{m} \\ \frac{300}{\sqrt{L}} & L > 100 \text{ keV}/\mu\text{m} \end{cases} \quad \text{Equation 5}$$

Then, the ambient dose equivalent,  $H^*(10)$  can be simply converted from  $H$  by using a conversion coefficient ( $f$ ), where  $f$  is called the ambient dose equivalent conversion coefficient:

$$H^*(10) = f \cdot H \quad \text{Equation 6}$$

The ambient dose equivalent rate ( $\dot{H}^*(10)$ ) is the changes in dose equivalent in time ( $t$ ):

$$\dot{H}^*(10) = \frac{dH^*(10)}{dt} \quad \text{Equation 7}$$

The SI unit for dose equivalent rate is Sievert ( $Sv/h$ ). In the project, the ambient dose equivalent rate is often simplified as ambient dose equivalent (rate) or  $H^*(10)$ .

LET plays an essential role in determining the radiation-induced effects. However, there is no feasible method to measure LET directly. As a substitute, lineal energy ( $y$ ) can be measured by detectors, a microscopic quantity and stochastic equivalent to LET (Wissmann, 2006).

Lineal energy,  $y$ , is the measurement of a single energy event deposited in a volume divided by the mean chord length of the volume (Al-Bayati, 2012):

$$y = \frac{\varepsilon}{\bar{l}} \quad \text{Equation 8}$$

Where  $\varepsilon$  is the deposited energy by the incident particle and  $\bar{l}$  is the mean chord length. The SI unit of lineal energy is  $keV/\mu m$ . The mean chord length is the mean length through a randomly oriented and isotropic volume. For example, for a spherical detector,

$$\bar{l} = 4 \cdot \frac{V}{A} = \frac{2}{3} d_s \quad \text{Equation 9}$$

Where  $V$  is the volume,  $A$  is the surface area,  $d_s$  is the diameter of the tissue equivalent (in both the composition and density) sphere simulated by the detector (in  $\mu m$ ).

One of the detectors that can measure the lineal energy distributions and distinguish the low LET and high LET spectra in mixed radiation fields is tissue equivalent proportional counter (TEPC), which will be discussed in the next section.

### 1.3 TISSUE EQUIVALENT PROPORTIONAL COUNTER (TEPC)

TEPC is recognized as the reference instrument in experimental microdosimetry (ICRP-103, 2007). According to the research done in flight altitude cosmic radiation dose measurements (Lindborg, 1999) (Taylor, 2002), the dose equivalent rates measured by TEPC agree with ( $\pm 20\%$ ) the results obtained gamma monitors (i.e., Ion Chamber Gamma Radiation Monitor, et al.) and the simulated dose results (i.e., CARI-6).

TEPC measures energy deposition in its sensitive volume, which can be converted to a distribution of lineal energy ( $y$ ) by utilizing a proper calibration factor (details will be discussed in Chapter 3). The sensitive volume is usually a sphere or cylinder of few centimetres in diameter, whose wall is made of tissue equivalent (TE) plastic and filled with gas with very low pressure (a few percent of the normal atmospheric pressure) to simulate the radiation absorption and energy deposition in human tissues at micrometre level (a few  $\mu\text{m}$ ). TEPC can simulate the microscopic volumes. According to Fano's theorem (Fano 1954), if the detector volume is constructed with a wall material and filled with gas that have equivalent atomic composition to human tissues, the dose measured by the detector will be the same, regardless of the size of its volume (Nam, 2013). In the detector volume, there is a central wire (anode electrode) surrounded by the conductive TE wall that serves as a cathode (Figure 2). The voltage applied between the anode and cathode is in the proportional voltage region (i.e., between the ionization and Geiger-Muller region), the high enough voltage enables the gas multiplication to take place in the TE sensitive volume due to secondary ionization. In the proportional voltage region, the energy deposited in TEPC is proportional to the output signal (Collums, 2012). The applied voltage in TEPC is usually between -600 V to -750 V. The other compartment of TEPC is the spectrum analyzer system (i.e., spectrometer, Figure 2), which contains all electronic parts to analyze the signal.

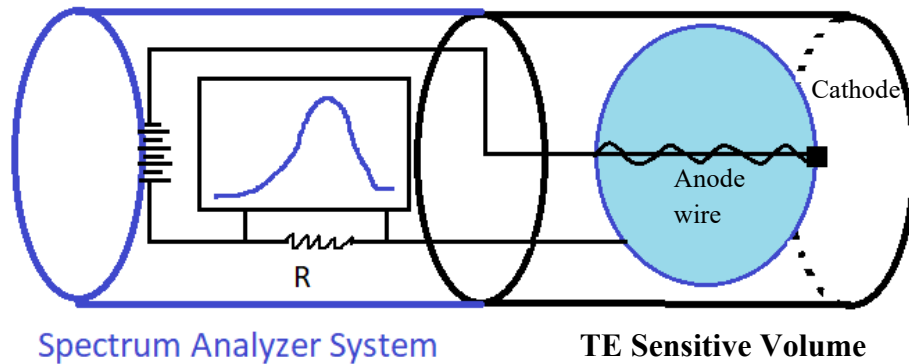


Figure 2. The structures of a TEPC, including the spectrum analyzer system (left) and TE sensitive volume (right).

When TEPC is exposed to radiation, the incoming ionizing particles collide with the TE wall or the gas molecules as they transverse the detector volume (Causey, 2018) (Figure 2). For example, electrons will penetrate the TE wall directly and ionize with gas molecules; gamma rays will knock off electrons from the TE wall; neutrons will interact with the TE wall and produce protons. These charged particles produced in the primary ionization, and the incoming radiation will continuously collide with the gas molecules (ionization), produce electrons, and positively charged gas ions in the detector volume. Negatively charged electrons and positively charged ions are created as electron-ion pairs. The electric force accelerates ion pairs due to the potential difference between the anode (a central wire) and cathode (shell). Then the negatively charged electrons are accelerated and attracted to the anode (Figure 3). The electric field intensity increases as function  $1/r$  as the electrons are approaching the anode ( $r$  is the distance of the electron from the center of the anode wire). The electrons gain more and more energy per unit of distance as they accelerate towards the anode and create more secondary ionizations, thus trigger an avalanche of ionization. The total charges arrived at the anode is proportional to the

total amount of ionization produced by the initial ionizing particles entering the TE volume. The total charged are proportionate to the total energy deposited by the particles, ( $\varepsilon$  in equation 8).

The charges collected by the anode will result in a voltage drop in the circuit.

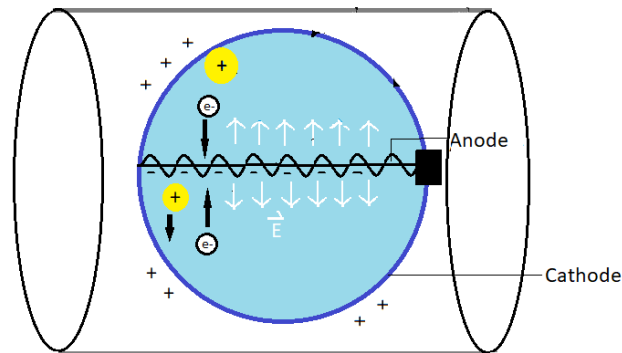


Figure 3. The electrons are accelerated and attracted toward the anode under the electric field inside the TEPC detector.

Because the applied voltage of a TEPC is in the proportional region (depending on the electric field strength), TEPC is above the threshold for gas multiplication (Sauli, 2014). The multiplication is linear. The voltage drops in the circuit is proportional to the total charge collected, proportional to the number of ion pairs created by the incoming radiation and to the energy deposited in the volume. The magnitude of the voltage drop is then amplified by the TEPC preamplifier, which transfers the signal to the pulse shaping amplifier to enhance and reshape the signal. Finally, the amplified signal reaches the spectrometer (Figure 2). The pulse signal is sorted and stored in each digital channel ( $i$ ) accordingly by the multi-channel analyzer

board (MCA) to produce a spectrum. The pulse amplitude (i.e., pulse height) is proportional to the amount of energy deposited in the TE volume. The pulse height spectrum can be converted to lineal energy distribution after proper lineal energy calibration.

In practice, the output TEPC spectrum must be corrected (extrapolated) to remove the electronic noise and “restore” the missed energy events below the TEPC threshold due to electronic limitations. A TEPC must be calibrated before it can accurately measure the radiation dose.

A typical lineal energy spectrum is shown in Figure 4 by exposing TEPC to a neutron source (*AmBe*, the activity was 1 Ci on the reference date of 04 November 2020). The spectrum shows four typical structures: 1. There is almost no signals detected below the electronic threshold. The threshold setting depends on the electronic components of the TEPC. 2. Three peaked areas, including gamma dose, proton dose and alpha dose refer to the dose contributions due to gamma rays, proton, and alpha rays respectively. 3. The fall at about  $8.55 \text{ keV}/\mu\text{m}$  is the electron edge and, 4. the fall at around  $176.25 \text{ keV}/\mu\text{m}$  is the proton edge. A proton-edge and electron-edge structures are produced when deposited energy reaches its corresponding maximum values for electrons and protons respectively (Endo, 2009). The proton- and electron-edges are useful in the lineal energy calibration, which will be discussed later in section 3.1.

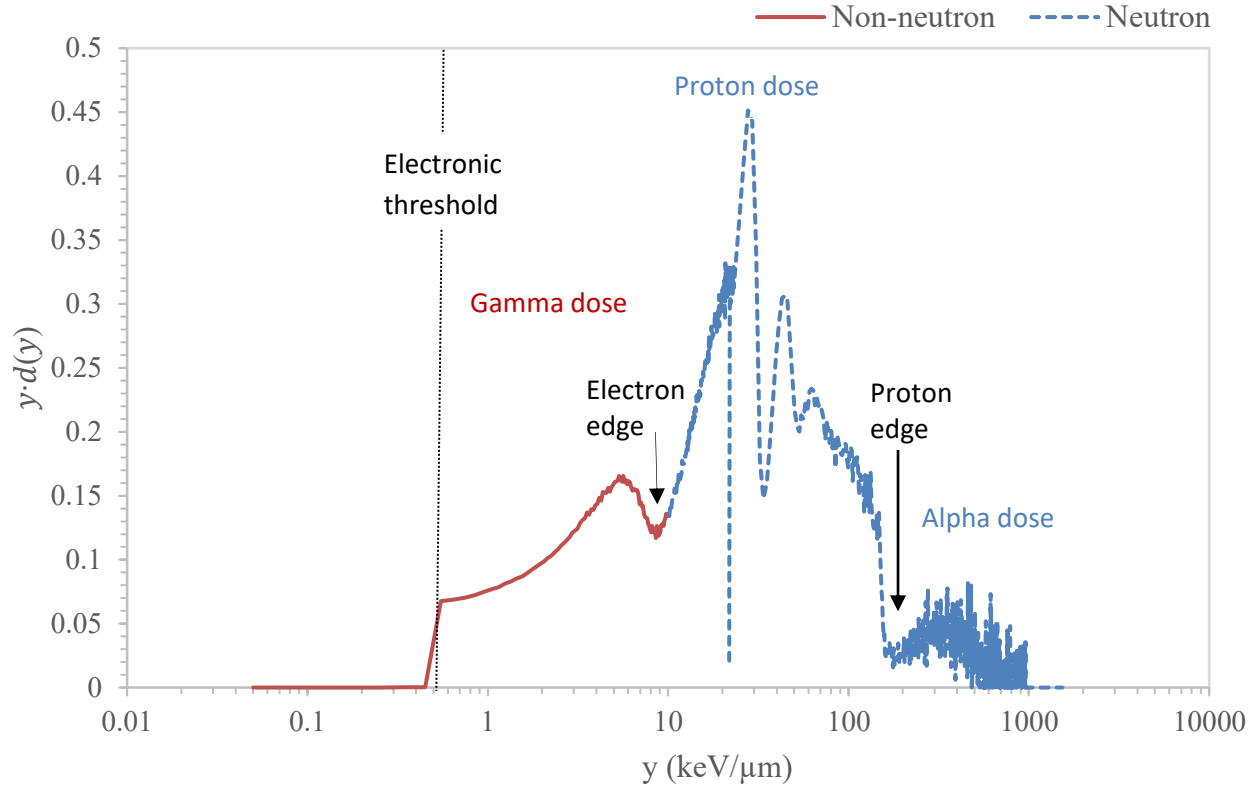


Figure 4. A typical lineal energy spectrum produced from a TEPC after exposure to *AmBe* source for 30 minutes.

In natural background radiation dose measurements, the region where the gamma doses located (usually from  $0 \text{ keV}/\mu\text{m}$  to  $10 \text{ keV}/\mu\text{m}$ ) are contributed from electrons, gamma rays and muon, i.e., non-neutron particles. Proton and alpha doses are located above  $10 \text{ keV}/\mu\text{m}$ , which are mainly contributed from cosmic neutron. As mentioned in section 1.2.2, lineal energy is the measurable quantity that can best estimate LET. In practice, non-neutron or low LET radiation dose, is the sum of the dose contributions from terrestrial gamma radiation (TR) and non-neutron cosmic rays (Non-n. CR), which is:

$$H^*(10)_{\text{Low LET}} = H^*(10)_{\text{Non-n. CR}} + H^*(10)_{\text{TR}}$$

Equation 10

And the natural dose including the contribution from neutron (i.e., low LET + high LET) is:

$$H^*(10)_{Low\ LET} + H^*(10)_{High\ LET} = H^*(10)_{With\ n.\ CR} + H^*(10)_{TR} \quad \text{Equation 11}$$

Where With-n. CR standards for cosmic rays including neutron.

Equations 10 & 11 calculate the doses contributed from cosmic rays in the low LET or high LET spectra if the doses from terrestrial gamma rays are known. Equations 10 & 11 are fundamental in the experimental designs (Chapter 4). In this project, the  $H^*(10)_{TR}$  is measured by the Canada's Fixed Point Surveillance (FPS) spectrometers (RS250),  $H^*(10)_{Low\ LET}$  and  $H^*(10)_{High\ LET}$  are measured by TEPC.

## 1.4 HEALTH CANADA'S FIXED POINT SURVEILLANCE (FPS) NETWORK

### 1.4.1 Introduction to FPS

In Canada, Health Canada's Fixed Point Surveillance (FPS) network monitors airborne and terrestrial gamma radiation doses from both naturally occurring radiative material (NORM) and man-made sources. Since 2000, all 77 FPS stations have been completed across Canada (Health Canada, 2015). As shown in Figure 5, the FPS stations are mainly located in major population centres, near the nuclear-powered plants and ports that berth nuclear powered vessels. There is a

RS250/2<sup>6</sup> Sodium Iodide (NaI (Tl), model RS250) spectrometer in each FPS station. The system reports near real time radiation dose in Air Kerma<sup>7</sup> and  $H^*$ (10).

In addition to routine monitoring, special event assessments rely on the FPS RS250 post-accident measurements, for example the Fukushima accident, DPRK nuclear tests, forest fires etc. Since 2015, the potential to establish a Nationwide Cosmic-ray Dose Monitoring System with the current FPS Network has been explored and discussed (Liu & Zhang, 2018). This project is a part of the Nationwide Cosmic-ray Dose Monitoring Network Project.

---

<sup>6</sup> Some station has equipped with the new version RS252. RS252 and RS250 function the same. In the project, the RS250/2 is simplified as RS250.

<sup>7</sup> Air Kerma is defined as the kinetic energy released per unit mass.



Figure 5. The stations of the Health Canada’s Fixed Point Surveillance (FPS) Network<sup>8</sup> (Health Canada, 2015)

<sup>8</sup> The RS250/2 detectors are located in population centre, near the nuclear plants and ports labelled by purple pins. Some stations also installed the newer version, i.e., RS252. FPS stations in each province are labelled by colored dots: NU: pink, NT: yellow, YT: orange, BC: blue, AB: purple, SK: grey, MB: amber, ON: white, QC: black, NB: red, PE: brown, NS: green, NL: olive.

#### *1.4.2 FPS Spectrometer (RS250) and the Analytical Model*

As mentioned in section 1.4.1, there is a RS250 spectrometer in each FPS station, which employs  $3 \times 3''$  thallium-activated sodium iodide (NaI (Tl)) as scintillators for gamma ray detections. RS250 reports near real-time gamma doses and is engaged in the routine terrestrial radiation monitoring because it can be self-stabilized on naturally occurring isotopes and tolerate the extreme weather in Canada. RS250 can function well at temperatures as high as 50 °C and as low as -40 °C (Radiation solutions Inc., 2020).

When the RS250 is exposed to natural radiation, the incoming radiation strikes the scintillator crystal, releasing electrons and ionizing the medium. The crystal rapidly de-excites by emitting photons (light), light is then guided to the photomultiplier tube (PMT) and strikes the photocathode of the PMT. Electrons are ejected and results in multiplication of the current (Radiation solutions Inc., 2020). The number of electrons is proportional to the amount of energy lost by radiation interacting with the scintillator, so the amplitude of the output voltage pulse is proportional to the energy (Glascock, 2014). The MCA<sup>9</sup> amplified and digitized the pulse signals into channels to produce an energy spectrum (Figure 6).

---

<sup>9</sup> The model of MCA employed in RS250 is the advanced digital spectrometer (ADS).

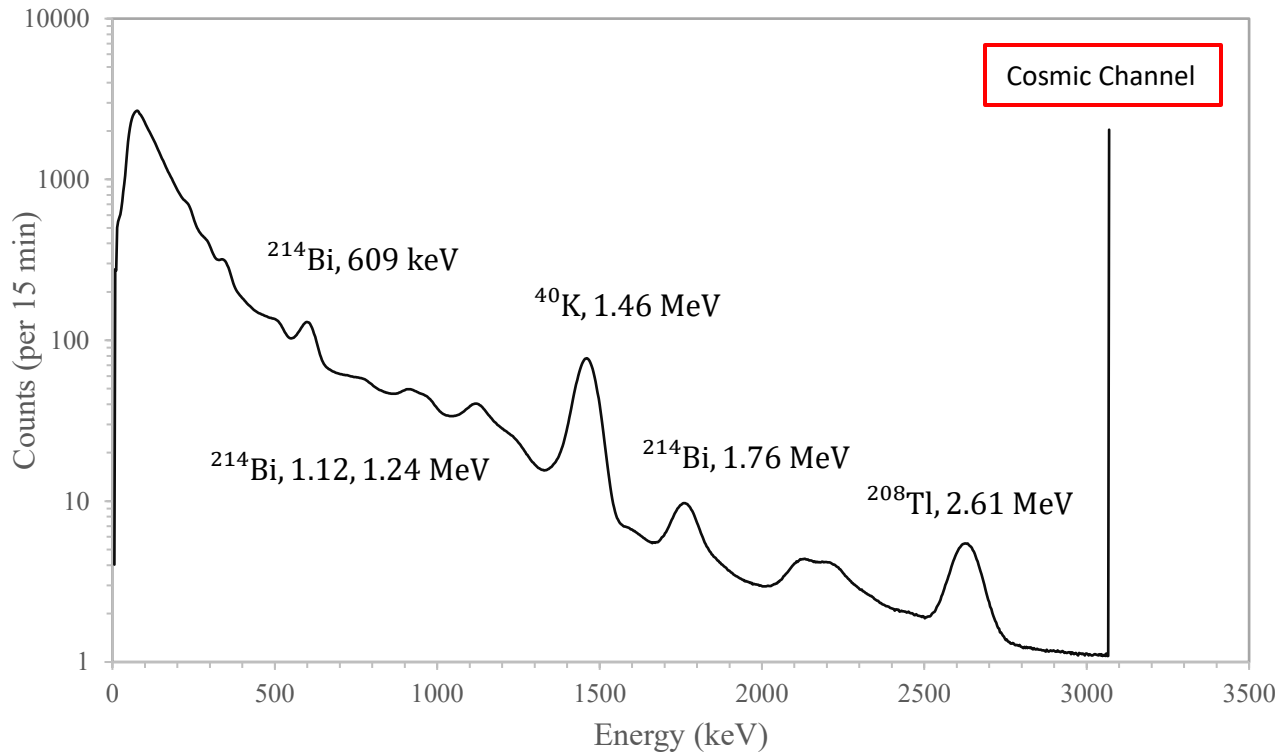


Figure 6. A typical 15 min energy spectrum produced from RS250 at the Ottawa FPS station (Radiation Protection Bureau).

RS250 can provide accurate dose measurements from a full gamma spectrum (0-3 MeV) and differentiate the sources of radiation. For example, some common radioactive isotopes, including bismuth-214 ( $^{214}\text{Bi}$ ), thallium-208 ( $^{208}\text{Tl}$ , from decay of uranium-232), and potassium-40 peaks are found in the spectrum from 0-3 MeV. Figure 6 shows a typical 15-minute spectrum measured by RS250 at the Ottawa FPS station. The energy spectrum can be separated to two regions. First, from 0-3 MeV, the counts are mainly contributed from the terrestrial radiation<sup>10</sup> (TR).

$H^*(10)_{TR}^{RS250}$  can be gained based on the pre-determined calibration curve, which converts

<sup>10</sup> About 3 mSv/h is contributed from the cosmic radiation in the region (0 to 3 MeV) and will be considered in the calculations later (Liu & Zhang, 2018).

energy spectrum to dose rates. Second, above 3 MeV, the counts are collected in the overflow channel. It is also called Cosmic Channel (CC) in this project because in the natural background radiation doses measurements at ground level, few or no signals are contributed from gamma rays above 3 MeV, i.e., it is predominantly contributed from the non-neutron cosmic rays (Non-n. CR) counts in a 15-minute period, i.e.,  $N_{CC}^{RS250}$  (Liu & Zhang, 2018).

To establish the Cosmic-ray Dose Monitoring System with the current FPS network, the essential step is to convert the counts in the cosmic channel (CC in RS250) to  $H^*(10)$ . The following describes the proposed model for converting the  $N_{CC}^{RS250}$  to  $H^*(10)_{CR}^{RS250}$ , which was previously developed by the Radiation Protection Bureau (RPB) of Health Canada and has never been tested before. The analytical model was developed to calculate the cosmic radiation dose in terms of  $H^*(10)$  in 3 steps. First, the simulated  $H^*(10)$  at 77 FPS stations were obtained based on the Excel-based Program for Calculating Atmospheric Cosmic Ray Spectrum (EXPACS) and its analytical model (PARMA). By inputting the corresponding information like altitude, latitude, longitude, time, and solar activity (W-index) et al., the Monte Carlo Simulation program, EXPACS, can generate the cosmic radiation dose in terms of  $H^*(10)$  anywhere in the world (Sato, 2015). Second, the counts from the CC channel of RS250 at the 77 FPS stations were collected.

Then the correlations between the CC counts and the simulated  $H^*(10)$  results were found (Liu & Zhang, 2018): The  $H^*(10)$  contributed from the non-neutron cosmic ( $H^*(10)_{Non-n. CR}^{RS250}$ ) can be calculated from the CC counts as:

$$H^*(10)_{Non-n. CR}^{RS250} = 0.0148 \cdot n_{CC}^{RS250} + 5.3323 \quad \text{Equation 12}$$

Where Non-n. CR standards for non-neutron cosmic rays. And the ambient dose equivalent including neutron  $H^*(10)_{With n. CR}^{RS250}$  can be calculated from:

$$H^*(10)_{With n. CR}^{RS250} = 0.0297 \cdot n_{CC}^{RS250} - 14.7989 \quad \text{Equation 13}$$

Where With-n. CR standards for cosmic rays including neutrons.

The empirical equations 12 & 13 convert CC counts from RS250 to  $H^*(10)$ , which show the FPS network's potential as a cosmic radiation dose monitoring system (Liu & Zhang, 2018). However, before the actual implementation to all FPS stations, the two equations must be verified with experimental measurements, i.e., the goal of this project.

## 1.5 OBJECTIVES

The objective of the project is to calibrate and compare the dose results from the analytical model based on EXPACS and the RS250 cosmic channel (CC) with the experimental measurements from the reference instrument, which is the tissue equivalent proportional counter (TEPC). The TEPC was selected as the reference instrument because of its ability to separate the non-neutron (low LET<sup>11</sup>) and neutron (high LET<sup>12</sup>) spectrum and measure the  $H^*(10)$  based on the absorbed dose in mixed radiation fields.

The experimental  $H^*(10)$ s contributed from CR are employed to calibrate the analytical results from the empirical equations (Equation 12 and 13, Section 1.4.2). Specifically, after obtaining the experimental measurements in terms of dose equivalent ( $H$ )s from TEPC,  $H$ s are converted to  $H^*(10)$ s by multiplying a conversion coefficient (Equation 6, Section 1.2.2). The experimental non neutron CR  $H^*(10)$ s, i.e.,  $H^*(10)_{Non-n. CR}^{TEPC}$ , are equal to the low LET  $H^*(10)$ s, i.e.,  $H^*(10)_{LOW LET}^{TEPC} = f_1 \cdot H_{LOW LET}^{TEPC}$ , minus the  $H^*(10)$ s contaminated by the terrestrial radiation dose, i.e.  $H^*(10)_{TR}^{RS250}$ :

$$H^*(10)_{Non-n. CR}^{TEPC} = f_1 \cdot H_{LOW LET}^{TEPC} - H^*(10)_{TR}^{RS250} \quad \text{Equation 14}$$

Where  $f_1$  is the conversion coefficient for low LET spectrum.  $H^*(10)_{Non-n. CR}^{TEPC}$  is then used to calibrate and compare with the  $H^*(10)_{Non-n. CR}^{RS250}$ .

---

<sup>11 6</sup> In the RMC research, the low LET and high LET regions are set to 0-10 keV/ $\mu$ m and >10 keV/ $\mu$ m respectively (Lewis & Desormeaux, 2004). In the project, a new way to separate the low LET and high LET region was discussed in Section 3.4.

To calibrate and compare  $H^*(10)_{With\ n.\ CR}^{RS250}$ , the experimental  $H^*(10)$  including the neutron can be calculated from the equation:

$$H^*(10)_{With\ n.\ CR}^{TEPC} = f_1 \cdot H_{Low\ LET}^{TEPC} + f_2 \cdot H_{High\ LET}^{TEPC} - H^*(10)_{TR}^{RS250} \quad \text{Equation 15}$$

Where  $f_2$  is the conversion coefficient for high LET spectrum.

## 1.6 SUMMARY OF THE CONTENTS OF THIS WORK

Chapter 2 covers the principles and features of the TEPC (model HAWK), methodology employed in the data processing and the data analysis. Chapter 3 presents the calibration with standard and improved methods, the detailed process, and the corresponding results. The experiments designed to determine the ambient dose equivalent conversion coefficient and the cosmic radiation doses are presented in Chapter 4. Finally, Chapter 5 provides the general conclusions and discussion of this project, and the directions which could be necessary and worthy to be pursued in the future.

## 2 TEPC DATA PROCESSING AND ANALYSIS

---

### 2.1 INTRODUCTION TO HAWK TEPC

#### 2.1.1 *Introduction to HAWK TEPC*

The Rossi-type TEPC, a model HAWK, is commercially available at Far West Technology Inc. It is initially conceived for the Space Shuttle, the International Space Station (ISS) and Air-flight dosimetry (ICRP, 1991); and has been selected as the reference instrument in this project. Two versions, HAWK 2 & 3, were employed for data collection<sup>13</sup>. Figure 7 shows the picture of the TEPCs stored in the carry-on case (left: HAWK 2, right: HAWK 3). The front look of a HAWK TEPC is shown in the middle.

HAWK is simple to operate. HAWK can be either battery operated or connected to an external AC/DC power supply. Power is supplied from four 1.5 volts 'D' cell batteries during the cosmic ray dose measurements. The current operating voltage of HAWKs is -671 V. Full data spectra are stored every minute in a standard compact-flash memory card. After downloading and extracting the data to a PC, the ROM-DOS operating system is employed for data analysis. Counts, absorbed dose rate, dose equivalent rate is stored as text files (FWT, 2011).

---

<sup>13</sup> HAWK 3 is not used much in the project and will be used in the coincident experiment in the future. Because the preamp output of HAWK 3 was set to a value that bias the neutron signals but sacrificed some of the gamma signals, the experimental results from HAWK 3 are found on the low side.



Figure 7. The appearance of the HAWK TEPCs.

The construction details of HAWK TEPCs are shown in Figure 8. HAWKs are made in a cylindrical shape with 16 cm in diameter and 34 cm in length; they consist of the electronic compartments (spectrum analyzer system) on the left side of HAWK and the TE spherical sensitive volume on the right side. Both chambers are enclosed in 0.050 inch stainless steel<sup>14</sup>, and the weight of the whole TEPC is 4 kg (FWT, 2010). The electronic compartments contain the display, memory card, battery, MCA, and other electronic structures (Figure 8. A). There are two MCA cards available, which collect data into<sup>15</sup>: 1. high LET: from 0.05 keV/ $\mu\text{m}$  to 1535.25 keV/ $\mu\text{m}$  (1024 channels) and 2. low LET: from 0.05 keV/ $\mu\text{m}$  to 25.6 keV/ $\mu\text{m}$  (266 channels) (FWT, 2010). The counts are collected in one minute in each channel, and the spectrum is produced along the channel numbers.

<sup>14</sup> HAWK 3 upgrades the outer shell to aluminum and reduce the weight from 4 kg to 2 kg.

<sup>15</sup> HAWK TEPC version 2.0 was previously modified from 1.0 keV/ $\mu\text{m}$  to 1.5 keV/ $\mu\text{m}$ .

2.1.2 Detector Specification

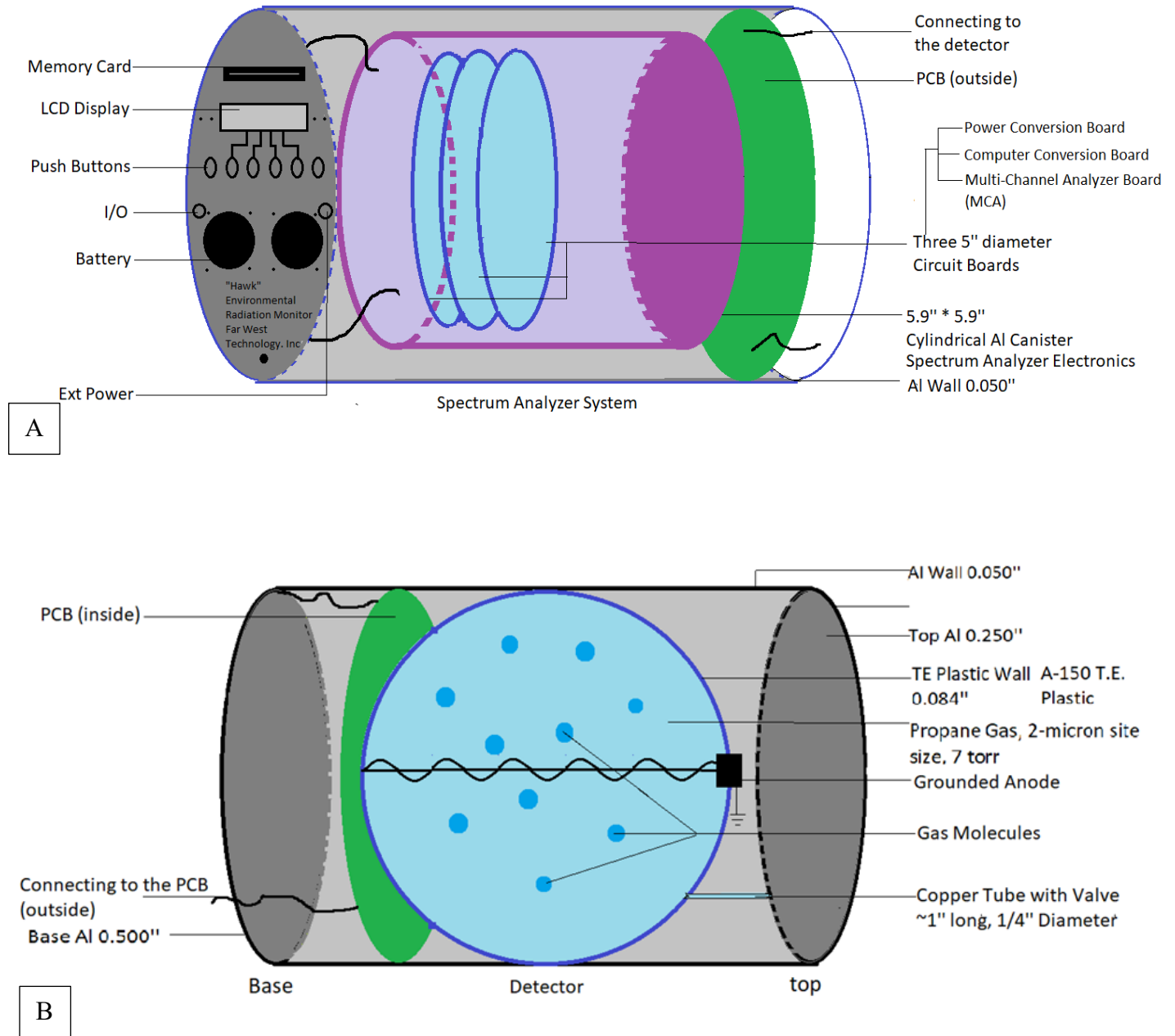


Figure 8. Diagram showing constructional details of the HAWK electronics (spectrum analyzer system) (A) and Rossi-type detector (B) chambers. The figures are drawn based on a general description given for HAWK TEPC.

The first Rossi-type TEPC was built in 1955 by Harald H. Rossi (Rossi & Rosenzweig, 1955). Since then, the low pressure tissue equivalent proportional counters have been developed to mimic the interactions and energy depositions in the microscopic tissue volumes at scales of the order of a few  $\mu\text{m}$  (FWT, 2010).

There is a spherical volume of 4.95'' in diameter surrounded by 0.21 cm thick plastic wall<sup>16</sup> in the detector chamber. The wall is made of A150 tissue (muscle) equivalent plastic, which is conductive and serves as the cathode. Pure propane gas, 7 Torr, is enclosed by the spherical plastic wall (Figure 8. B). The pressure of the gas inside the detector volume is very low. And atomic compositions of the TE wall and gas are similar to human muscle tissue<sup>17</sup> defined by ICRU. These features enable TEPC to simulate a spherical volume with a 2-micron site size. A wire anode passes along the centre of the spherical volume and is bounded by a fine helical wire to create a uniform electric field along the length of the anode (Anjomani, 2017). The entire detector is encased in the steel cylinder, which acts as a Faraday cage and provides electrostatic shielding (Conecici, 2017).

---

<sup>16</sup> A-150 TE wall is a conducting plastic with composition: 10.2 % H, 76.8 % C, 3.6 % N, 5.9 % O, 1.7 % F and 1.8 % Ca (Bianchi, 2017).

<sup>17</sup> The composition of human muscle: 10.1 % H, 11.1 % C, 2.6 % N, 76.2 % O (Bianchi, 2017).

## 2.2 DATA ANALYSIS

A series of pertinent equations are presented in the section to understand the process from the first signal to the final output. As discussed in Section 1.3, TEPC can measure the voltage drop in the circuit, which is proportional to the (kinetic) energy deposited in the detector chamber by the incoming ionizing particles. The built-in MCA analyzes the voltage drops, records the number of counts ( $n$ ) in each channel bin ( $i$ ) and produces a count versus voltage drop spectrum (Al-Bayati, 2012). Lineal energy,  $y$ , is the approximation of the energy deposited ( $\varepsilon$ ) in the TE volume by a charged particle per unit distance and is defined as  $y = \frac{\varepsilon}{\bar{l}}$  (Equation 8<sup>18</sup>). In other words, each lineal energy bin ( $y_{i=1,2,3,4,5\dots}$ ) is transformed from ( $\varepsilon_{i=1,2,3,4,5\dots}$ ) bin by using the mid-point value of  $\varepsilon_i$  divided by the mean chord length of the microscopic TE volume ( $\bar{l}$ ) (Figure 9). The procedures to calibrate the raw voltage drop spectrum to the lineal energy spectrum will be discussed later in Chapter 3.

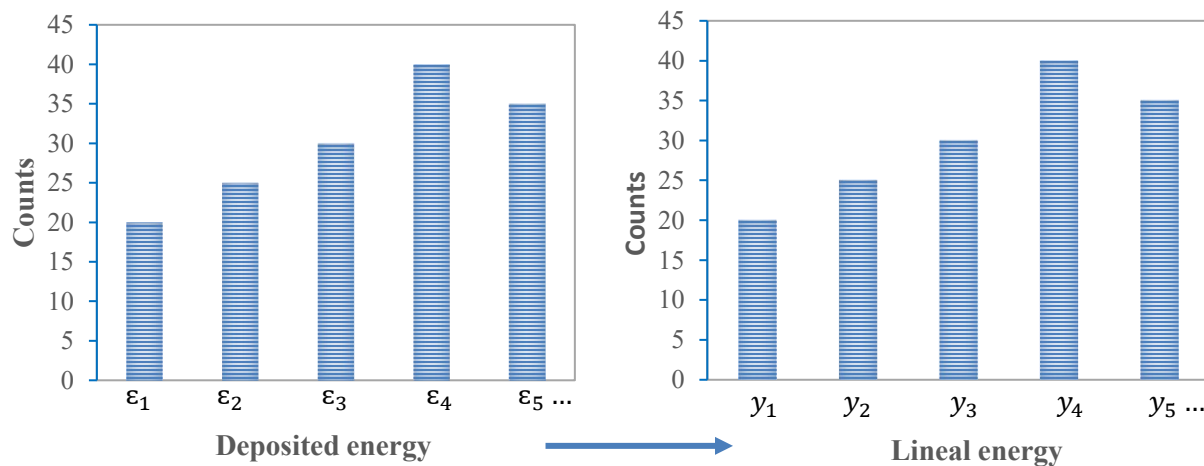


Figure 9. Qualitative illustration showing the conversion of energy spectrum to lineal energy spectrum after calibration.

<sup>18</sup>  $\varepsilon$  is the deposited energy by the incident particle and  $\bar{l}$  is the mean chord length.

From the lineal energy spectrum, the frequency-mean lineal energy ( $\bar{y}_f$ ) can be calculated:

$$\bar{y}_f = \frac{\sum_i y_i n(y_i)}{\sum_i n(y_i)} \quad \text{Equation 16}$$

Where  $y_i$  is the mid-point value of each lineal energy bin (i), and  $\sum_i n(y_i)$  is the total counts.

The dose-mean lineal energy ( $\bar{y}_D$ ) can also be calculated from the lineal energy spectrum:

$$\bar{y}_D = \frac{\sum_i y_i^2 n(y_i)}{\sum_i y_i n(y_i)} \quad \text{Equation 17}$$

The dose probability density or dose weighted distribution,  $d(y)$ , the fraction of total dose caused by events in the lineal energy between  $y_i$  and  $y_{i+1}$ :

$$d(y) = \frac{y \cdot f(y)}{\bar{y}_f} \quad \text{Equation 18}$$

The dose weighted lineal energy distribution (i.e., dose distribution)  $y \cdot d(y)$  versus  $y$  spectrum can be calculated from:

$$y \cdot d(y) = \frac{y^2 \cdot f(y)}{\bar{y}_f} \quad \text{Equation 19}$$

Because  $y \cdot d(y)$  is a normalized quantity, the spectrum is independent of the intensity of the radioactive source or the radiation field (Ali, 2014).

From equation 2 & 8 (section 1.2.2), the absorbed dose ( $D$ ) becomes:

$$D = \frac{d\varepsilon}{dm} = \frac{1.602 \times 10^{-13} \cdot \bar{l} \cdot \sum_i y_i n(y_i)}{m_{gas}} \quad \text{Equation 20}$$

Where  $1.602 \times 10^{-13}$  is a conversion constant ( $Gy$  to  $g \cdot keV^{-1}$ ),  $m_{gas}$  is the mass of the TE gas,  $\bar{l}$  is the mean chord length of TE volume,  $\sum_i y_i n(y_i)$  is the sum of the lineal energy (i.e., event size)  $y_i$  multiplied by the counts of the events that occurred over the entire spectrum. By using the definition of mean chord length,  $\bar{l} = 2d_s/3$ , and the physical relation  $m_{gas} =$

$\rho_{gas} V_{gas} = \pi \frac{d^3}{6}$  and  $d_s = \frac{d \cdot \rho}{\rho_s}$ ,  $D$  can be further simplified to:

$$D = \frac{0.204}{d^2} \sum_i y_i n(y_i) \quad \text{Equation 21}$$

Where  $d$  is the diameter of TE volume ( $1.27 \times 10^5 \mu m$ ).

Then the dose equivalent  $H$  can be calculated by using equation 3 & 21:

$$H = \frac{0.204}{d^2} \sum_i q(y_i) y_i n(y_i) \quad \text{Equation 22}$$

In practice,  $q(y_i)$  is assumed to be equal to the quality factor  $Q(L)$  given in ICRP 60 (ICRP 1991) (Section 1.2.3, Equation 5).

As mentioned in Chapter 1, the  $H^*(10)$  is utilized to get comparable results from the HAWK and RS250.  $H^*(10)$  is specific to the external radiation field, regardless of the type of detectors employed. The typical way to determine the ambient dose equivalent conversion factor is by calibrating TEPCs with poly-energetic neutron sources with known  $H^*(10)$ . In a recent study,

the Royal Military College of Canada (RMC) research group published the conversion coefficient and calculated the  $H^*(10)$  as followings (Lewis & Desormeaux, 2004):

$$H^*(10)_{Non-n. CR}^{TEPC} = \frac{1}{1.05} \cdot H_{Low LET}^{TEPC} - H^*(10)_{TR}^{RS250} \quad \text{Equation 23}$$

$$H^*(10)_{With n. CR}^{TEPC} = \frac{1}{1.05} \cdot H_{Low LET}^{TEPC} + \frac{1}{1.25} H_{High LET}^{TEPC} - H^*(10)_{TR}^{RS250} \quad \text{Equation 24}$$

Where  $\frac{1}{1.05}$  and  $\frac{1}{1.25}$  are the ambient dose equivalent conversion coefficients for low LET and high LET respectively. The RMC ambient dose equivalent conversion coefficients will be applied in the project (Section 4.2).

## 2.3 UNCERTAINTIES AND CORRECTIONS

### 2.3.1 Inherent Statistical Counting Uncertainty

The radioactive decays for natural radioactive particles are governed by the Poisson distribution (Vasconcelos, 2019). The standard deviation can be calculated from the equation:

$$\sigma_n = \sqrt{n} \quad \text{Equation 25}$$

Where  $n$  is the number of counts and  $\sigma$  is one standard deviation based on Poisson statistics. The count rate and the absorbed dose are dependent on the summation of counts, the uncertainties associated can be calculated by using error propagation (Taylor, 1996). The count rate is equal to the total counts ( $N = \sum_i n_i$ ) in a specific period ( $t$ ) with the unit in counts per second ( $cps$ ), the equation is:

$$\text{Count rate} = \frac{N}{t} \pm \frac{\sigma_N}{t} = \frac{N}{t} \pm \frac{\sqrt{N}}{t} \quad \text{Equation 26}$$

The absorbed dose  $D$  is equal to the summation of counts in each lineal energy channel  $i$ , so the error propagation equation is:

$$\sigma_D = \frac{0.204}{d^2} \sqrt{\sum_i y_i^2 \sigma_{n(y_i)}^2} \quad \text{Equation 27}$$

Where  $d$  is the diameter of the TEPC detector,  $y$  is the lineal energy. The only difference between the absorbed dose  $D$  and dose equivalent  $H$  is the quality factor in each channel:  $q(y_i)$ , the uncertainty on dose equivalent becomes:

$$\sigma_H = \frac{0.204}{d^2} \sqrt{\sum_i q(y_i)^2 \sigma_{n(y_i)}^2} \quad \text{Equation 28}$$

Where the quality factor used in the project is recommend by the ICRP 60 (Equation 5) and the uncertainties on the quality factor is neglected.

The uncertainty on the HAWK ambient dose equivalent is equal to the uncertainty of the dose equivalent multiply the ambient dose equivalent conversion coefficient  $f$ :

$$\sigma_{H^*(10)} = f \cdot \sigma_H \quad \text{Equation 29}$$

The RS250 ambient dose equivalent is an analytical value based on the counts  $n$ , so the equations of the uncertainties are:

$$\begin{cases} \sigma_{H^*(10)_{Non-n. CR}^{RS-250}} = 0.0148 \cdot \sigma_n = 0.0148 \cdot \sqrt{n} & \text{Non - n. CR} \\ \sigma_{H^*(10)_{With-n. CR}^{RS-250}} = 0.0297 \cdot \sigma_n = 0.0297 \cdot \sqrt{n} & \text{With n. CR} \end{cases} \quad \text{Equation 30}$$

Where the parameters 0.0148 and 0.0297 are the analytical coefficients for doses contributed from non-neutron cosmic rays (non-n. CR) and cosmic rays, including neutron (with n. CR) respectively (discussed in Section 1.4.2, Equation 12 & 13).

### 2.3.2 *Deadtime Correction*

Dead-time (DT) induced error is the other major contributor to TEPC dosimetric uncertainties. The dead time refers to the time after each event during which the detector cannot detect another event (Leo, 1994). The count rate of TEPC must be kept below 1000 counts per second (cps)<sup>19</sup> to avoid the distortion of signals and subsequent loss of information. Above 1000 cps (i.e., high dose rates), DT becomes significantly large, DT factor must be applied to correct the signal output (i.e., dose equivalent) (FWT, 2011). The equation of the HAWK dead-time correction factor is recommended in the operational manual (FWT, 2010) as follows:

$$DT \text{ factor} = \frac{1}{1 - (6.42 \cdot 10^{-5} \cdot n)} \quad \text{Equation 31}$$

Where  $n$  is the total counts in per seconds (cps). The dose equivalent can be corrected after multiplying by the DT factor.

---

<sup>19</sup> The maximum count rate of HAWK is 1000 counts per second (cps) and can be increased to 5000 cps after dead-time losses correction (FWT, 2011).

### 3 TEPC CALIBRATION WITH IMPROVED METHODS

---

The pulse height of a single energy deposition event by ionization is measured in TEPCs, and its amplitude is proportional to the amount of energy deposition. The raw pulse height, which is digitized to channel number by the MCAs, only be expressed in lineal energy if an appropriate calibration factor is applied. The chapter, section 3.1, shows the principles and process involved in the TEPC lineal calibration. Section 3.2 presents the procedures to generate the dose distribution spectrum. After the lineal energy calibration, the extrapolation method is needed to correct the output spectrum to cancel the electronic noise and include the missed energy events below the TEPC threshold due to electronic limitations. In section 3.3, the necessity, methods, and steps to extrapolate below the TEPC electronic threshold are presented. To accurately measure the doses contributed from natural background or cosmic radiation dose, two methods were employed in the project (MD-1 and MD-2). MD-1 & MD-2 made improvements on the extrapolation below the threshold, and on the separation between the low LET and high LET spectra. Section 3.4 describes the new way to separate the spectra contributed from non-neutron and neutron particles in the region around  $10 \text{ keV}/\mu\text{m}$ .

### 3.1 LINEAL ENERGY CALIBRATION

#### 3.1.1 *Manufacturer Setting*

HAWK 2 and HAWK 3 were calibrated by Far West Technology (FWT) in 2019 and 2020 respectively. The suggested calibration uncertainty is about 5 % (FWT, 2016). The calibration factor is  $1.5 \text{ keV}/\mu\text{m}$  per high LET channel and  $0.1 \text{ keV}/\mu\text{m}$  per low LET channel, set by the manufacturer.

#### 3.1.2 *Proton and Electron Edge Calibration*

##### 3.1.2.1 *Proton and Electron Edge*

The most common calibration method for TEPC is to use the proton edge as a marker point (Moro & Chiriotti, 2015). In TEPC, when incident neutrons strike the TE wall and produce recoil protons, these charged particles ionize the gas molecules and deposit energy in the TE volume.

The energy ( $\Delta E$ ) that a charged particle can deposit is  $\Delta E = \frac{dE}{dl} \Delta l$ , where  $\Delta l$  is the particle's path length and  $\frac{dE}{dl}$  is LET (defined in Section 1.2, Equation 1). The amount of energy deposited in a specific volume of matter cannot be infinitely large. Instead, it will reach to a theoretical maximum when both  $\Delta l$  and LET are at their maximum values<sup>20</sup>. Then the “edge” of the charged particle will be observed in the event-size spectrum. By using the lineal energy corresponding to the position in the event-size spectrum, a calibration factor can be calculated for the spectrum to convert all the “position” (i.e., channel number) to lineal energy. The proton-edge (p-edge) is

---

<sup>20</sup> Typically, the amount of energy deposited will reach the maximum when the particle travels through the centre of the simulated TE volume with the maximum lineal energy (or similarly the maximum stopping power) and stops exactly at the end of the spherical counter (Lindborg & Waker, 2017).

usually denoted around  $140 \text{ keV}/\mu\text{m}$  for propane TE gas in a  $2 \mu\text{m}$  simulated site sized TEPC (Endo, 2009).

Like neutrons, gamma rays knock out electrons in the TE wall, these electrons ionize the TE gas and deposit energy in the TE volume. Electrons will also create an “edge” in the event-size spectrum. The electron-edge (e-edge) is usually observed around  $10 \text{ keV}/\mu\text{m}$  for propane TE gas in a  $2 \mu\text{m}$  simulated site sized TEPC (Endo, 2009).

### ***3.1.2.2 Identifying the marker points of p- and e-edges by Moro & Chiriotti***

The calibration using p-edge or e-edge is feasible in radiation protection measurements, the only difficulty is to figure out what the lineal energy corresponds to the “edge”, i.e., the positions of p- and e-edges in the event-size spectrum. For example, some researchers identified the edge positions by using the middle point of the decreasing slope, some used the x-intercept after extrapolating the edge (Lindborg & Waker, 2017). In 2015, Moro & Chiriotti described the most precise method to identify the “edges” and calculate the calibration factor (More & Chiriotti, 2015). The uncertainty in the calibration was reported as around 3 % (Lindborg & Waker, 2017).

As mentioned in section 2.1, after the ionizations take place in TE volume, ion pairs are created, electrons are collected in the anode, the total charge is proportional to the voltage drops in the circuit. The magnitude of the voltage drop is then amplified and reshaped to pulse signals. The pulse signals are sorted and digitized in channel number (i) by the MCA. Then the event-size

spectrum ( $i \cdot d(i)$ ) (Equation 18 & 19) along the channel number ( $i$ ) was obtained utilized to perform the calibration (Moro & Chiriotti, 2015) in three steps. The first step is to identify a marker point. The marker point is required to select from the p-edge region of the ( $i \cdot d(i)$ ) spectra (the lineal energy is proportional to the pulse height and the counts in each channel ( $i$ )), which reveals the maximum possible energy deposited (Moro & Chiriotti, 2015). The shape of the p-edge region is like a shape reverse sigmoidal function due to energy-loss straggling. The p-edge region is fitted with a Fermi-like function, which is a common technique in TEPCs' calibration (Bianchi, 2021) (Moro & Chiriotti, 2015):

$$i \cdot d(i) = \frac{A}{1 + \exp(B \cdot (i - C))} \quad \text{Equation 32}$$

Where A is the upper asymptote parameter, parameters B and C are unitless.

Three marker points, including the abscissa of the inflection point  $i_{flex}$ , the abscissa of the second derivative maximum  $i_{\delta\delta}$ , and the intercept of the tangent through the inflexion point with the x-axis (channel)  $i_{TC}$ , are determined by the three equations below:

$$i_{flex} = C \quad \text{Equation 33}$$

$$i_{\delta\delta} = \frac{\ln(2 + \sqrt{3})}{B} + C \quad \text{Equation 34}$$

$$i_{TC} = \frac{2}{B} + C \quad \text{Equation 35}$$

The second step is to get a specific lineal energy value ( $y_{p-edge}$ ) and assign to the marker point  $i_{TC}$ . The lineal energy value is usually determined by exposing TEPC to a neutron source with

specific energy (Bianchi & Mazzucconi, 2021). In the last step, a calibration factor is obtained by using  $y_{p-edge}$  divided by  $i_{TC}$ . Then the calibration factor is compared to the factory settings from FWT.

### 3.1.2.3 Methods

HAWK 3 was recently calibrated by the manufacturer in 2020 and employed as the reference instrument in the calibration. To calibrate HAWK 2 in our lab, the man-made neutron-gamma source Americium-Beryllium (*AmBe*) was used. The *AmBe* source is a double-encapsulated stainless steel source, stable with a homogeneous active element. The activity of *AmBe* was 1 Ci ( $3.70 \times 10^4$  MBq) on the reference date of 04 November 2020. The experimental measurements were taken with HAWK 2 & 3 at the Canadian Nuclear Safety Commission (CNSC) laboratory. Because the energy of *AmBe* was not provided, the  $y_{p-edge}$  value used in the calibration was obtained from the HAWK 3 dose distribution spectra (i.e.,  $1.5 \cdot i_{TC}$  for high LET and  $1.0 \cdot i_{TC}$  for low LET).

As depicted in Figure 10, the *AmBe* source is located 0.5 m perpendicularly from the center of the spherical volume of TEPC. And the source and HAWK 2 were placed on one meter high wood stand. After the instruments were secured, the detector unit was turned on, the measurements were recorded for 3 hours, and the data were stored in the SD card. The same procedures were repeated for the HAWK 3. Then the source was relocated to 1.0 m away from both HAWK 2 & 3 detectors. The HAWKs were exposed to the same *AmBe* source with the new distance for 16 hours. Two subsections below present the results of the high LET spectrum

by using the p-edge technique (Section 3.1.2.4), and the results of the low LET spectrum by using the e-edge method (Section 3.1.2.5).

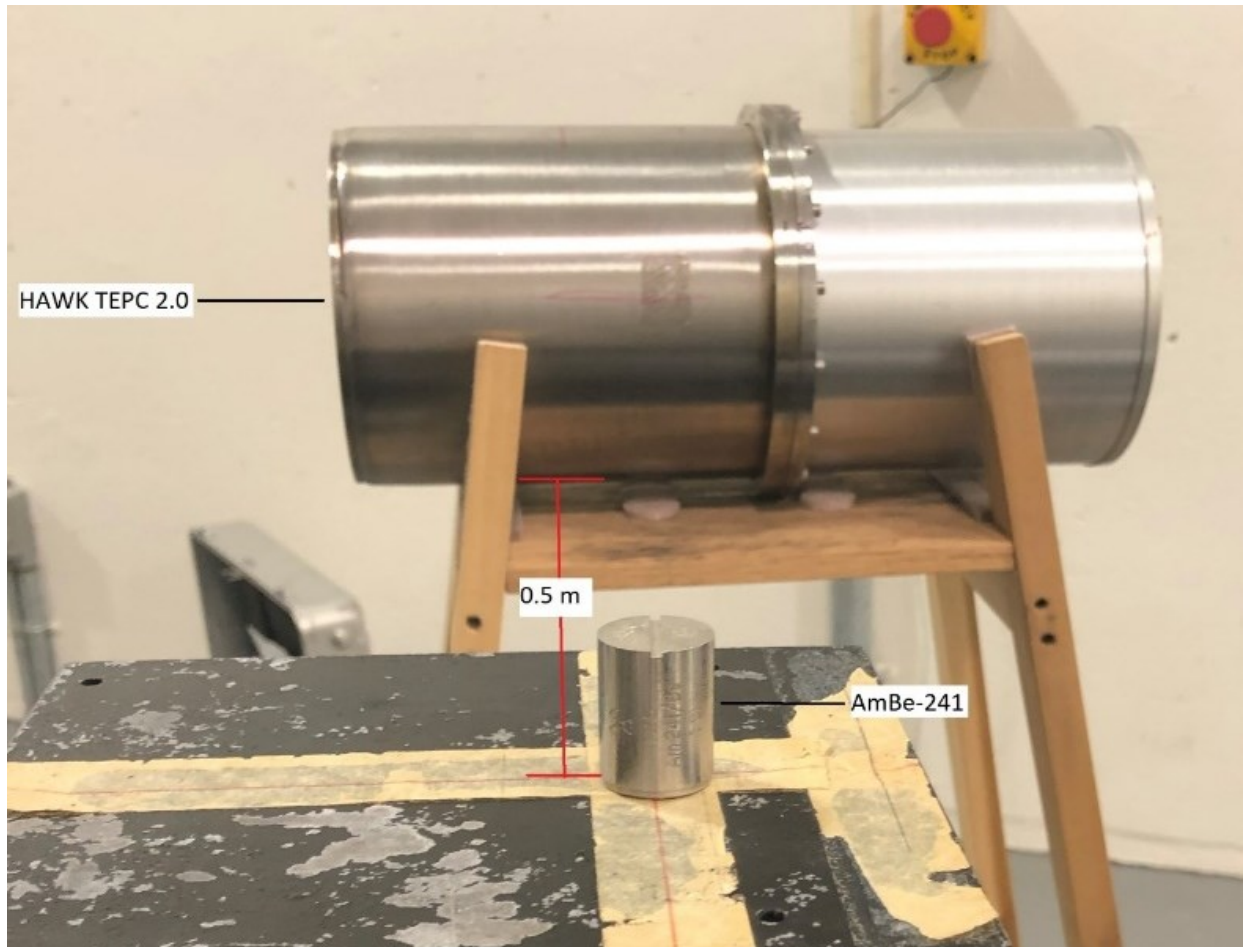


Figure 10. The experimental calibration set-up of HAWK 2 by exposure to a neutron source (*AmBe*).

### 3.1.2.4 Calibration results of the high LET spectrum

HAWK 2 detector was placed 0.5 m and 1.0 m away from the neutron source. The dose distributions spectra ( $i \cdot d(i)$ ) (Equation 18 & 19 with  $i$  instead of  $y$ ) along the channel number ( $i$ ) were obtained from the high LET measurements of HAWK 2 with two different distances: 0.5 m (labelled by red circles) and 1.0 m (labelled by blue dots) between the neutron source and detector (Figure 11). The two spectra (Hawk 2\_1.0 m and Hawk 2\_0.5 m) show similar patterns below channel 100. Above channel 100, the value of  $i \cdot d(i)$  gets larger when the detector was placed closer.

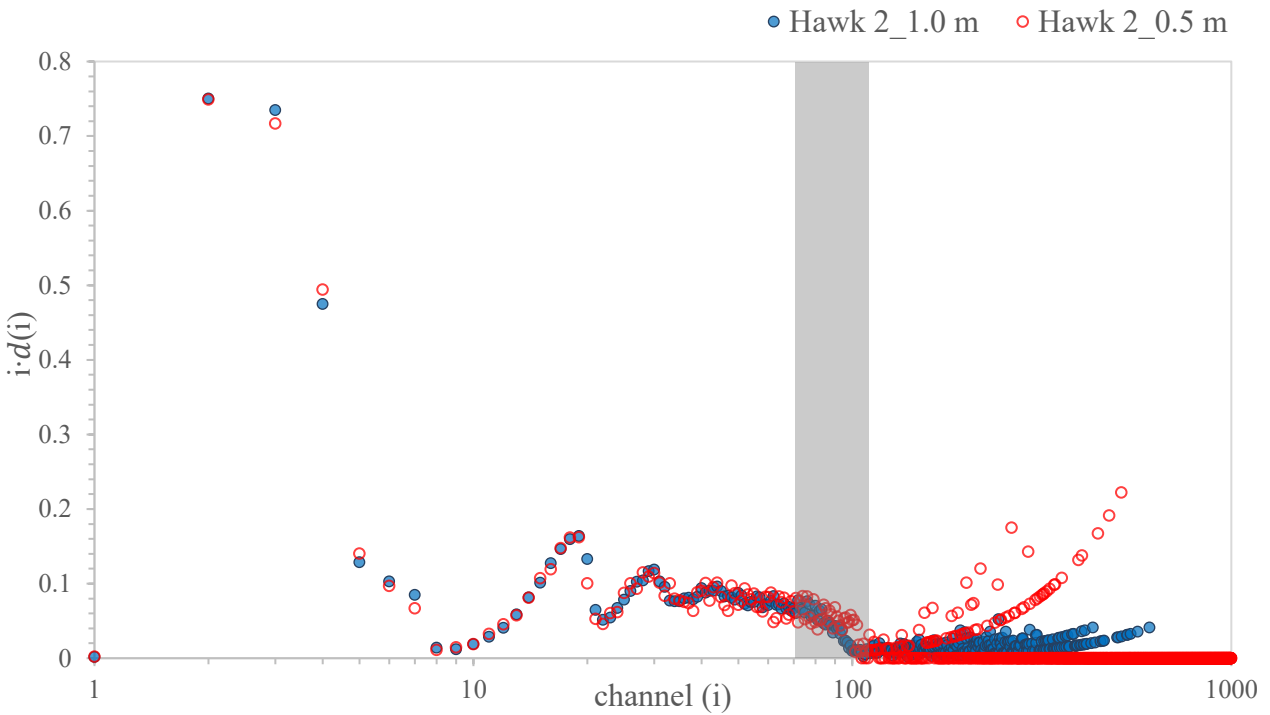


Figure 11. The *AmBe* high LET spectrum measured from the HAWK 2 TEPC at site size  $D = 2 \mu\text{m}$ . The proton edge region is highlighted by grey.

Figures 12 and 13 present the zoomed plots for the two distances 0.5 m and 1.0 m. The inflection point  $i_{flex}$ , the second derivative maximum  $i_{\delta\delta}$ , and the inflexion point  $i_{TC}$  were showed on the graph accordingly. In Figure 12, the fermi-like equations fit the measurements from channel 20 to 154, the correlation is 0.92 and the root mean square error, i.e., RSME is  $\pm 0.014$ . Figure 13 shows that the fermi-like equations fit the measurements very well from channel 20 to 154 (the correlation is 0.97 and RSME is  $\pm 0.0068$ ).

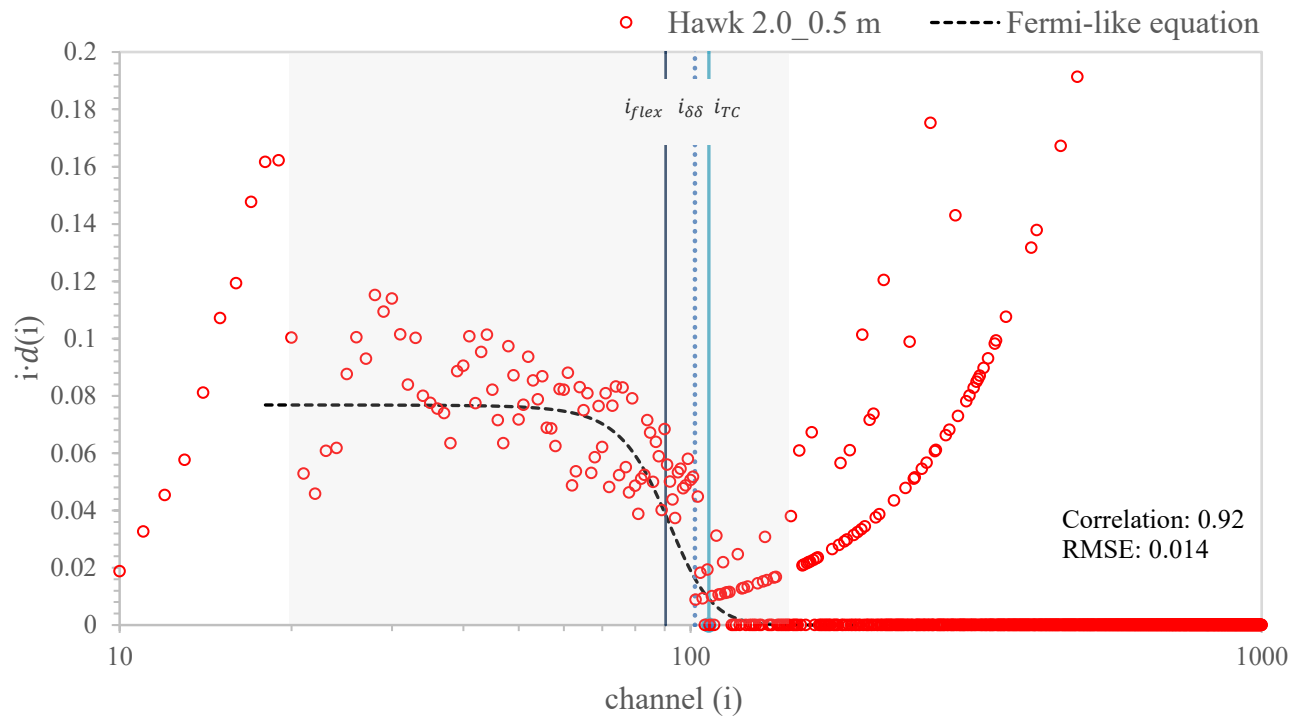


Figure 12. Zoomed neutron spectrum of the proton-edge region of Figure 11, generated from the measurements when detector and source are 0.5 m apart. A fermi-like function was fitted to the measured data in the grey region (channel 20 to 154).

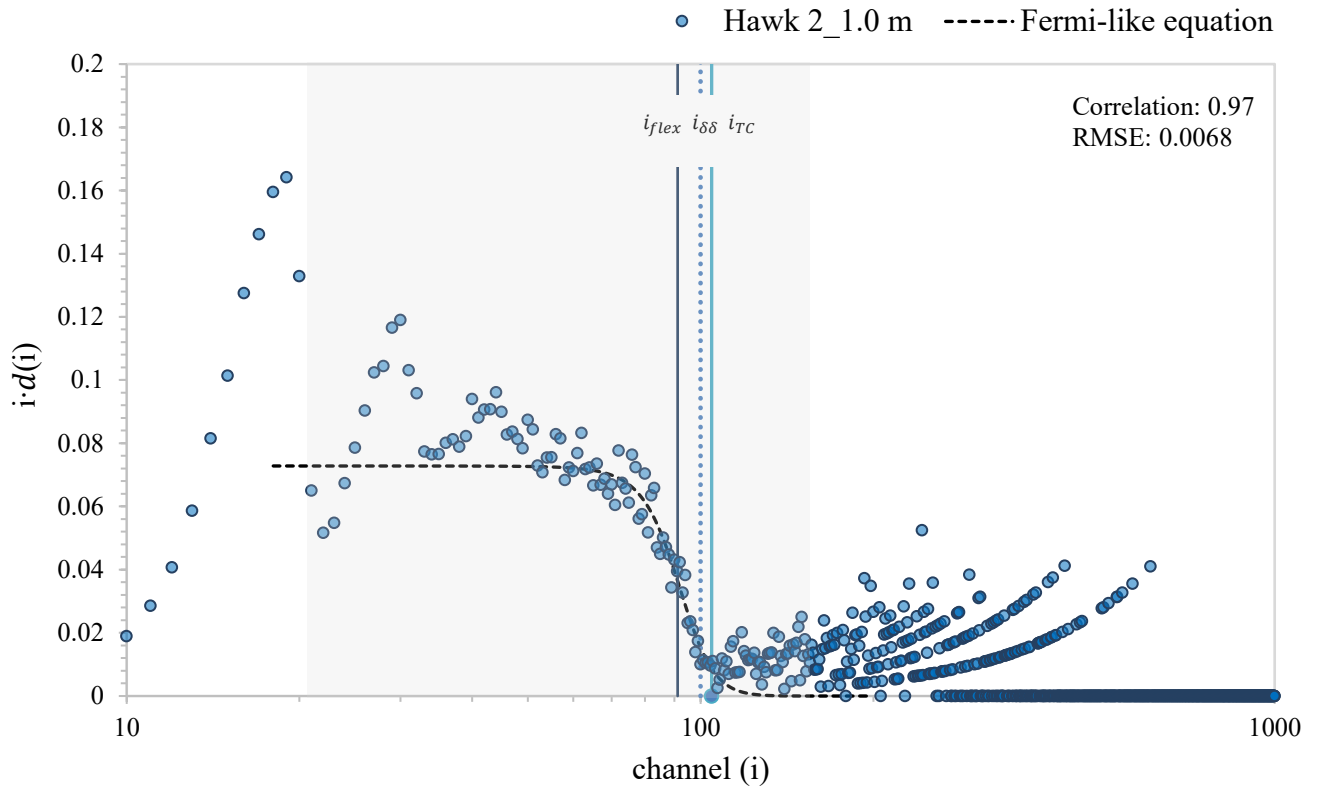


Figure 13. Zoomed view of the proton-edge region of the *AmBe* high LET spectrum (HAWK 2), generated from the measurements when detector and source are 1.0 m apart. A fermi-like function was fitted to the measured data in the grey region (channel 20 to 154).

Table 1 below shows the counts rate, the fitted fermi-like equations, the value of the three marker points and the calibration factor for both HAWK 2 and 3 with *AmBe* placed 0.5 m apart.

Similarly, the summaries are presented in Table 2 for the second distance (1.0 m).

Table 1. The summary table including the count rate, fitted fermi-like equation, the three marker points ( $i_{flex}$ ,  $i_{\delta\delta}$ ,  $i_{TC}$ ) and the calibration factor generated from the *AmBe* high LET spectrum at 0.5 m.

TEPC	HAWK 2	HAWK 3
Count rate (cps)	$201.76 \pm 0.14$	$185.95 \pm 0.13$
Fermi-like equation	$i \cdot d(i) = \frac{0.077}{1 + \exp(0.116 \cdot (i - 90.4))}$	$i \cdot d(i) = \frac{0.335}{1 + \exp(0.111 \cdot (i - 83.6))}$
$i_{flex}$	$90.4 \pm 1.2$	$83.6 \pm 1.9$
$i_{\delta\delta}$	$101.7 \pm 1.7$	$95.5 \pm 3.0$
$i_{TC}$	$107.6 \pm 2.1$	$101.7 \pm 4.0$
$y_{p-edge} (keV/\mu m)$	$152.6 \pm 9.7$	$152.6 \pm 9.7$
Calibration factor ( $keV/\mu m$ )	$1.418 \pm 0.094$	$1.500 \pm 0.075$

Table 2. The summary table including the count rate, fitted fermi-like equation, the three marker points ( $i_{flex}$ ,  $i_{\delta\delta}$ ,  $i_{TC}$ ) and the calibration factor generated from the *AmBe* high LET spectrum at 1.0 m.

TEPC	HAWK 2	HAWK 3
Count rate (cps)	$49.620 \pm 0.030$	$44.940 \pm 0.028$
Fermi-like equation	$i \cdot d(i) = \frac{0.073}{1 + \exp(0.150 \cdot (i - 91.17))}$	$i \cdot d(i) = \frac{0.357}{1 + \exp(0.132 \cdot (i - 85.82))}$
$i_{flex}$	$91.17 \pm 0.74$	$85.82 \pm 0.70$
$i_{\delta\delta}$	$99.9 \pm 1.1$	$95.8 \pm 1.2$
$i_{TC}$	$104.5 \pm 1.5$	$101.0 \pm 1.6$
$y_{p-edge}$ (keV/ $\mu$ m)	$152.6 \pm 9.7$	$152.6 \pm 9.7$
Calibration factor (keV/ $\mu$ m)	$1.460 \pm 0.095$	$1.500 \pm 0.075$

It shows that the distance doesn't affect the fitted equations significantly (Figures 12 & 13). For

example, the fitted fermi-like equation is  $i \cdot d(i) = \frac{0.077}{1 + \exp(0.116 \cdot (i - 90.4))}$  for HAWK 2\_0.5 m

spectrum (Table 1) and  $i \cdot d(i) = \frac{0.073}{1 + \exp(0.150 \cdot (i - 91.17))}$  for HAWK 2\_1.0 m spectrum (Table 2).

The calibration factor of HAWK 2 are  $1.418 \pm 0.094$  keV/ $\mu$ m and for  $1.460 \pm 0.095$  keV/ $\mu$ m at

0.5 m and 1.0 m respectively (Table 1 & 2). The calibration results are within the acceptable

range of the factory setting (i.e.,  $1.500 \pm 0.075$  keV/ $\mu$ m) (FWT, 2010). The *AmBe* high LET

spectra measured from the HAWK 3 TEPC are insignificant and presented in Appendix A,

Figure 55.

### 3.1.2.4 Calibration results of the low LET spectrum

Figure 14 shows the distributions of  $i \cdot d(i)$  versus the channel number from the low LET measurements of HAWK 2 exposed to  $AmBe$  at the distances of 0.5 m (HAWK 2\_0.5 m) and 1.0 m (HAWK 2\_1.0 m).

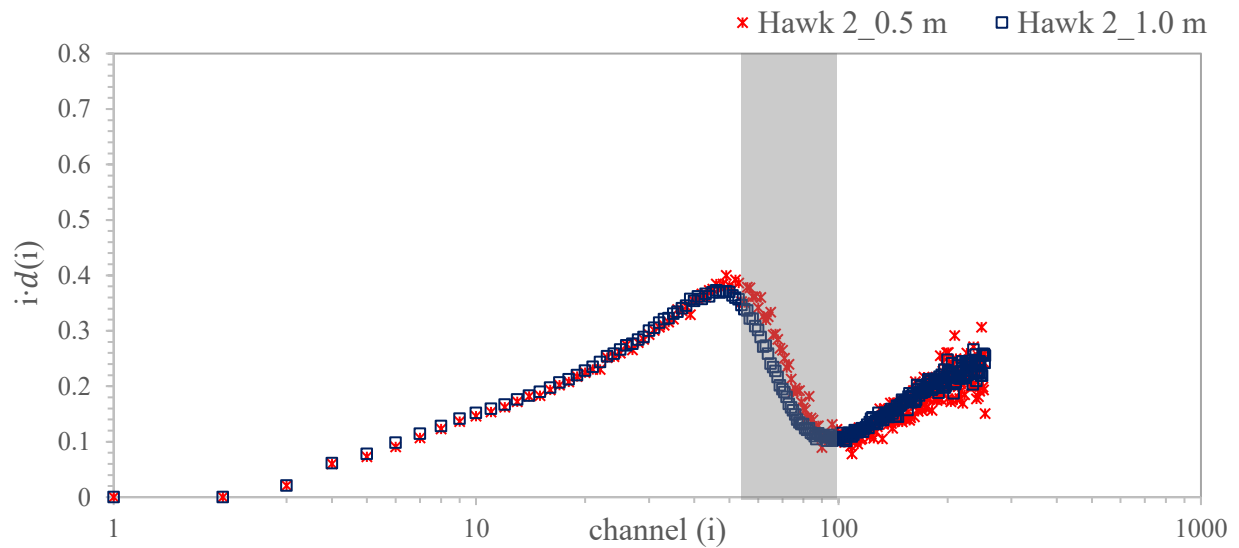


Figure 14. The  $AmBe$  low LET spectrum measured from the HAWK 2 at site size  $D = 2 \mu\text{m}$ . The proton edge region is highlighted by grey.

Figures 15 and 16 present the zoomed plots for the two distances 0.5 m and 1.0 m. The inflection point  $i_{flex}$ , the second derivative maximum  $i_{\delta\delta}$ , and the inflexion point  $i_{TC}$  were labelled on the graphs accordingly. Figure 15 shows the fermi-like equations fit the measurements from channel 50 to 93 (the correlation is 0.99 and RSME is  $\pm 0.014$ ). Figure 16 shows that the fermi-like equations fit the measurements very well from channel 50 to 93 (the correlation is 0.99 and RSME is  $\pm 0.0099$ ).

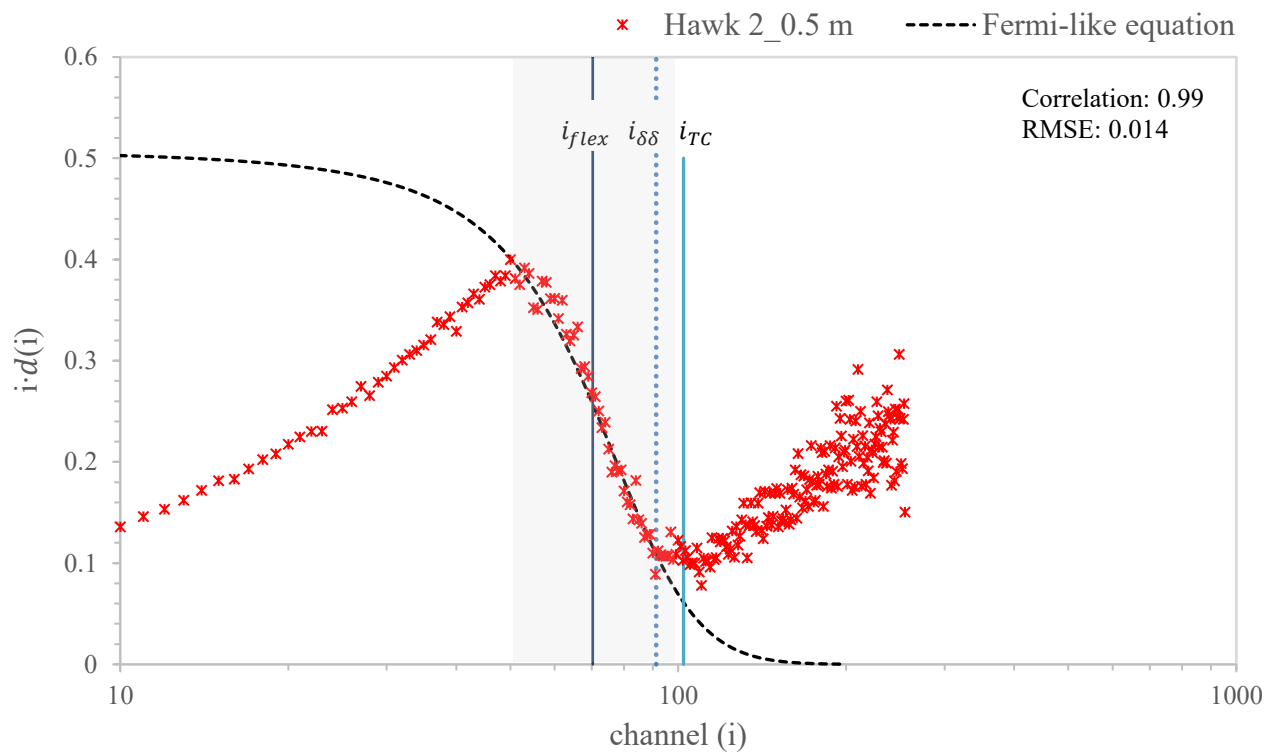


Figure 15. Zoomed view of the proton-edge region of the *AmBe* low LET spectrum (HAWK 2), generated from the measurements when detector and source are 0.5 m apart. A fermi-like function was fitted to the measured data in the grey region (channel 50 to 93).

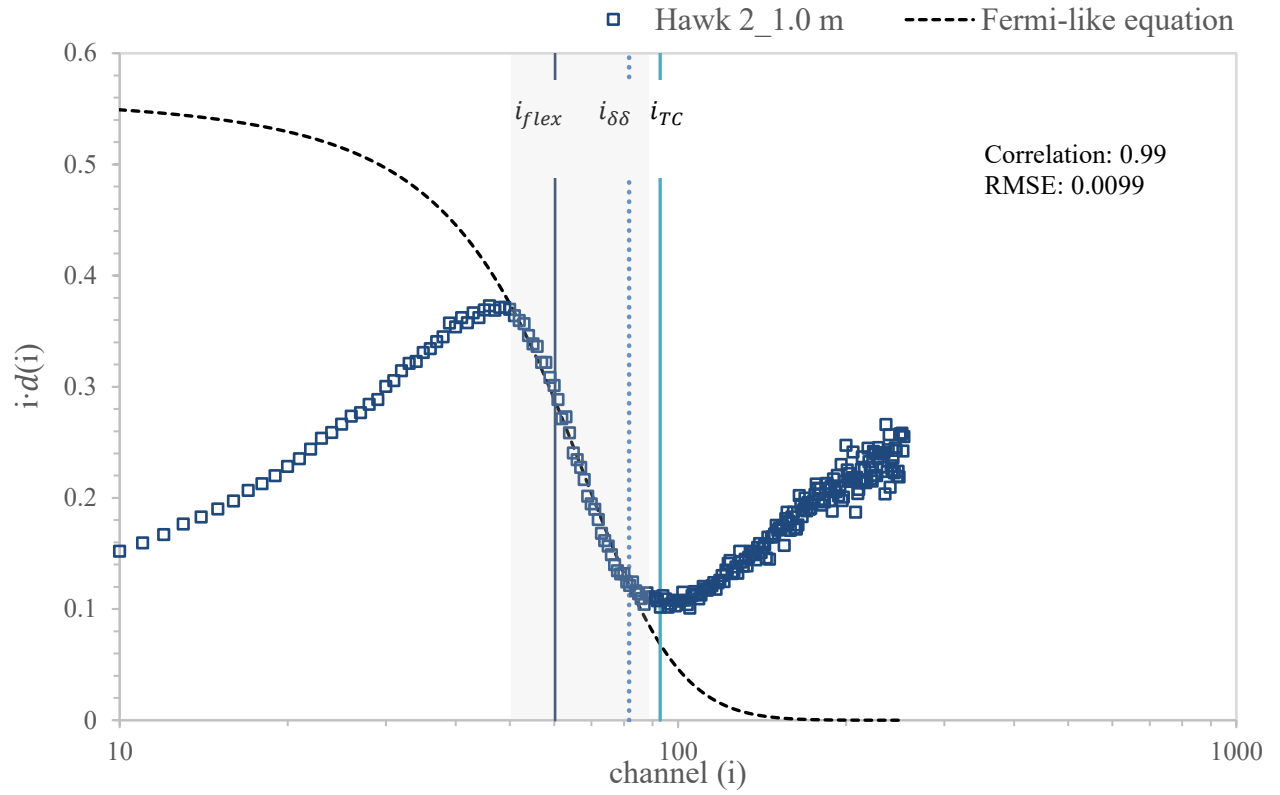


Figure 16. Zoomed view of the proton-edge region of the *AmBe* low LET spectrum (HAWK 2), generated from the measurements when detector and source are 1.0 m apart. A fermi-like function was fitted to the measured data in the grey region (channel 50 to 93).

Table 3 shows the counts rate, the fitted fermi-like equations, the value of the three marker points and the calibration factors of the low LET (ionizing, non-neutron) spectrum for both HAWK 2 and 3.

Table 3. The summary table includes the count rate, fitted fermi-like equation, the three marker points ( $i_{flex}$ ,  $i_{\delta\delta}$ ,  $i_{TC}$ ) and the calibration factor generated from the *AmBe* low LET spectrum at 0.5 m.

TEPC	HAWK 2	HAWK 3
Count rate (cps)	$201.76 \pm 0.14$	$185.95 \pm 0.13$
Fermi-like equation	$i \cdot d(i) = \frac{0.514}{1 + \exp(0.063 \cdot (i - 70.3))}$	$i \cdot d(i) = \frac{0.605}{1 + \exp(0.077 \cdot (i - 62.7))}$
$i_{flex}$	$70.3 \pm 2.6$	$62.7 \pm 2.0$
$i_{\delta\delta}$	$91.3 \pm 3.1$	$79.7 \pm 2.4$
$i_{TC}$	$102.2 \pm 3.7$	$88.6 \pm 2.8$
$y_{e-edge}$ (keV/ $\mu$ m)	$8.86 \pm 0.52$	$8.86 \pm 0.52$
Calibration factor (keV/ $\mu$ m)	$0.0867 \pm 0.0060$	$0.1000 \pm 0.0050$

Similarly, the summaries are presented in table 4 for the alternative distance (1.0 m). The distance doesn't play an important role in determining the fermi-like equation and calibration

factor. For example, the fitted fermi-like equations are  $i \cdot d(i) = \frac{0.514}{1 + \exp(0.063 \cdot (i - 70.3))}$  for HAWK

2\_0.5 m spectrum (Table 3) and  $i \cdot d(i) = \frac{0.575}{1 + \exp(0.061 \cdot (i - 60.2))}$  for HAWK 2\_1.0 m spectrum

(Table 4). The calibration factor of HAWK 2 are  $0.0867 \pm 0.0060$  keV/ $\mu$ m and for  $0.0954 \pm 0.0067$  keV/ $\mu$ m at 0.5 m and 1.0 m respectively (Table 3 & 4). Following the calibration by

using the e-edge technique, the uncertainties of the calibration factor are estimated to be less than 7 %. The calibration results of HAWK 2 agree with the manufacture,  $0.1000 \pm 0.0050 \text{ keV}/\mu\text{m}$  (FWT, 2010). The edge technique is feasible in determining the calibration factor.

Table 4. The summary table includes the count rate, fitted fermi-like equation, the three marker points ( $i_{flex}$ ,  $i_{\delta\delta}$ ,  $i_{TC}$ ) and the calibration factor generated from the *AmBe* low LET spectrum at 1.0 m.

TEPC	HAWK 2	HAWK 3
Count rate (cps)	$49.620 \pm 0.030$	$44.940 \pm 0.028$
Fermi-like equation	$i \cdot d(i) = \frac{0.575}{1 + \exp(0.061 \cdot (i - 60.2))}$	$i \cdot d(i) = \frac{0.553}{1 + \exp(0.098 \cdot (i - 64.0))}$
$i_{flex}$	$60.2 \pm 2.7$	$64.00 \pm 0.86$
$i_{\delta\delta}$	$81.7 \pm 3.1$	$77.4 \pm 1.1$
$i_{TC}$	$92.9 \pm 3.5$	$84.33 \pm 0.55$
$\gamma_{e-edge} \text{ (keV}/\mu\text{m)}$	$8.86 \pm 0.52$	$8.86 \pm 0.52$
Calibration factor ( $\text{keV}/\mu\text{m}$ )	$0.0954 \pm 0.0067$	$0.1000 \pm 0.0050$

The *AmBe* low LET spectra measured from the HAWK 3 TEPC are insignificant and presented in Appendix A, Figure 56.

## 3.2 DOSE DISTRIBUTION SPECTRUM

In HAWK TEPC, the events deposited in the TE volume span a wide range of energies from 0  $keV/\mu m$  to 1500  $keV/\mu m$ . Commonly in the natural background radiation dose measurements, numerous events are detected in the low LET (i.e., non-neutron) spectra, a few but very important events detected in the high LET spectra. The dose distribution spectrum, also called the microdosimetric spectrum, ( $y \cdot d(y)$ ), is employed to visualize the distribution of these energy deposition events.

### 3.2.1 *Generating the Dose Distribution Spectrum*

After converting the channel number ( $i$ ) to lineal energy ( $y$ ) by applying the calibration factor<sup>21</sup>, the low LET and high LET spectra ( $y \cdot d(y)$ ) are generated by using Equation 18 & 19 and combined to a total dose distribution spectrum by using a transition point (channel). Ideally, the sum of all counts from 0  $keV/\mu m$  to the transition point in the low LET spectrum should be equal to the sum of the same region in the high LET spectrum. The complete dose distribution spectrum consists of the low LET region (from 0  $keV/\mu m$  to the transition point with 0.1  $keV/\mu m$  per channel) and the high LET region (from the transition point to the last channel with 1.5  $keV/\mu m$  per channel). In practice, the selection of the transition point may be tricky because the addition of the counts in the low LET and high LET spectra from 0  $keV/\mu m$  to the transition point may not be exactly same to each other due to uncertainties (i.e., uncertainty in Poisson distribution). The best transition point will result in a minor difference between the two sums,

---

<sup>21</sup> The author designed but did not operate the calibration experiment during the pandemic. Considering the test conditions including the temperature, humidity, and the surrounding obstructs et al. during the calibration were not fully inspected, the results obtained from the calibration measurements are not used to generate the dose distribution spectra and calculate the  $H^*(10)s$ . Instead, the calibration factors recommended by the manufacturer were employed.

i.e., the less the difference between the two sums, the smoother the dose distribution curve.

Typically, the transition point is found to be around channel 210, which is equivalent to  $21.05 \text{ keV}/\mu\text{m}$  (FWT, 2010).

The dose distribution spectrum is commonly plotted on a logarithmic scale of  $y$  to show more structures over a wide range of lineal energy (i.e.,  $0 \text{ keV}/\mu\text{m}$  to  $1535.25 \text{ keV}/\mu\text{m}$ ). It also visualizes the fraction of the total absorbed dose delivered by events in each lineal energy bin. The area under the  $y \cdot d(y)$  curve is equivalent to the fractional dose, i.e., visual area under the curve is equal to its relative dose contribution. The high LET events (a few but important) can be immediately apparent because they are dose weighted (Section 2.2, Equation 19). In addition, because  $y \cdot d(y)$  is a normalized quantity, the dose distribution is independent of the intensity of the radioactive source or the radiation field applied (Ali, 2014).

### 3.2.2 The Complete Dose Distribution Spectrum

Figure 16 shows the complete dose distribution spectra of HAWK 2 measured at two different distances (0.5 m and 1.0 m) from the *AmBe* source after lineal energy calibrated. Below  $170 \text{ keV}/\mu\text{m}$ , the dose distributions measured at the two different distances are almost identical.

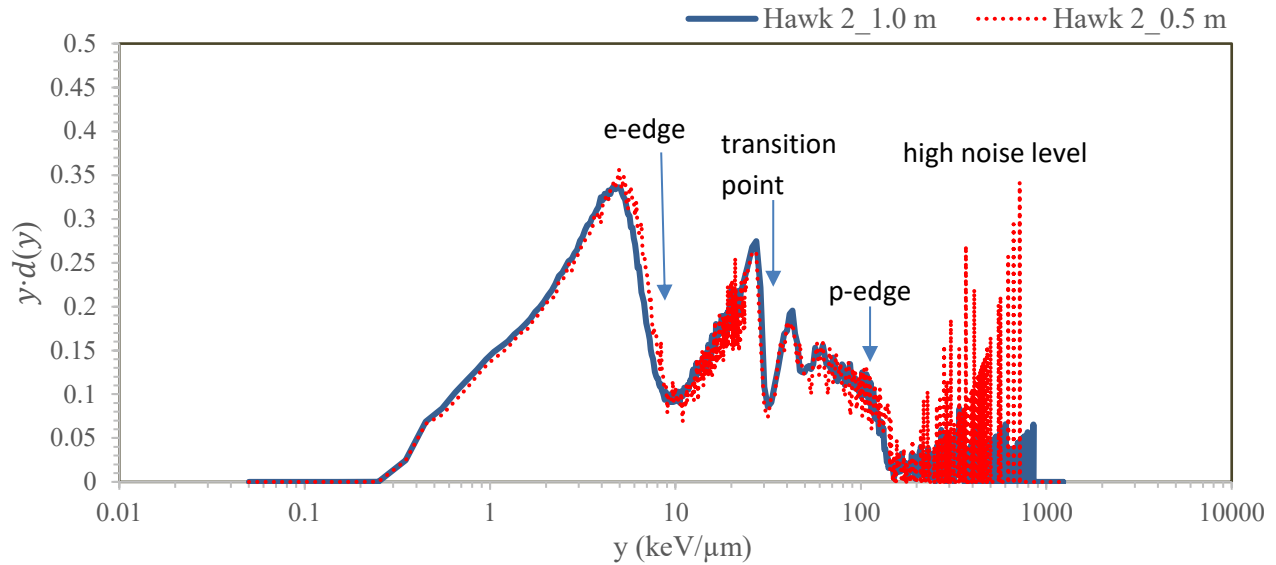


Figure 17. Dose distribution spectrum  $y \cdot d(y)$  measured at two different distances after the lineal calibration with the p-edge and e-edge techniques.

There are some typical structures shown in Figure 17. One is the e-edge located at around 10  $keV/\mu m$ . The second, the third peaks together with the p-edge (from approximately 10 - 150  $keV/\mu m$ ) are all contributed by the recoil protons. These split peaks indicate a poor selection of the transition point. The p-edge is located around 150  $keV/\mu m$ . In the dose distribution spectrum above 150  $keV/\mu m$ , the curve becomes a series of “spikes”, this is because in each high LET channel (bin), there are only one or two counts collected and heavily weighted by their dose (i.e.,  $y^2$ ). Above 170  $keV/\mu m$ , the (n,  $\alpha$ )- reactions dominate and an alpha edge should be visible, which is an “edge” at around 360  $keV/\mu m$  followed an exponential tail (Cruz, 2016). The alpha edge and exponential tail are expected in both spectra but not observed. Instead, the amplitude of the “peaks” increases with the lineal energy, which may be distorted by the high noise level. According to the manufacture (FWT, 2010), there are noise issues in HAWKs caused by high voltage (HV) breakdown, noise glitches on test pulsar inputs or ion discharge in the detector

when measuring low-energy radiation doses. The dose results calculated from the high LET spectrum will be evaluated further in the field experiments for cosmic ray doses measurement (Chapter 4).

### 3.3 EXTRAPOLATING BELOW THE ELECTRONIC THRESHOLD

#### 3.3.1 Electronic Threshold

Due to electronic limitations, all TEPCs have an electronic threshold (or called low LET threshold) in a low LET channel, below which almost no energy deposition events will be detected (Lillhok, 2007). Generally, the threshold may range from  $0.1 \text{ keV}/\mu\text{m}$  to  $0.5 \text{ keV}/\mu\text{m}$  in TEPCs. In the project, the HAWKs have a threshold of  $0.50 \text{ keV}/\mu\text{m}$  (FWT, 2016). In a typical dose distribution spectrum shown in figure 18, there is no dose distributed below  $0.25 \text{ keV}/\mu\text{m}$ . A sharp peak was observed in the last channel (from  $0.4 \text{ keV}/\mu\text{m}$  to  $0.5 \text{ keV}/\mu\text{m}$ ) right before the threshold, which may be caused by the electronic noise from  $0.4 \text{ keV}/\mu\text{m}$  to  $0.5 \text{ keV}/\mu\text{m}$ . The black dotted line indicates the threshold located at  $0.5 \text{ keV}/\mu\text{m}$ .

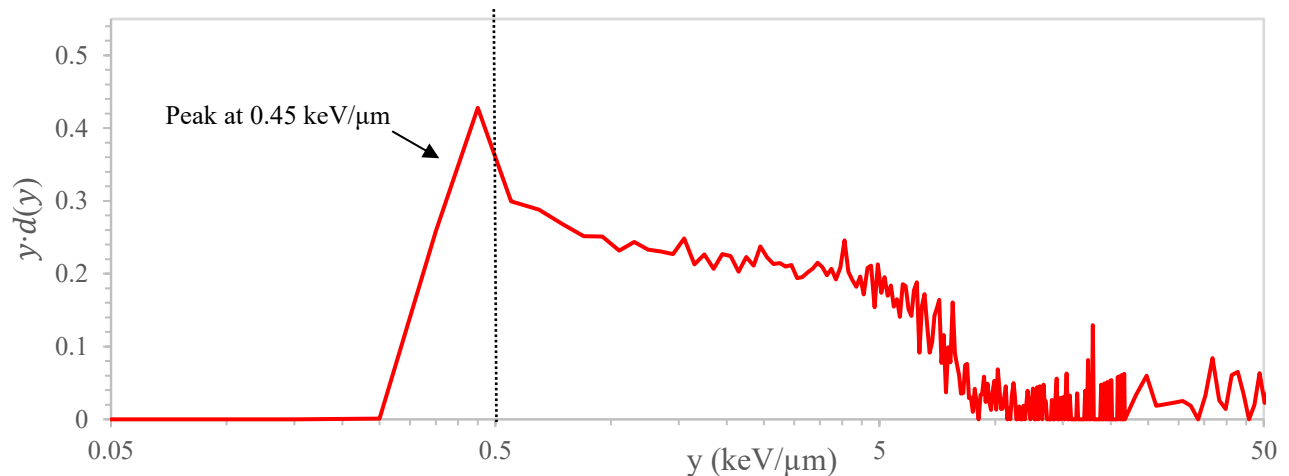


Figure 18. A typical dose distribution low LET spectrum produced from HAWK TEPC using the experimental measurements for background radiation done at the Ottawa FPS station (RPB) on 22-June-2021.

The significance and the detailed steps of method to restore the doses below threshold will be discussed in the following sections. A few different interpolation methods were published for dose correction below the electronic threshold, among which the most common way is to employ simulated  $^{60}\text{Co}$  or  $^{137}\text{Cs}$  spectra (Bianchi & Mazzucconi, 2021).

Section 3.3.2 details the methods used to evaluate and extrapolate the missing dose below  $0.5 \text{ keV}/\mu\text{m}$  in HAWKs, including the method used by RMC and two improved methods that we proposed in the project (named MD-1 & MD-2). Both RMC and MD-1 depend on the simulation of gamma spectra. MD-2 was developed based on the experimental measurements, then tested by using the simulated gamma and muon spectra. Section 3.3.3 represent all the results, including 4 sub-sections, section 3.3.3.1 shows the comparison in the dose distribution spectra between FLUKA simulation and experimental measurements; section 3.3.3.2, 3.3.3.3, & 3.3.3.4 present the dose distribution spectra and the dose equivalent results by using the RMC, MD-1 & MD-2 methods respectively.

### *3.3.2 Comparison Between Experimental Measurements & FLUKA Simulations*

#### **3.3.2.1 Design & Method**

##### I. FLUKA Monte-Carlo Simulations

The setup was modeled using FLUKA, the Monte Carlo code, which can mimic how the particles transport and interact with matter (Gersey & Wilkins, 2012). The simulation can estimate the ionization energy deposited through particle scattering, interactions, and propagation in the matter.

A FLUKA application was developed to simulate the response of a 4.95 inch Rossi-type TEPC with exposure to monoenergetic beams. Five simulated spectra are used to compare with the field measurements, including the spectra of 200 keV photon, 662 keV photon, 10000 keV photon, 1 GeV Muon and 4 GeV Muon. The choice of the initial kinetic energy and the type of particles was made to represent the dynamic radiation environment, i.e., typically, cosmic muon has mean kinetic energy at 4 GeV, and gamma rays has an energy of 662 keV (Wijesinghe, 2007).

## II. Experimental Measurements

The gamma spectrum (EXP. (Cs-137)) was obtained by exposing HAWK to a point source,  $^{137}\text{Cs}$  for 25 hours (Figure 19). The activity of  $^{137}\text{Cs}$  was  $0.25 \mu\text{Ci}$  on 01-Jan-15 (the reference date). The Caesium-137 ( $^{137}\text{Cs}$ ) is a double encapsulated gamma source (Figure 19 A). The sources were placed directly on the HAWK and perpendicular to the centre of the TEPC volume (Figure 19 B). The HAWK is secured on the wood stand 1 m above the ground.

The background spectrum was also obtained by operating HAWK for 25 hours under the same conditions after removing the radioactive source. In both cases, the last 24 hours of data were used for analysis to avoid stabilization issues. The “pure” gamma dose distributions were calculated by using the gamma spectrum counts minus the background readings.

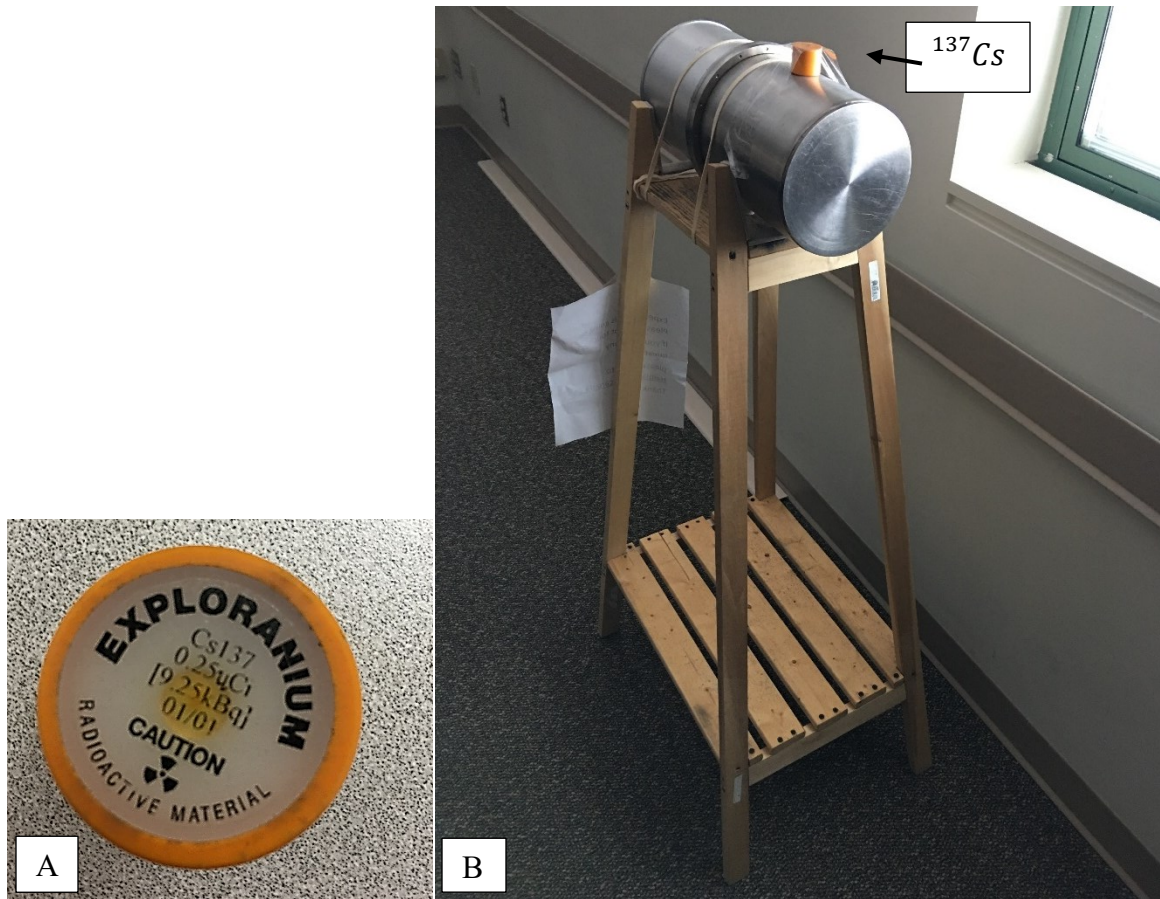


Figure 19. The set up of HAWK exposed to  $^{137}\text{Cs}$ .

In addition, the field measurements (EXP. (Natural Background)) contributed from the natural background radiation were done to generate a natural radiation background spectrum. The HAWK 2 was installed on the 1 meter high wooden stand in a flat and open space, away from the trees and obstructions. The set-up of the experiment is shown below (Figure 20).

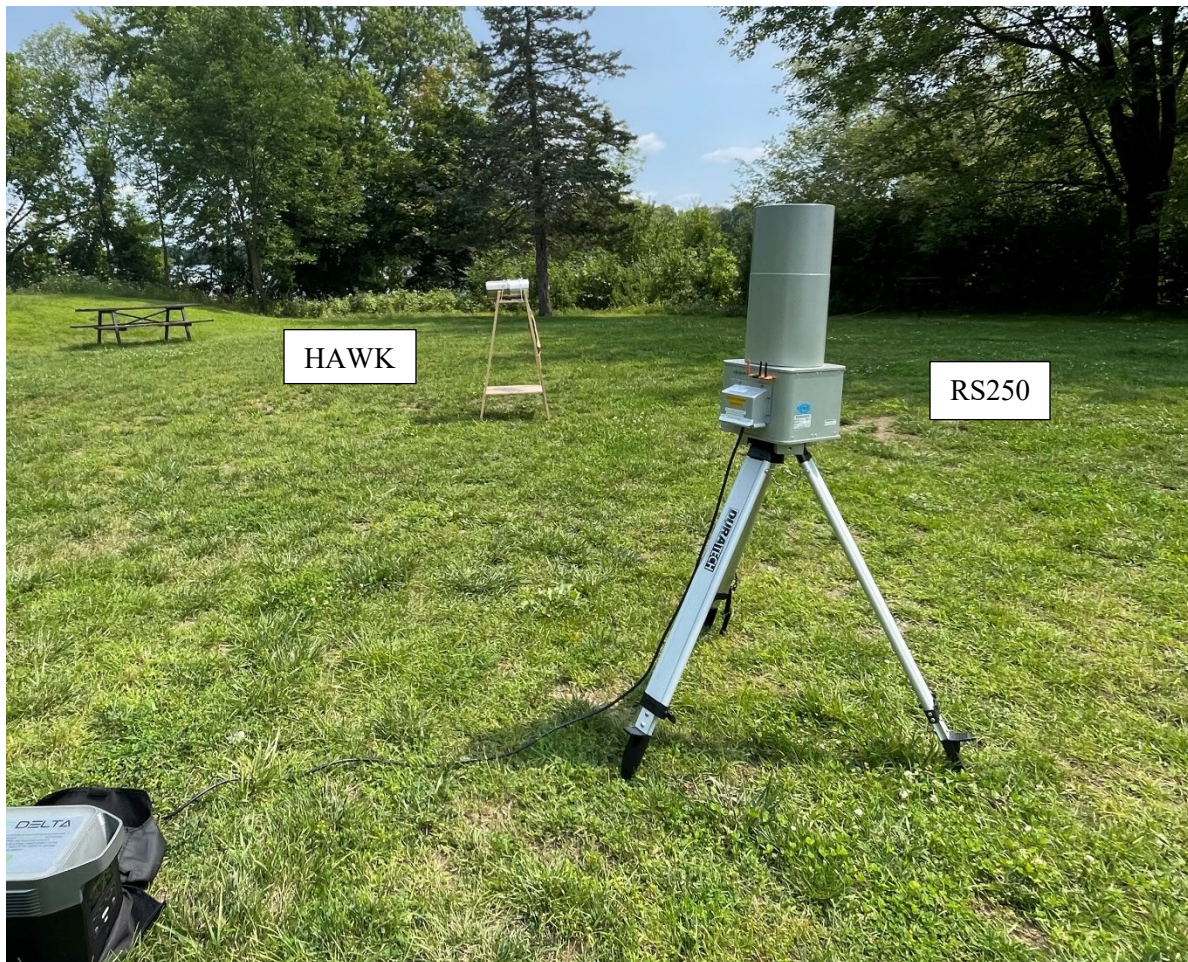


Figure 20. Set-up of the field experiment performed in Ottawa local park near Rideau Canal Lock 35-Narrows on 03-Aug-2021.

### III. Data analysis

The results from HAWK experimental measurements and FLUKA simulation were compared in two ways: comparing the dose distribution  $y \cdot d(y)$  spectra (Equation 18 & 19 in Section 2.2) and the dose equivalents ( $H$ ) (Equation 22 in Section 2.2) calculated from the low LET spectrum (0-10  $keV/\mu m$ ). The simulation plots are approximated by using a polynomial equation of degree six.

Because some energy deposition events detected below threshold (0.5  $keV/\mu m$ ) are “false”, i.e., contaminated with noise, two experimental dose equivalents were calculated by using 1. the “raw” experimental measurements without any cuts (i.e., from 0-10  $keV/\mu m$ ), and 2. the experimental measurements with a cut at threshold (i.e., from 0.50-10  $keV/\mu m$ ).

In addition, a new method to evaluate the response of TEPC in different radiation environments (FLUKA simulated spectra of 200 keV photon, 662 keV photon, 10000 keV photon, 1 GeV Muon and 4 GeV Muon), i.e., the counts versus lineal energy. To make the dependence on  $y$  clearer, the natural log values of the counts ( $\ln(n(y))$ ) were plotted against the natural log values of the lineal energy ( $\ln(y)$ )<sup>22</sup>. This new method explored the power relation between counts  $n(y)$  and lineal energy ( $y$ ).

---

<sup>22</sup> The natural logs (i.e., logarithms base  $e$ ) and the log (i.e., logarithms base 10) are interchangeable with each other in the method.

**3.3.2.2 Results and Discussion**

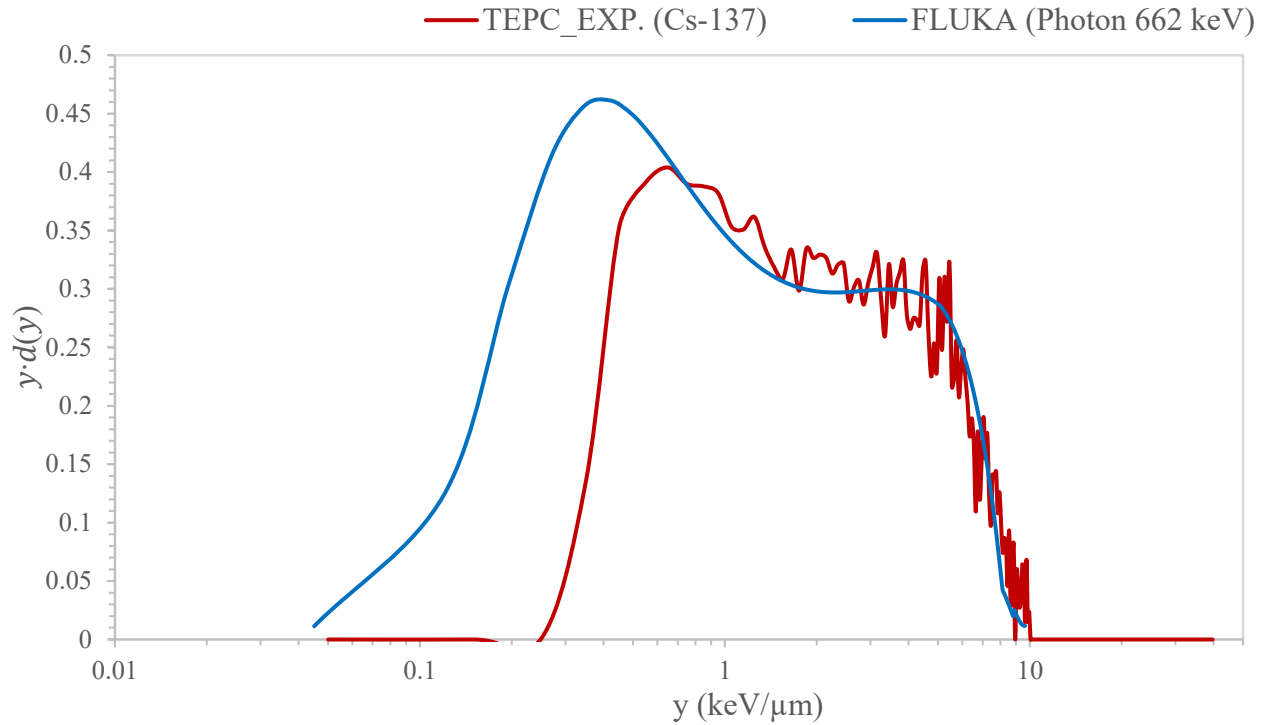


Figure 21. Comparison between the gamma dose distribution spectra (0-5 keV/μm) using the measurements with radioactive <sup>137</sup>Cs gamma source and the FLUKA simulation of 662 keV photon.

Table 5. The summary of the dose equivalent rates (H) calculated from gamma rays’ (<sup>137</sup>Cs) spectra by using the experimental measurements (TEPC\_EXP.) and FLUKA simulation; the percentage differences between the underestimated dose (raw experimental measurements) and the simulated dose result.

<sup>137</sup> Cs spectrum	H (nSv/h)	% difference
TEPC_EXP.	65.95 ± 0.27	-
TEPC_EXP. with threshold cut	58.21 ± 0.27	-11.7
FLUKA (Photon 662 keV)	106.40 ± 0.30	61.3

The experimental measurement by using a gamma source, TEPC\_EXP. (Cs-137) is compared to the FLUKA simulated results (FLUKA (662 keV photon) (Figure 21 & Table 5). From 0.65  $keV/\mu m$  to 10  $keV/\mu m$ , the shape of the simulated dose distributions matches the experimental measurements. Much fewer counts are detected in HAWK below 0.55  $keV/\mu m$  than in simulation. Instead of a straight cut shown in the HAWK measurements, the simulated spectrum indicates the presence of events below the electronic threshold, i.e., below 0.50  $keV/\mu m$ . In table 5, the dose equivalents calculated from experimental measurements without the threshold cut (i.e., raw measurements from 0-10  $keV/\mu m$ ), the experimental measurements with a cut at threshold (i.e., from 0.50-10  $keV/\mu m$ ) and the FLUKA simulated results are  $(65.95 \pm 0.27) nSv/h$ ,  $(58.21 \pm 0.27) nSv/h$  and  $(106.40 \pm 0.30) nSv/h$  respectively. The percentage difference between the doses calculated from the raw experimental measurements and simulated results is 61.3 % (table 5), i.e., the dose calculated from the raw TEPC measurements underestimated the actual dose, and it is important to include the dose below the threshold.

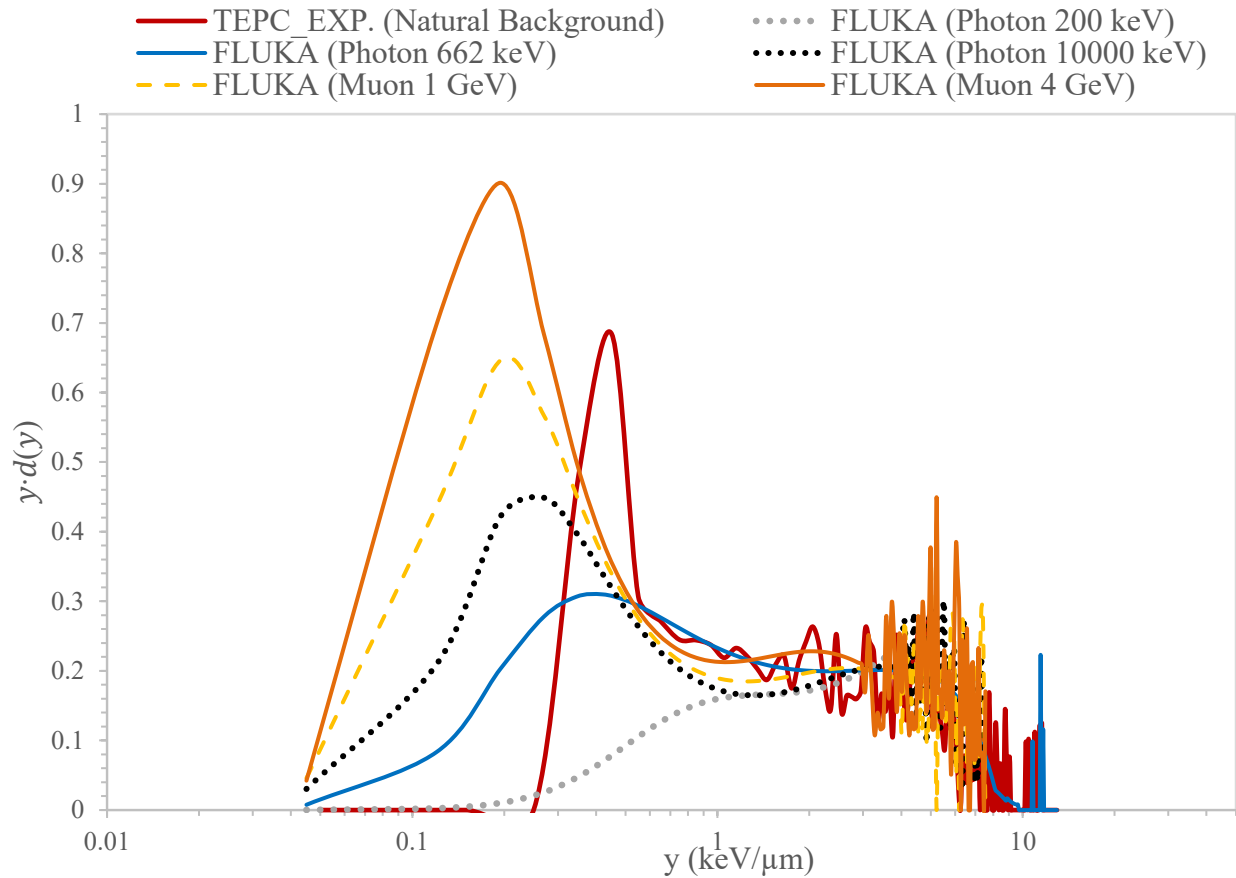


Figure 22. Comparisons between the dose distribution spectra by using the field measurements and the FLUKA simulation with different monoenergetic beams.

Figure 22 shows the normalized dose distributions among the spectra contributed from the natural background radiation and the FLUKA simulation with monoenergetic beams. It indicates that the peaks in the low LET spectra of 200 keV photon, 662 keV photon, and 10000 keV photon were located at  $1.01 \text{ keV}/\mu\text{m}$ ,  $0.42 \text{ keV}/\mu\text{m}$  and  $0.25 \text{ keV}/\mu\text{m}$  respectively. Compared to the peaks contributed from gamma rays, the peaks contributed from the 1 GeV muon, and 4 GeV muon were sharper, which were found at  $0.22 \text{ keV}/\mu\text{m}$  and  $0.20 \text{ keV}/\mu\text{m}$  respectively.

A new way to interpret the counts' distribution spectra resulting in different radiation environments is shown in Figure 23. Unlike the previous figures, figure 23 plots the natural log value of counts ( $\ln(n(y))$ ) versus the natural log value of lineal energy ( $\ln(y)$ ) to show characteristics that were unnoticeable in a linear-linear count distribution plot. The dependence of  $n(y)$  on  $y$  can be approximated by a simple power function, which is presented as a near-linear line (above thresholds, i.e.,  $\ln(0.55) \cong -0.60$ ) in the natural log-log plot (Figure 23). The values of  $\ln(n(y))$  decrease almost linearly along the  $\ln(y)$  from 0.55-1.05  $keV/\mu m$  (the grey area in the figure). It reveals the potential to extrapolate, or “restore”, the data below threshold by using the linear relation between  $\ln(n(y))$  and  $\ln(y)$  from 0.55  $keV/\mu m$  (the first channel after the threshold) to 1.05  $keV/\mu m$  (6 channels in total). The details will be discussed in section 3.3.4.

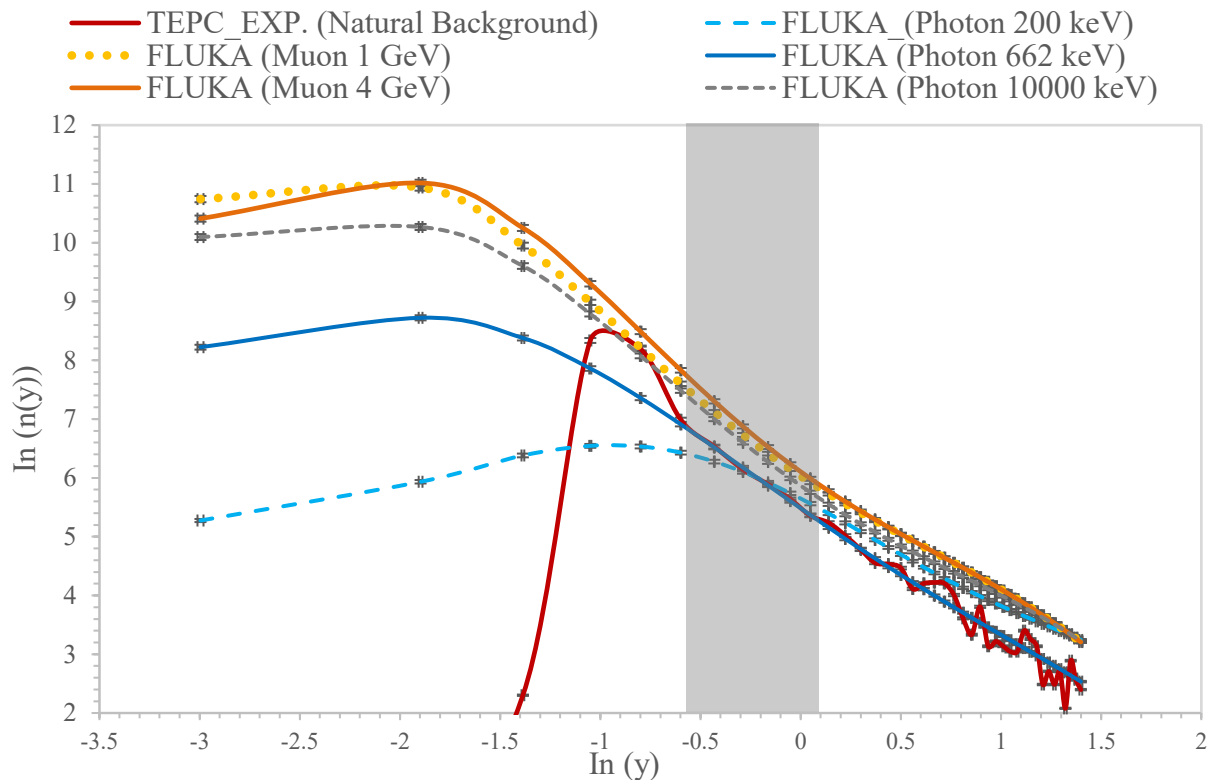


Figure 23. Comparison of experimental and simulated logarithmic spectra of counts. The grey area shows the linear relation between  $\ln(n(y))$  and  $\ln(y)$  from 0.55  $keV/\mu m$  to 1.05  $keV/\mu m$ .

### 3.3.3 RMC Method

The extrapolation method from RMC was evaluated first in the project. The technique has been employed widely in the cosmic radiation dose measurement with TEPC in space and at flight altitude (Bianchi & Mazzucconi, 2021). The RMC method is generated from the Pacific Northwest National Laboratory (PNNL) software (Lewis, 1999).

#### 3.3.3.1 Method

From the experimental measurements, the product of the lineal energy ( $y$ ) multiplied by the counts  $n(y)$  from the 5th Channel, i.e.,  $y_5 n(y_5)$  in  $0.55 \text{ keV}/\mu\text{m}$ , is used to approximate the actual  $y \cdot n(y)$  values in channels 0 to 4. Then the counts of the first 4 channel can be calculated from:

$$n(y_{i=1 \text{ to } 4}) = \frac{y_5 n(y_5)}{y_{(i=1 \text{ to } 4)}} \quad \text{Equation 36}$$

**3.3.3.2 Results & Discussion**

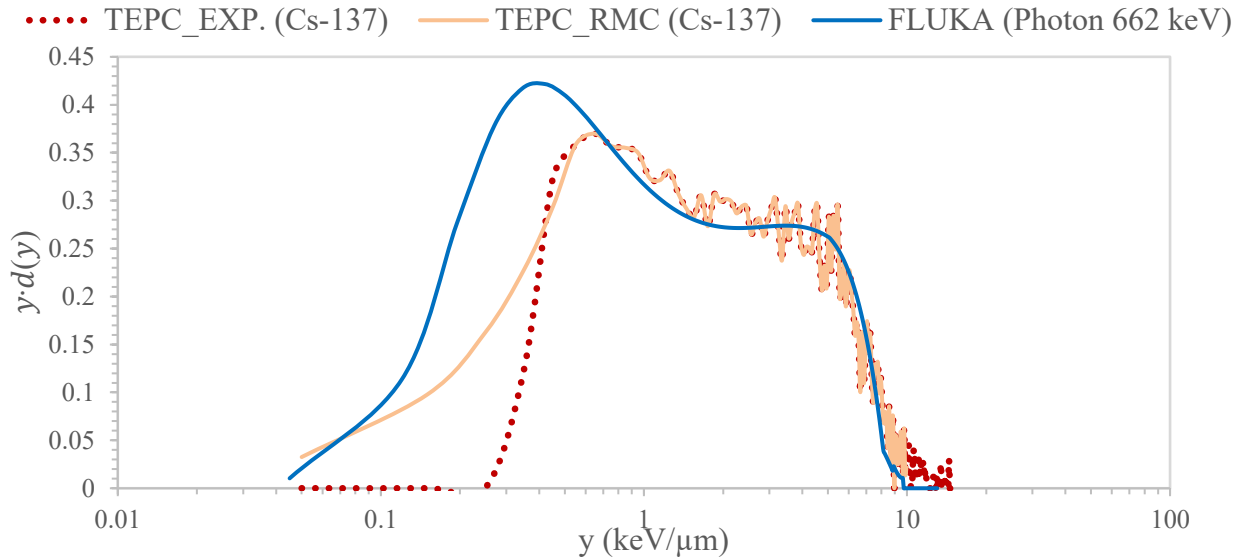


Figure 24. Comparisons between the gamma dose distribution spectra using the experimental measurements with  $^{137}\text{Cs}$ , the results after applying the RMC extrapolation method, and the FLUKA simulation with 662 keV photon after normalization.

Table 6. The summary of the dose equivalent rates (H) calculated from gamma rays' ( $^{137}\text{Cs}$ ) spectra by using the experimental measurements (TEPC\_EXP.) and the RMC method; the percentage differences between the underestimated dose (raw experimental measurements) and the result after extrapolation below the low LET threshold.

$^{137}\text{Cs}$ spectrum <sup>23</sup>	H (nSv/h)	Percentage difference <sup>24</sup>
TEPC_EXP.	$65.95 \pm 0.27$	-
TEPC_EXP. with threshold cut	$58.21 \pm 0.27$	-11.7 %
TEPC_RMC	$81.68 \pm 0.28$	23.9 %

<sup>23</sup> Low LET spectrum refers to the lineal energy ranging from 0 keV/μm to 10 keV/μm, where 10 keV/μm is recognized as the separation point between low LET and high LET.

<sup>24</sup> The percentage difference is calculated by using the difference in dose equivalents between the result after applying the extrapolation correction method of RMC and the experimental measurements divided by the experimental measurement.

The experimental measurement by using a gamma source, TEPC\_EXP. (Cs-137), is compared to the measurement corrected by the RMC extrapolation and FLUKA simulated results (FLUKA (662 keV photon)) (Figure 24 & Table 6). As shown, compared to the simulation, fewer events are detected in HAWK below  $0.55 \text{ keV}/\mu\text{m}$ , i.e., events are partially restored after the RMC extrapolation. In table 6, the dose equivalents calculated from raw measurements, the experimental measurements with a cut at the threshold and extrapolated data by using the RMC method are  $(65.95 \pm 0.27) \text{ nSv/h}$ ,  $(58.21 \pm 0.27) \text{ nSv/h}$  and  $(81.68 \pm 0.28) \text{ nSv/h}$  respectively. The percentage difference between the doses calculated from the underestimated experimental measurements and the data after RMC extrapolation is 23.9 %, much smaller than the simulated result (61.3%, Table 6).

Table 7. The summary of the dose equivalent rates (H) calculated from natural background radiation's spectra by using the experimental measurements (TEPC\_EXP.) and the RMC method; the percentage differences between the underestimated dose (raw experimental measurements) and the results after extrapolations below the low LET threshold.

Natural Background spectrum	H ( $\text{nSv/h}$ )	Percentage difference
TEPC_EXP.	$45.17 \pm 0.60$	-
TEPC_EXP. with threshold cut	$29.74 \pm 0.60$	-34.2%
TEPC_RMC	$44.63 \pm 0.59$	-1.3 %

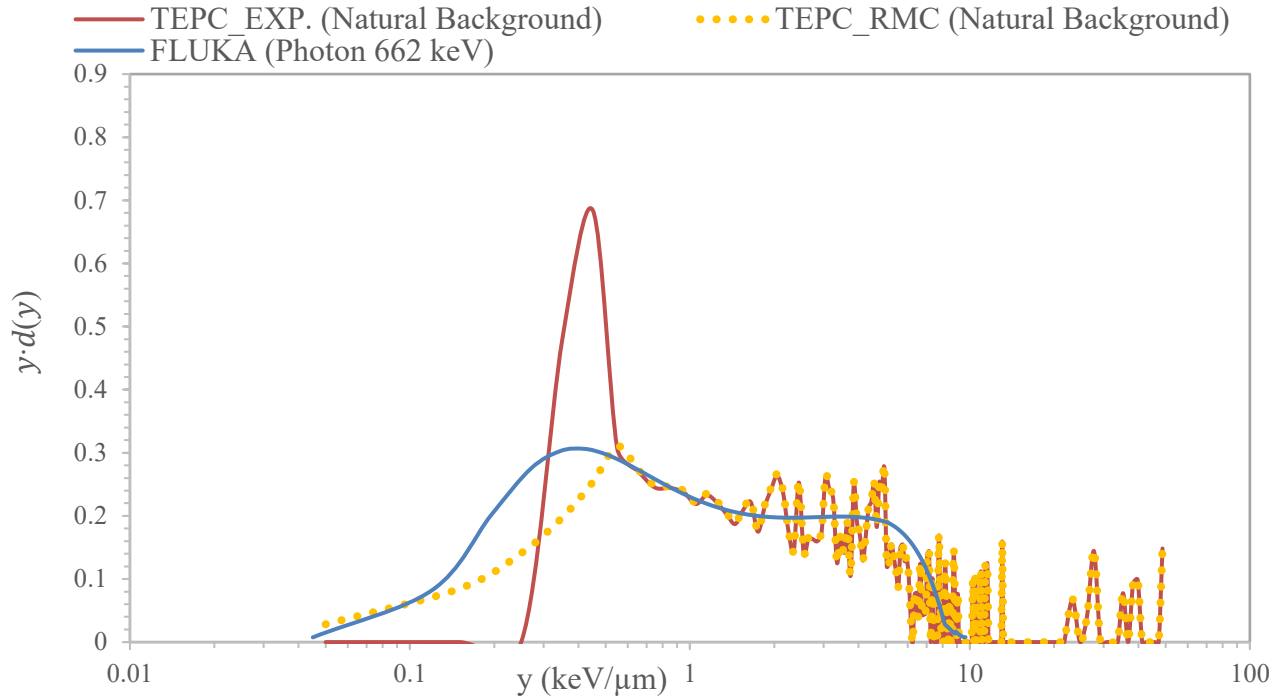


Figure 25. Comparisons between the dose distribution spectra using the field measurements with natural background radiation, the results after applying the RMC extrapolation method, and the FLUKA simulation with 662 keV photon after normalization.

The experimental measurement in a natural background, TEPC\_EXP. (Natural Background), is compared to the measurement corrected by the RMC extrapolation and FLUKA simulated results (FLUKA (Photon 662 keV)) (Figure 25 & Table 7). As shown in figure 25, there is a high peak observed at  $0.35 \text{ keV}/\mu\text{m}$  in the EXP. (Natural Background), which may be resulted from a high noise level in the last channel before the threshold ( $0.50 \text{ keV}/\mu\text{m}$ ). Not many events are corrected after the RMC extrapolation below  $0.55 \text{ keV}/\mu\text{m}$ . In table 7, the dose equivalents calculated from the raw measurements, the experimental measurements with a cut at the threshold and the data after extrapolation by RMC are  $(45.17 \pm 0.60) \text{ nSv/h}$ ,  $(29.74 \pm 0.60)$

$nSv/h$  and  $(44.63 \pm 0.59) nSv/h$  respectively. The dose calculated from the raw experimental measurements is 34.2 % more than the one with threshold cut, which means that the energy deposition events below the threshold contributed to 34.2 % in the total gamma doses and should not be removed in the dose calculation. The dose calculated from the raw experimental measurements is 1.3 % more than the doses calculated by using the RMC extrapolation (Table 7). Also, in Figure 25, some doses are corrected by RMC in the region between  $0 keV/\mu m$  and  $0.25 keV/\mu m$ , but the doses contributed from  $0.30 keV/\mu m$  to  $0.50 keV/\mu m$  may be mistakenly treated as noise, which results in underestimated results.

In conclusion, the RMC extrapolation method cancels the electronic noise and restores some energy events that were not measured below the threshold. The RMC method performs not as well in measuring the doses from natural background/ cosmic rays at ground level as in radiation environments with strong sources or cosmic rays at higher altitudes. In space station or at flight altitude, the RMC method was widely employed. The space or flight-altitude cosmic radiation doses are ~ 10 times to 400 times more than the doses detected at ground level, because neutrons appear in cosmic rays in much greater abundance at higher altitudes. RMC method works in the cases that the doses contributed from non-neutron particles are less significant. This project focuses the doses contributed from non-neutron cosmic rays at ground level, i.e., low dose exposures in the environment. The estimation below low LET threshold by using the RMC method is not good enough. It is crucial to develop our extrapolation methods to serve the purpose of the thesis better.

### 3.3.4 Improved Methods (MD-1 & MD-2)

#### 3.3.4.1 Theory

As mentioned in section 3.3.2, there is a relation between the peaks in the low LET dose distribution spectrum and the type of the radiation. Figure 22 shows that the peak may shift towards left if the energy of the incoming photon is larger, i.e., 200 keV photon, 662 keV photon, and 10000 keV photon peak at  $1.01 \text{ keV}/\mu\text{m}$ ,  $0.42 \text{ keV}/\mu\text{m}$  and  $0.25 \text{ keV}/\mu\text{m}$  respectively. For 1 GeV muon and 4 GeV muon, they peak at  $0.22 \text{ keV}/\mu\text{m}$  and  $0.20 \text{ keV}/\mu\text{m}$  respectively. Also, compared to the peaks contributed from gamma rays, the peaks contributed from muons were sharper. In addition, it is found that the values of  $\ln(n(y))$  are almost linearly along the  $\ln(y)$  between  $0.55 \text{ keV}/\mu\text{m}$  and  $1.05 \text{ keV}/\mu\text{m}$  (Figure 23), and the slopes of these “linear” regions change in different radiation environments, i.e., it may be capable of reflecting the changes in a mixed radiation field.

Two improved methods are developed for the project. MD-1 employs the FLUKA simulated  $^{137}\text{Cs}$  spectrum (monoenergetic photon with kinetic energy of 662 keV). In comparison, MD-2 uses the measured dose distribution spectra and is expected to work better in the dynamic radiation environment. The results from HAWK experimental measurements and FLUKA simulation were compared in multiple ways: by using the dose distribution  $y \cdot d(y)$  spectra, the logarithmic spectra of counts and the dose equivalents ( $H$ ) calculated from the low LET spectrum ( $0\text{-}10 \text{ keV}/\mu\text{m}$ ).

### 3.3.4.2 Method

#### I.MD-1:

FLUKA simulation outputs counts from  $0.045 \text{ keV}/\mu\text{m}$  to  $76.763 \text{ keV}/\mu\text{m}$  with bin width of  $0.075 \text{ keV}/\mu\text{m}$ . In the low LET region ( $0.045 \text{ keV}/\mu\text{m}$  to  $1.320 \text{ keV}/\mu\text{m}$ ), a sextic polynomial with  $R^2 = 0.97$  was generated to approximate the simulated dose distribution curve. Counts were calculated by using the polynomial with the HAWK's lineal energy bin width ( $0.1 \text{ keV}/\mu\text{m}$  in low LET). The distribution of counts was then normalized and fitted to the experimental measurements by using the linear relation between  $\ln(n(y))$  and  $\ln(y)$  from  $0.55 \text{ keV}/\mu\text{m}$  to  $1.05 \text{ keV}/\mu\text{m}$ . Counts  $n(y)$  were calculated from the fitted equation from  $0.05 \text{ keV}/\mu\text{m}$  to  $0.45 \text{ keV}/\mu\text{m}$  (first 5 channels).

#### II.MD-2:

As shown in figure 23 (section 3.3.2), the natural log values of the counts ( $\ln(n(y))$ ) were plotted against the natural log values of the lineal energy ( $\ln(y)$ ). The linear best fit equation was obtained from  $0.55 \text{ keV}/\mu\text{m}$  to  $1.05 \text{ keV}/\mu\text{m}$ , where is found to be the best fit equation in all measurements (with  $R^2$  ranging from 0.96 to 0.99). The equation was then employed to calculate the counts from  $0.05 \text{ keV}/\mu\text{m}$  to  $0.45 \text{ keV}/\mu\text{m}$  (i.e., extrapolation).

The counts were then tested in the simulated spectra of different monoenergetic particles, including 200 keV photon, 662 keV photon, 10000 keV photon, 1 GeV muon and 4 GeV mount. It was observed that the calculated counts in the first two channels (i.e.,  $0.05 \text{ keV}/\mu\text{m}$  &  $0.15 \text{ keV}/\mu\text{m}$ ) were much larger than the counts in the third ( $0.25 \text{ keV}/\mu\text{m}$ ). On the contrary, the

simulated counts in the first two channels were less than the third channel. Two equations based on empirical observations from the FLUKA simulated spectra were obtained to modify the counts in the first two channels:

$$n(y_1) = \frac{y_3 n(y_3) - y_2 n(y_2)}{y_1} \quad \text{Equation 37}$$

$$n(y_2) = \frac{y_3 n(y_3) + y_4 n(y_4)}{y_2} \quad \text{Equation 38}$$

Where  $y_{i=1,2,3,4}$  refers to the lineal energy in the channel (i),  $n(y_{i=1,2,3,4})$  is the count in the corresponding channel and  $y_i n(y_i)$  is the product of the lineal energy and count in channel i. The empirical equations 37 & 38 must be evaluated further.

### III. Mixed radiation field simulation

To evaluate the MD-1 and MD-2 in mixed radiation field, the counts of mixed field spectra are obtained by adding the counts of the simulated (monoenergetic) 4 GeV muons ( $\mu$ ) spectrum to the simulated 662 keV photons ( $\gamma$ ) spectrum in different ratios:  $\mu: \gamma = 1:20, 1:10, 1:8, 1:6, 1:4, 1:2, 1:1, 2:1, 4:1, 6:1, 8:1, 10:1, \text{ and } 20:1$ .

**3.3.4.3 Result & Discussion**

A. MD-1 & MD-2 in FLUKA simulated spectra

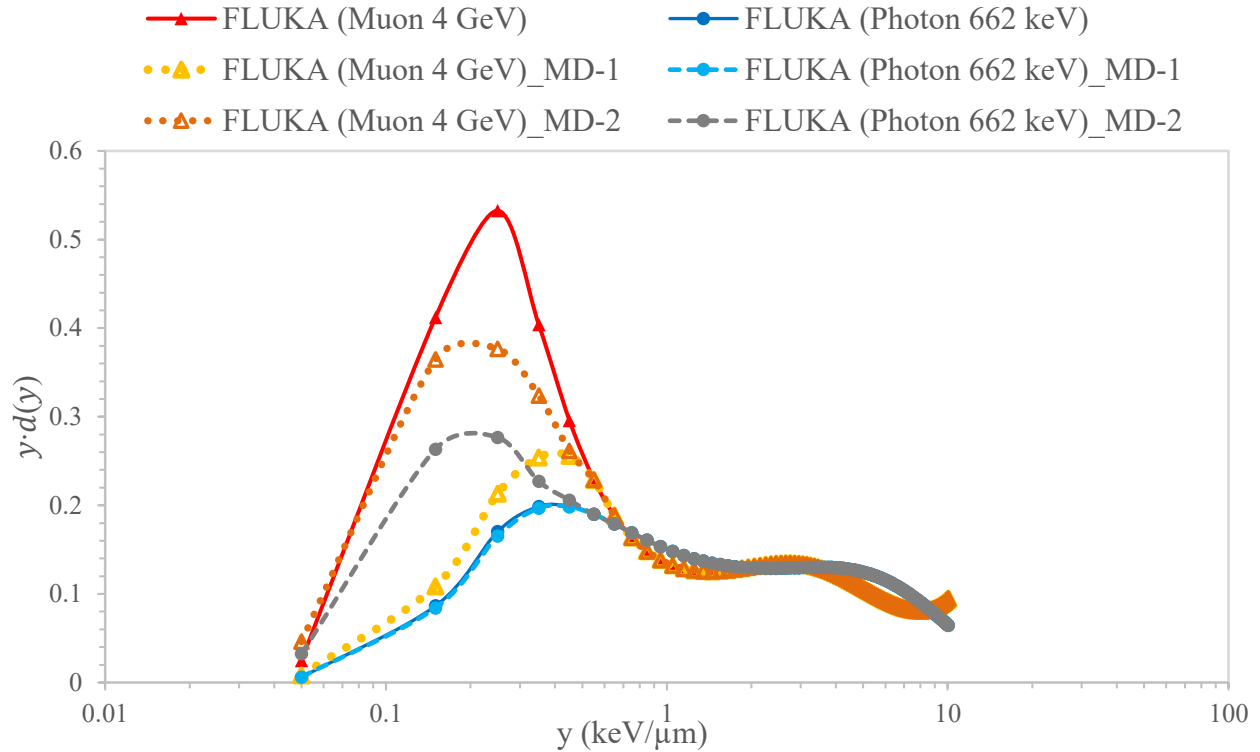


Figure 26. Comparison of normalized dose distribution spectra between simulations and after MD-1 & MD-2 extrapolations.

Figure 26 compares the simulated dose distribution spectra using monoenergetic particles and the results after applying the MD-1 and MD-2 extrapolations. Muon simulation (4 GeV) is significant because the average kinetic energy of muons received at ground level is approximately 4 GeV (Atri & Melott, 2013). Photon simulation (662 keV) also plays a vital role because the mean energy of gamma rays emitted from a  $^{137}\text{Cs}$  source is 662 keV (Guinn, 2003). Figure 26 shows that MD-1 (Photon 662 keV) was developed based on the photon 662 keV simulations, i.e., the dose distributions are the same. There is a big “bump” in MD-2 (Photon 662

keV) compared to the FLUKA (Photon 662 keV), i.e., MD-2 will result in overestimated dose results in gamma spectrum because MD-2 always take muon into consideration. Compared to muon simulations (Figure 26), FLUKA (Muon 4 GeV), which is represented by red line with triangles, MD-1 cannot “restore” as many energy-deposition events as MD-2 below the threshold in the muon spectrum.

Table 8. The summary of the dose equivalent rates (H) calculated from the FLUKA spectra using the simulated data and MD-1; the percentage differences between the raw FLUKA doses, and the results after extrapolations.

FLUKA monoenergetic simulated spectra	H (nSv/h)		% difference <sup>25</sup>
	FLUKA	MD-1	
$\mu$ 1 GeV	$906.6 \pm 8.9$	$552.4 \pm 8.7$	-39.1
$\mu$ 4 GeV	$858.9 \pm 8.4$	$535.9 \pm 8.1$	-37.6
$\gamma$ 200 keV	$596 \pm 12$	$652 \pm 12$	9.4
$\gamma$ 662 keV	$518.6 \pm 8.4$	$515.8 \pm 8.4$	-0.5
$\gamma$ 10000 keV	$747.7 \pm 8.8$	$558.3 \pm 8.6$	-25.3
Average			-22.4 <sup>26</sup>

Table 8 quantifies the differences in dose equivalent rates between the simulations and their spectra after MD-1 extrapolating from  $0.45 \text{ keV}/\mu\text{m}$  down to  $0.05 \text{ keV}/\mu\text{m}$ . As expected, MD-1 extrapolation performs very well in gamma spectra, i.e., the difference in the dose equivalent (rates) between the FLUKA Photon 662 keV and MD-1 is -0.5 %, and the difference is 9.4 % compared to the FLUKA Photon 200 keV. However, MD-1 does a poor job in the extrapolations

<sup>25</sup> The percentage difference is calculated by using the difference in dose equivalents between the result after applying the extrapolation correction method of MD-1 and the simulated dose divided by the simulated dose.

<sup>26</sup> The average percentage difference refers to the average of the absolute differences in the rows above.

for FLUKA 1 GeV muon (the difference is -39.1 %) and FLUKA 4 GeV muon (the difference is -37.6 %).

Table 9. The summary of the dose equivalent rates (H) calculated from the FLUKA spectra using the simulated data and the MD-2 method; the percentage differences between the raw FLUKA doses and the results after extrapolations.

FLUKA monoenergetic simulated spectra	H (nSv/h)		% difference <sup>27</sup>
	FLUKA	MD-2	
$\mu$ 1 GeV	906.6 $\pm$ 8.9	763.0 $\pm$ 8.8	-15.8
$\mu$ 4 GeV	858.9 $\pm$ 8.4	795.8 $\pm$ 8.3	-7.3
$\gamma$ 200 keV	596 $\pm$ 12	746 $\pm$ 12	25.2
$\gamma$ 662 keV	518.6 $\pm$ 8.4	701.0 $\pm$ 8.5	35.2
$\gamma$ 10000 keV	747.7 $\pm$ 8.8	785.9 $\pm$ 8.8	5.1
Average			17.7 <sup>28</sup>

Table 9 compares the differences in dose equivalent rates between the simulations and their spectra after MD-2 extrapolating from 0.45 keV/ $\mu$ m down to 0.05 keV/ $\mu$ m. MD-2 does not perform well in the extrapolation of FLUKA gamma spectra: for photon 200 keV, and 662 keV, the differences between FLUKA and MD-2 are 25.2 % and 35.2 % respectively (Table 9). MD-2 successfully restores most of the missing doses below threshold in the spectra of high energy photon (5.1 % difference), 4 GeV muon (-7.3 % difference) and 1 GeV muon (-15.8 %).

Generally, although MD-2 doesn't behave well in gamma spectra, the average percentage difference in dose equivalents between the simulations and MD-2 is 17.7 %, which is less than

<sup>27</sup> The percentage difference is calculated by using the difference in dose equivalents between the result after applying the extrapolation correction method of MD-2 and the simulated dose divided by the simulated dose.

<sup>28</sup> The average percentage difference refers to the average of the absolute differences in the rows above.

the difference between the simulations and MD1 (22.4 %), i.e., MD-2 still does a better job than MD-1.

### B. MD-1 & MD-2 in FLUKA simulated muon ( $\mu$ ) and gamma ( $\gamma$ ) mixed spectra

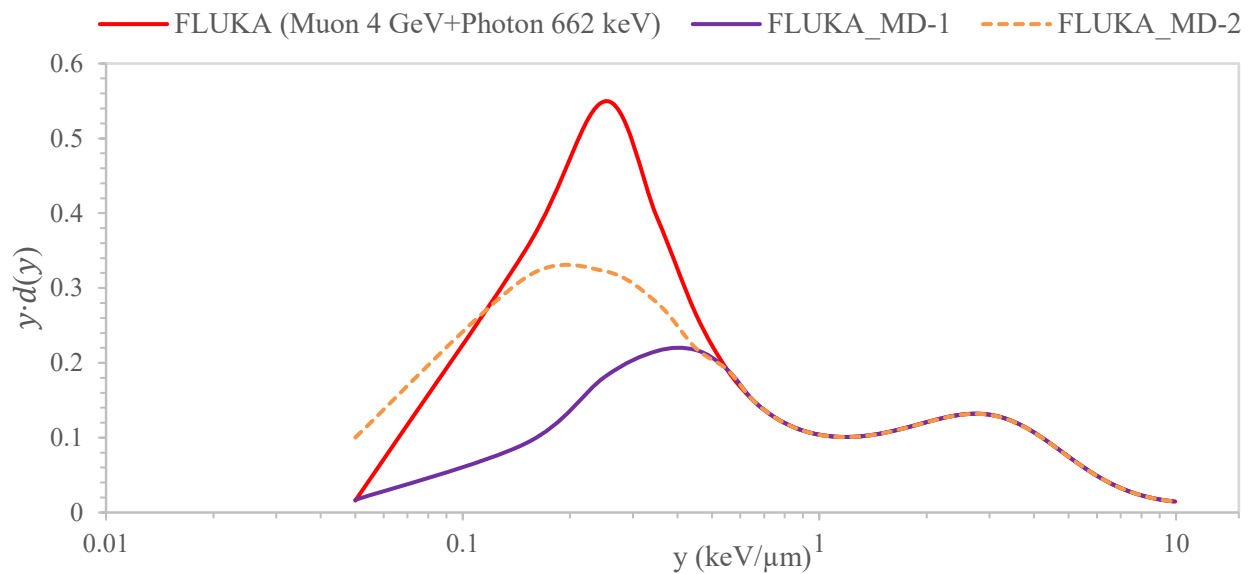


Figure 27. Comparison of normalized dose distribution spectra between mixed field simulation (Counts ratio of 4 GeV  $\mu$ : 662 keV  $\gamma$  = 4:1) and after MD-1 & MD-2 extrapolations.

Figure 27 shows an example of the dose distribution spectra obtained by using the mixed field simulation in a ratio<sup>29</sup>  $\mu$  (4 GeV):  $\gamma$  (662 keV) = 4:1. It compares a mixed radiation field's simulated dose distribution spectra, and the results after applying the MD-1 and MD-2 extrapolations. As shown, MD-1 (purple line) cannot “restore” as many energy-deposition events

<sup>29</sup> The counts of mixed field spectrum are obtained by adding the counts of the  $\mu$  spectrum to the  $\gamma$  spectrum in each lineal energy bins in a ratio:  $\mu$ :  $\gamma$  =4:1.

as MD-2 (orange dashed line) below the threshold compared to the simulated spectrum (red line).

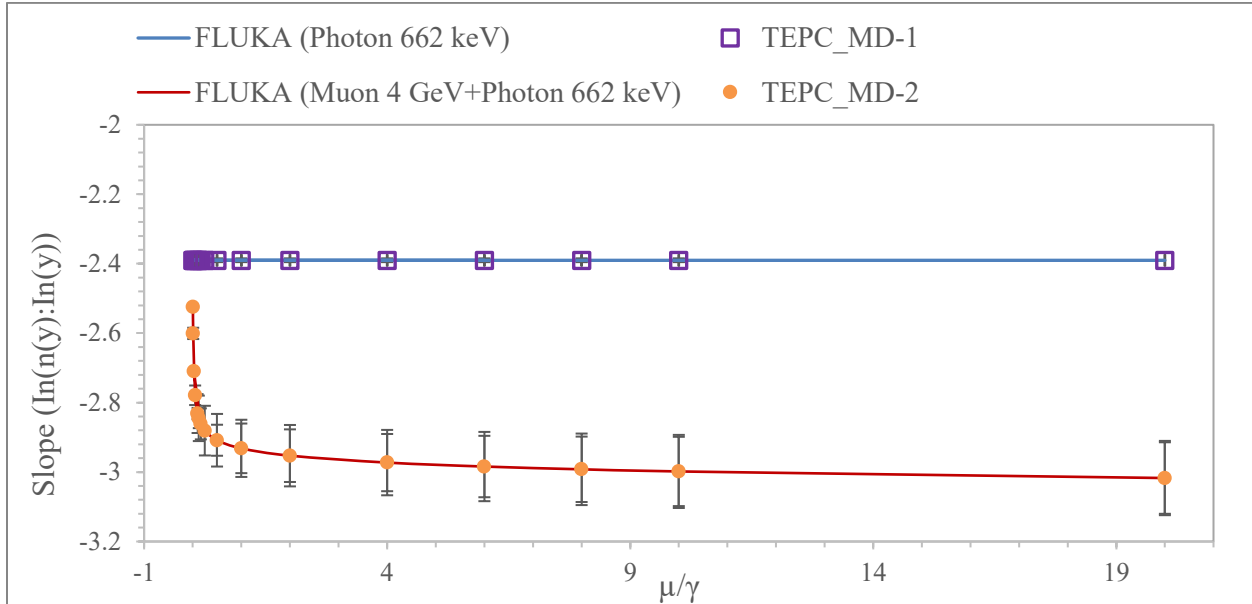


Figure 28. The comparison between the slopes of the linear best fit equations from  $\ln(n(y))$  vs.  $\ln(y)$  spectra of simulated mixed fields by using MD-1 and MD-2 extrapolation methods. Error bars represent the uncertainties on the slopes of  $\ln(n(y))$  versus  $\ln(y)$  plots (y-axis).

Figure 28 is obtained by comparing the slopes of the linear best fit equations from  $0.55 \text{ keV}/\mu\text{m}$  and  $1.05 \text{ keV}/\mu\text{m}$ , in order to visualize and evaluate how well the extrapolation methods of MD-1 and MD-2 perform in mixed radiation fields (i.e., different  $\mu/\gamma$  counts ratio). The slope used in the MD-1 is constant in all cases, which is equivalent to the slope generated from the simulated photon (662 keV) spectrum. MD-2 used the slopes of the simulated  $\ln(n(y))$  vs.  $\ln(y)$  spectra, it changes when the ratio of  $\mu/\gamma$  changes. When  $\mu/\gamma$  gets bigger, the absolute values of the slopes used in the MD-2 get bigger, i.e., the counts  $n(y)$  decrease faster as the lineal energy ( $y$ ) increases; and the slopes are not changing much when  $\mu/\gamma \geq 2$ .

Table 10 quantifies the differences in dose equivalent rates among different mixed field simulations and the dose equivalent results after MD-1 extrapolating from  $0.45 \text{ keV}/\mu\text{m}$  down to  $0.05 \text{ keV}/\mu\text{m}$ . And the differences in the dose equivalent rates (H) between the FLUKA mixed field spectra and MD-1 range from -31.5 % to -43.1 %. On average, the dose equivalent (rates) calculated by using MD-1 method is 39.0 % less than the simulated result.

Table 10. The summary of the dose equivalent rates (H) calculated from the FLUKA spectra using the simulated data and MD-1; the percentage differences between the raw FLUKA doses, and the results after extrapolations.

FLUKA mixed field spectra $\mu: \gamma$	H (nSv/h)		% difference <sup>30</sup>
	FLUKA	MD-1	
1:20	$55.78 \pm 0.49$	$38.23 \pm 0.48$	-31.5
1:10	$51.22 \pm 0.46$	$33.38 \pm 0.44$	-34.8
1:8	$50.32 \pm 0.45$	$32.37 \pm 0.43$	-35.7
1:6	$49.42 \pm 0.44$	$31.34 \pm 0.42$	-36.6
1:4	$48.54 \pm 0.43$	$30.28 \pm 0.41$	-37.6
1:2	$47.72 \pm 0.41$	$29.12 \pm 0.40$	-39.0
1:1	$47.38 \pm 0.41$	$28.44 \pm 0.39$	-40.0
2:1	$94.64 \pm 0.57$	$56.03 \pm 0.54$	-40.8
4:1	$189.68 \pm 0.79$	$110.92 \pm 0.75$	-41.5
6:1	$285.18 \pm 0.96$	$165.64 \pm 0.91$	-41.9
8:1	$381.0 \pm 1.1$	$220.3 \pm 1.0$	-42.2
10:1	$477.2 \pm 1.2$	$274.8 \pm 1.2$	-42.4
20:1	$961.6 \pm 1.7$	$547.6 \pm 1.6$	-43.1
Average			-39.0

<sup>30</sup> The percentage difference is calculated by using the difference in dose equivalents between the result after applying the extrapolation correction method of MD-1 and the simulated dose divided by the simulated dose.

Table 11 quantifies the differences in dose equivalent rates among different mixed field simulations and the dose equivalent results after MD-2 extrapolating from  $0.45 \text{ keV}/\mu\text{m}$  down to  $0.05 \text{ keV}/\mu\text{m}$ . And the differences in the dose equivalent rates (H) between the FLUKA mixed field spectra and MD-2 range from -0.1 % to -13.1 %. On average, the dose equivalent (rates) calculated using the MD-2 method is 8.5 % less than the simulated result.

Table 11. The summary of the dose equivalent rates (H) calculated from the FLUKA spectra using the simulated data and the MD-2 method; the percentage differences between the raw FLUKA doses, and the results after extrapolations.

FLUKA mixed spectra $\mu: \gamma$	H (nSv/h)		% difference <sup>31</sup>
	FLUKA	MD-2	
1:20	$55.78 \pm 0.49$	$55.76 \pm 0.49$	-0.1 <sup>32</sup>
1:10	$51.22 \pm 0.46$	$49.26 \pm 0.45$	-3.8
1:8	$50.32 \pm 0.45$	$47.92 \pm 0.44$	-4.8
1:6	$49.42 \pm 0.44$	$46.56 \pm 0.43$	-5.8
1:4	$48.54 \pm 0.43$	$45.16 \pm 0.42$	-7.0
1:2	$47.72 \pm 0.41$	$43.67 \pm 0.41$	-8.5
1:1	$47.38 \pm 0.41$	$42.84 \pm 0.40$	-9.6
2:1	$94.64 \pm 0.57$	$84.69 \pm 0.55$	-10.5
4:1	$189.68 \pm 0.79$	$168.17 \pm 0.77$	-11.3
6:1	$285.18 \pm 0.96$	$251.53 \pm 0.94$	-11.8
8:1	$381.0 \pm 1.1$	$334.9 \pm 1.1$	-12.1
10:1	$477.2 \pm 1.2$	$418.2 \pm 1.2$	-12.4
20:1	$961.6 \pm 1.7$	$835.2 \pm 1.7$	-13.1
Average			-8.5

Generally, MD-2 does better than MD-1 in restoring the (missing) doses below threshold. The following two sub-sections present the performance of MD-1 & MD-2 in “real” radiation

<sup>31</sup> The percentage difference is calculated by using the difference in dose equivalents between the result after applying the extrapolation correction method of MD-2 and the simulated dose divided by the simulated dose.

<sup>32</sup> The percentage difference is equal to 0.036%.

environments (C. experimental measurements done with  $^{137}\text{Cs}$  source and D. in the natural background).

### C. MD-1 & MD-2 in gamma spectra

The experimental measurement by using a gamma source, TEPC\_EXP. (Cs-137), is compared to the measurement corrected by the MD-1 & MD-2 extrapolations and FLUKA simulated results (FLUKA (662 keV photon)) (Figure 29, 30 & Table 12).

Figure 29 compares the  $^{137}\text{Cs}$  experimental and the simulated dose distribution spectra for multiple monoenergetic particles. As proposed in Section 3.3.2 (Figure 23), the values of  $\ln(n(y))$  decrease linearly with  $\ln(y)$  from 0.55-1.05  $\text{keV}/\mu\text{m}$  and MD-2 extrapolates 3 channels (0.45  $\text{keV}/\mu\text{m}$ , 0.35  $\text{keV}/\mu\text{m}$ , & 0.25  $\text{keV}/\mu\text{m}$ ) down along the linear track. The first 2 channels (0.15  $\text{keV}/\mu\text{m}$  & 0.05  $\text{keV}/\mu\text{m}$ ) are calculated by using the two empirical equations (Equation 37 & 38). It reveals that the difference between MD-1 and MD-2 is mainly caused by the counts estimated for the first two channels.

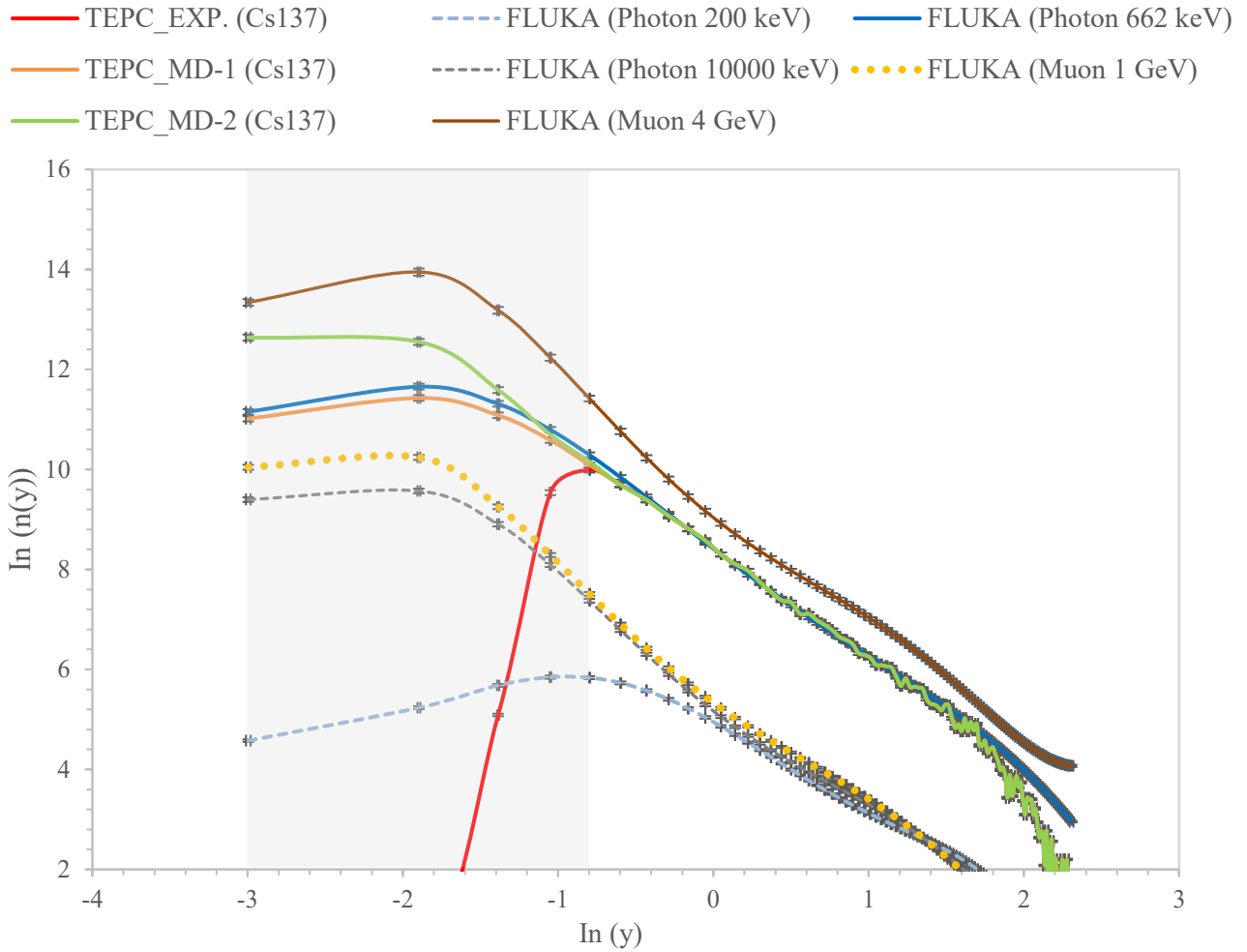


Figure 29. Comparison of Cs-137 experimental and simulated dose distribution spectra for multiple monoenergetic particles incident on the simulated TEPC from 1 meter.

Figure 30 below shows that some events are “restored” by using the MD-1 and MD-2 extrapolation methods below  $0.55 \text{ keV}/\mu\text{m}$  compared to the simulation. In table 12, the dose equivalents after MD-1 and MD-2 extrapolations are  $(88.59 \pm 0.28) \text{ nSv/h}$ , and  $(112.49 \pm 0.28) \text{ nSv/h}$  respectively. The percentage difference between the doses calculated from the raw experimental measurements and the data after MD-1 extrapolation is 34.3 %. The percentage difference between the doses calculated from the raw experimental measurements and the data

after MD-2 extrapolation is 70.6 %. Although the dose distributions after MD-2 correction is very different from the photon 662 keV simulation, the dose equivalent calculated from the spectrum of MD-2 ( $112.49 \pm 0.28 \text{ nSv/h}$ ) (Table 12) is close to (i.e., slightly higher than) the simulated results ( $106.40 \pm 0.30 \text{ nSv/h}$ ) (Table 5). In other words, it results in overestimated doses by using MD-2 extrapolation in gamma rays' spectra. MD-1 better estimates in the very low LET region than MD-2 in the gamma spectrum.

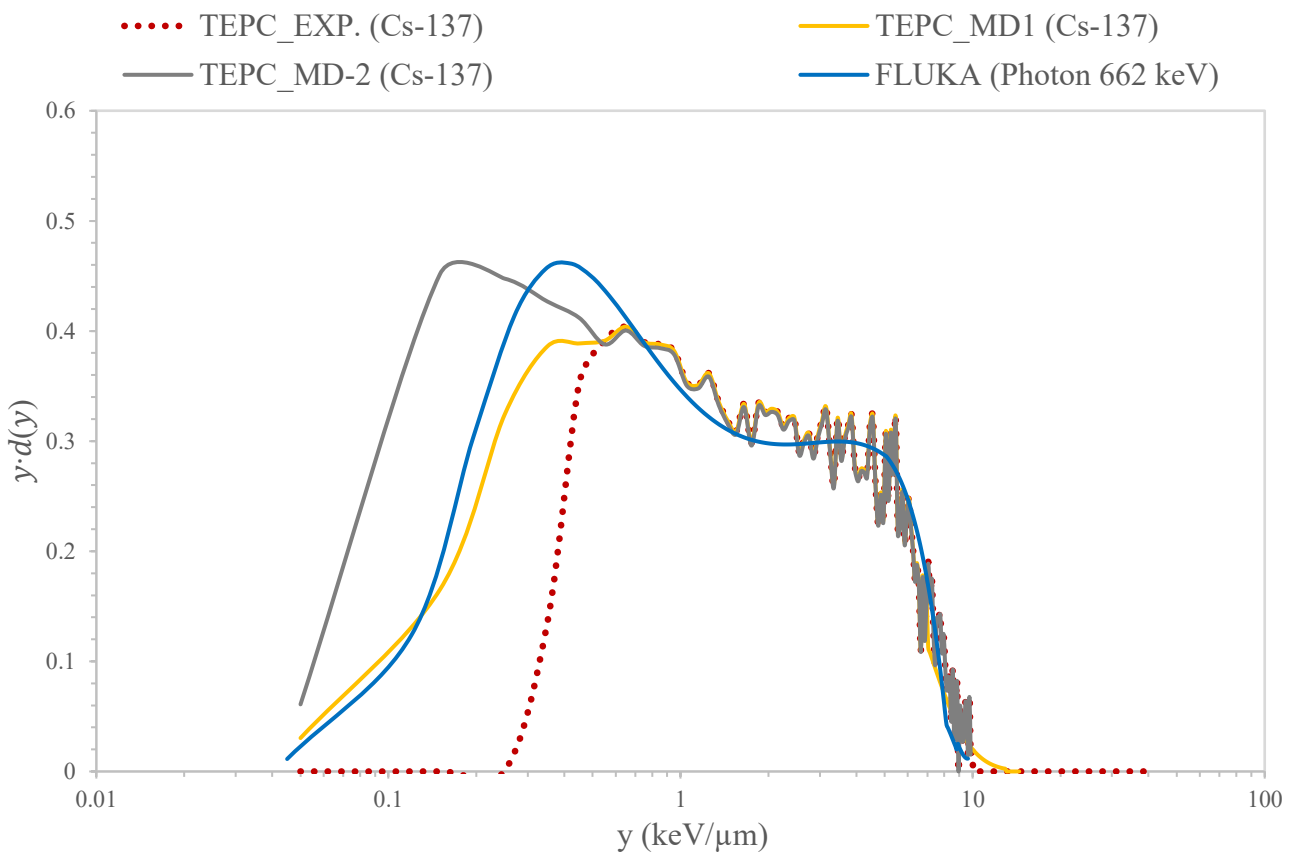


Figure 30. The gamma dose distribution spectra by using the experimental measurements (Cs-137), the results after applying the MD-1 & MD-2 extrapolation methods, and the FLUKA simulation with 662 keV photon.

Table 12. The summary of the dose equivalent rates (H) calculated from the gamma rays' ( $^{137}\text{Cs}$ ) spectra by using the experimental measurements (TEPC\_EXP.), MD-1 and MD-2 methods; the percentage differences between the underestimated dose (raw experimental measurements) and the results after extrapolations below the low LET threshold.

$^{137}\text{Cs}$ low LET spectrum <sup>33</sup>	H (nSv/h)	% Difference <sup>34</sup>
TEPC_EXP.	$65.95 \pm 0.27$	-
TEPC_EXP. with threshold cut	$58.21 \pm 0.27$	-11.7
TEPC_MD-1	$88.59 \pm 0.28$	34.3
TEPC_MD-2	$112.49 \pm 0.28$	70.6

<sup>33</sup> Low LET spectrum refers to the lineal energy ranging from 0 keV/ $\mu\text{m}$  to 10 keV/ $\mu\text{m}$ , where 10 keV/ $\mu\text{m}$  is recognized as the separation point between low LET and high LET.

<sup>34</sup> The percentage difference is calculated by using the difference in dose equivalents between the result after applying the extrapolation correction method and the experimental measurements divided by the experimental measurement.

#### D. MD-1 & MD-2 in natural background radiation spectra

The experimental measurement done in the natural radiation environment is compared to the measurement corrected by the MD-1 & MD-2 extrapolations and FLUKA simulations (Figure 31-33 & Table 13). Similar trends are observed in figure 31, the difference between MD-1 and MD-2 are mainly caused by the difference in the counts estimated for the first two channels (MD-2). In table 13, after extrapolating from the threshold down to  $0.05 \text{ keV}/\mu\text{m}$ , the new dose equivalent calculated from the low LET spectrum with the MD-1 & MD-2 methods are  $(50.22 \pm 0.60) \text{ nSv/h}$  and  $(62.49 \pm 0.60) \text{ nSv/h}$  respectively. Compared to the dose equivalent calculated from the raw experimental measurement,  $(45.17 \pm 0.60 \text{ nSv/h})$ , the results by using the MD-1 and MD-2 methods are increased by 11.1 % and 38.3 % respectively.

Table 13. The summary of the dose equivalent rates (H) calculated from natural background radiation's spectra using the experimental measurements (TEPC\_EXP.), MD-1 and MD-2 methods; the percentage differences between the underestimated dose (raw experimental measurements) and the results after extrapolations below the low LET threshold.

Natural Background LET spectrum	H ( $\text{nSv/h}$ )	Percentage difference
TEPC_EXP.	$45.17 \pm 0.60$	-
TEPC_EXP. with threshold cut	$29.74 \pm 0.60$	-34.2 %
TEPC_MD-1	$50.22 \pm 0.60$	11.1 %
TEPC_MD-2	$62.49 \pm 0.60$	38.3 %

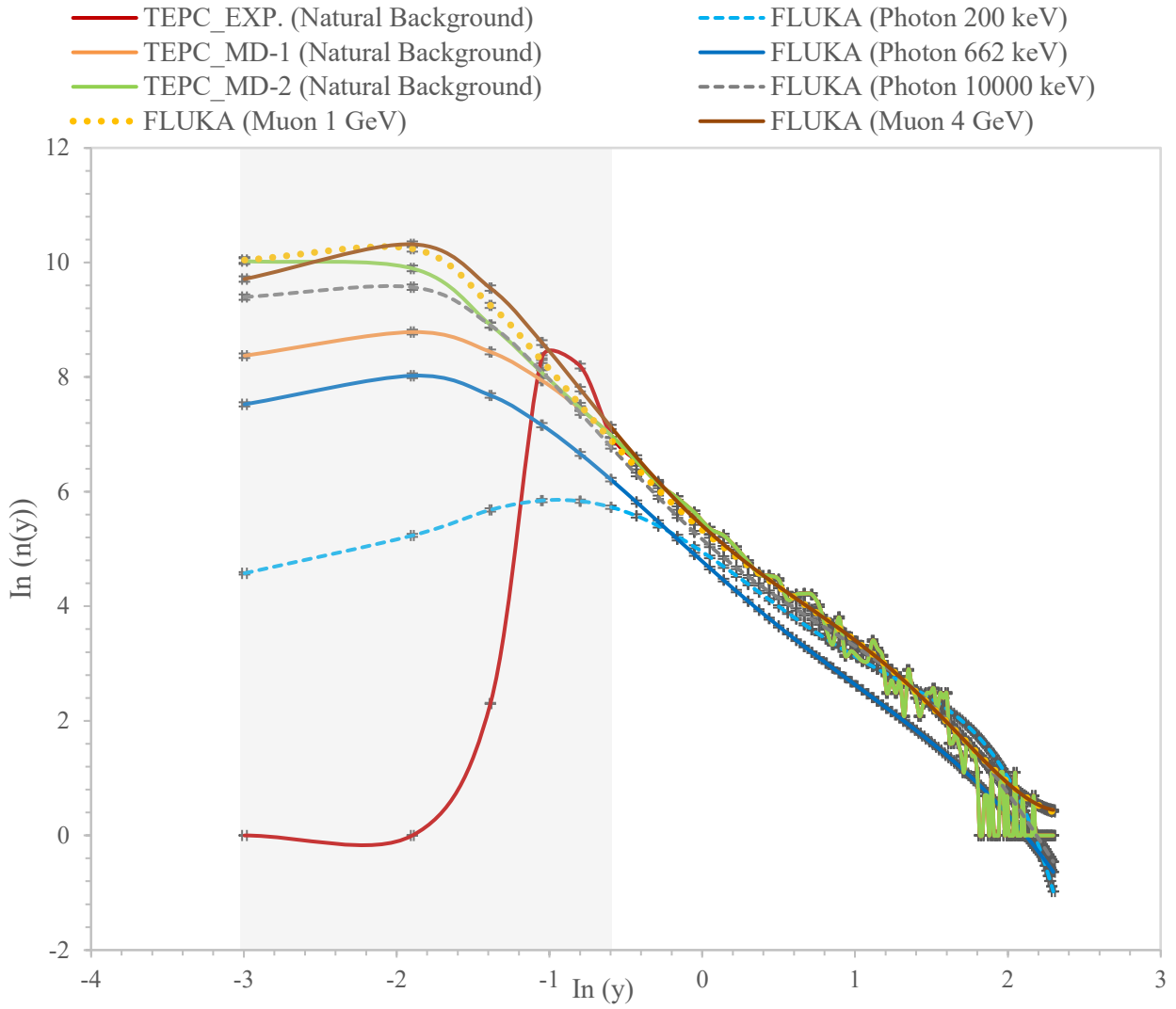


Figure 31. Comparison of experimental (natural background) and simulated dose distribution spectra for multiple monoenergetic particles incident on the simulated TEPC from 1 meter.

Also shown in figure 32, in the MD-1 method, energy deposition events are partially corrected in the region between  $0 \text{ keV}/\mu\text{m}$  and  $0.35 \text{ keV}/\mu\text{m}$ . The dose distribution with the MD-1 extrapolation is close to the simulated spectrum of 662 keV photon, i.e., it performs well in gamma dominated distribution. The dose distribution of MD-1 is very different than the simulated spectrum of 4 GeV muon. Because MD-1 employs the simulated results of 662 keV photon only, MD-1 doesn't consider the contribution of muons. The doses calculated by MD-1 will be less accurate (falsely reduced) in a mixed radiation environment, i.e., natural background/cosmic radiation fields.

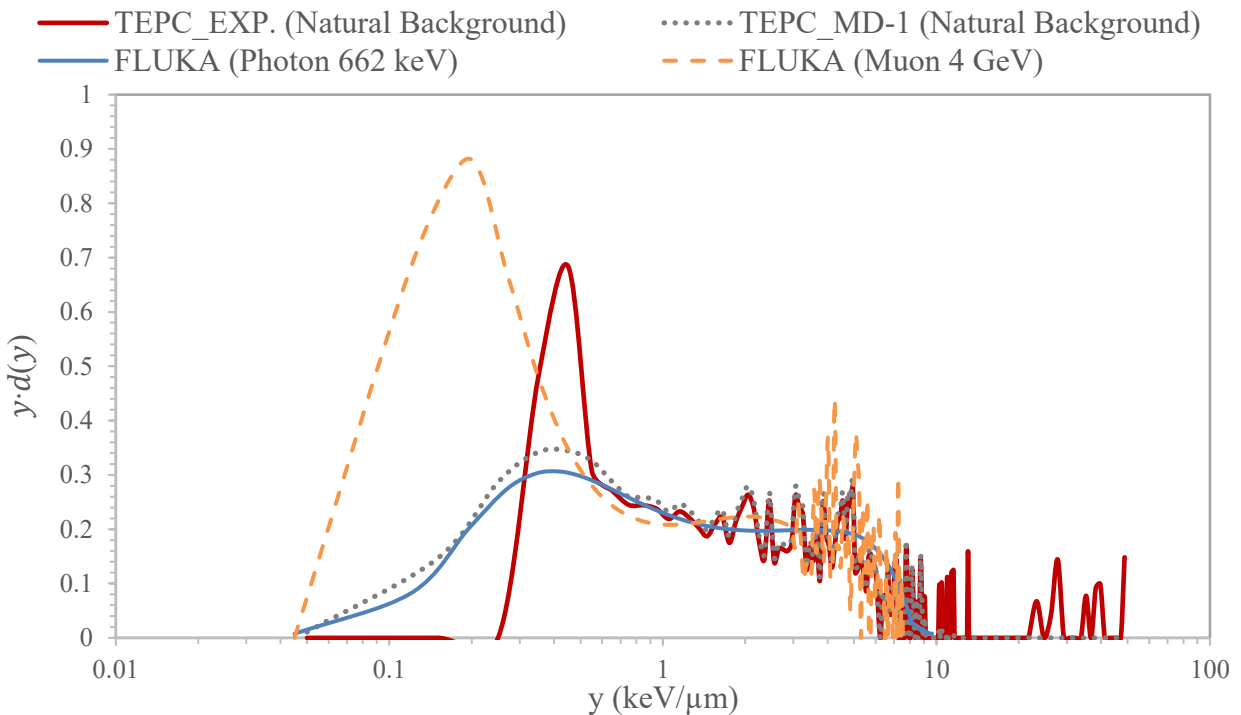


Figure 32. The dose distribution spectra of the experimental measurements with natural background radiation, the results after applying the MD-1 extrapolation method, and the FLUKA simulation with 662 keV photon and 4 GeV muon.

Also shown in figure 33, in the MD-2 method, more energy deposition events are restored in the region between  $0 \text{ keV}/\mu\text{m}$  and  $0.45 \text{ keV}/\mu\text{m}$ . The dose distribution with the MD-2 extrapolation is not biased towards gamma distribution (i.e., the simulated spectrum of 662 keV photon) or muon distribution (i.e., the simulated spectrum of 4 GeV muon). MD-2 employs the linear relation between  $\ln(n(y))$  and  $\ln(y)$  from the experimental measurements and has been tested in the simulated spectra of different monoenergetic particles (200 keV photon, 662 keV photon, 10000 keV photon, 1 GeV Muon and 4 GeV Muon). Compared to RMC and MD-1, MD-2 does a better job of indicating the changes in the radiation environment and adjusted accordingly.

In conclusion, MD-2 provides a better estimation in the very low LET region in the spectra contributed from muon or mixed radiation fields than RMC and MD-1. In natural background radiation dose measurements, the doses are contributed from cosmic and terrestrial radiation. For example, in Ottawa, the (effective) doses from cosmic and terrestrial radiation are  $0.35 \text{ mSv/yr}$ . and  $0.2 \text{ mSv/yr}$ . respectively, i.e., the ratio of doses contributed from cosmic rays to terrestrial radiation is 1.75 (Grasty & LaMarre, 2004). Although MD-2 didn't estimate the energy deposition events very well in the gamma spectrum, it is believed that MD-2 proposes a feasible and satisfactory method in extrapolating (i.e., estimating) the doses below threshold in mixed fields.

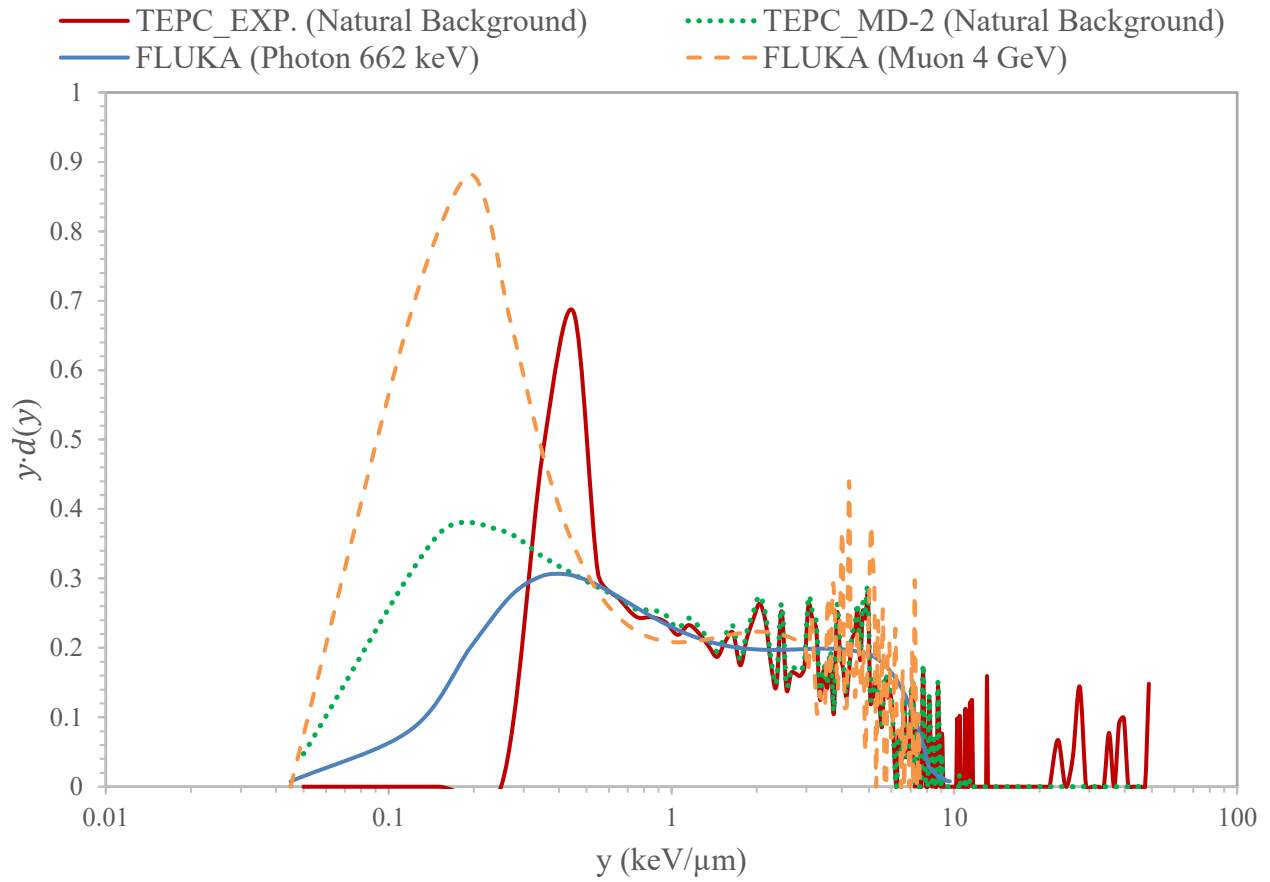


Figure 33. The dose distribution spectra of the experimental measurements with natural background radiation, the results after applying the MD-2 extrapolation method, and the FLUKA simulation with 662 keV photon and 4 GeV muon.

### 3.4 NON-NEUTRON AND NEUTRON SEPARATION

#### 3.4.1 Mixed Radiation Doses with Lineal Energy Around $10 \text{ keV}/\mu\text{m}$

The typical way to separate the spectra contributed from low LET and high LET radiation is to use the crossover channel at  $10 \text{ keV}/\mu\text{m}$ , i.e.,  $y < 10 \frac{\text{keV}}{\mu\text{m}}$  is the non-neutron spectrum (low LET) and  $y \geq 10 \frac{\text{keV}}{\mu\text{m}}$  is the neutron spectrum (high LET) (Lewis & Desormeaux, 2004).

However, the doses with LET between  $9 \text{ keV}/\mu\text{m}$  and  $12 \text{ keV}/\mu\text{m}$  or even wider range can be contributed from both non-neutron particles and neutrons. Errors are introduced when separating non-neutron (low LET) and neutron (high LET) spectra at  $10 \text{ keV}/\mu\text{m}$ . This section discusses and reveals the possibility of using a fermi-like equation on the electron-edge to better separate the non-neutron and neutron spectra instead of a straight cut at  $10 \text{ keV}/\mu\text{m}$ .

#### 3.4.2 Methods

In addition to the extrapolation methods discussed in the previous section, the improved methods (MD-1 & MD-2) also separate the low LET and high LET dose distribution spectra in a better way rather than a straight cut at  $10 \text{ keV}/\mu\text{m}$ . By employing the normalized  $^{137}\text{Cs}$  spectrum and e-edge technique discussed in section 3.1.2, the dose contributed from non-neutron particles ( $D_{\text{Non-n}}$ ) can be calculated and separated from the mixture in three steps. First, the spectrum was generated after exposure HAWK 2 to a  $^{137}\text{Cs}$  source and the fermi-like equation was fitted to the e-edge region (Figure 34). Second, the  $^{137}\text{Cs}$  spectrum was normalized and fitted to the  $^{241}\text{AmBe}$  spectrum (Figure 35 & 36). Finally, the dose contributed from the neutrons can be obtained by subtracting  $D_{\text{Non-n}}$  from the total dose (Figure 36).

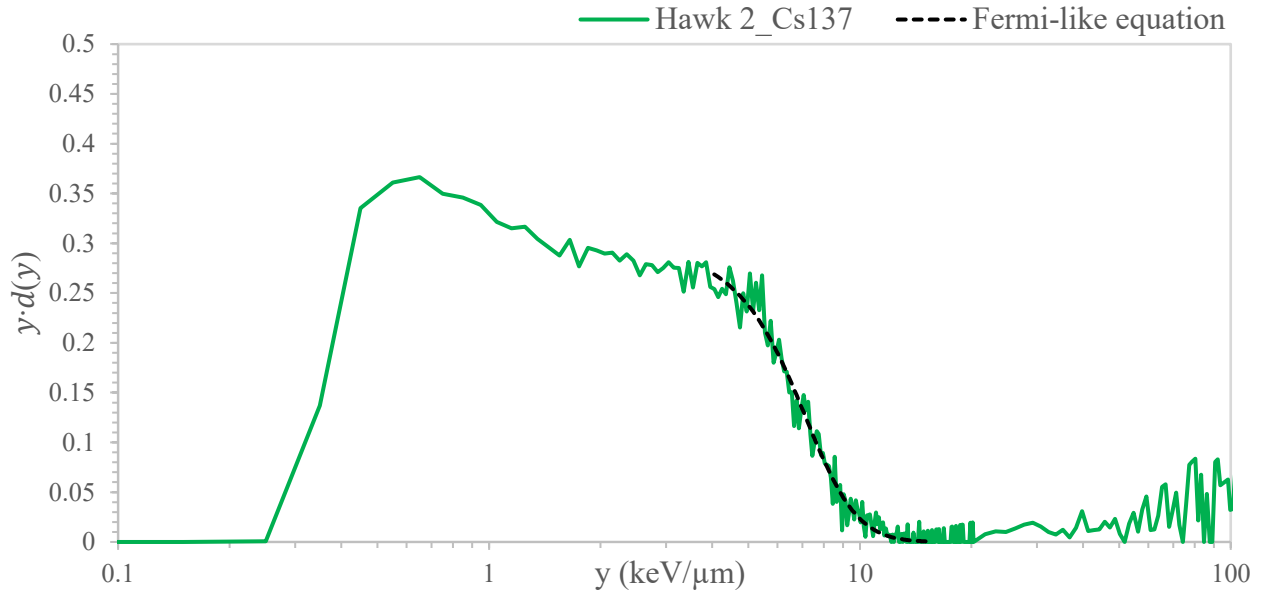


Figure 34.  $^{137}\text{Cs}$  dose distribution spectrum measured by using the HAWK 2 tissue equivalent proportional counter with fermi-like equation fitted to the electron edge.

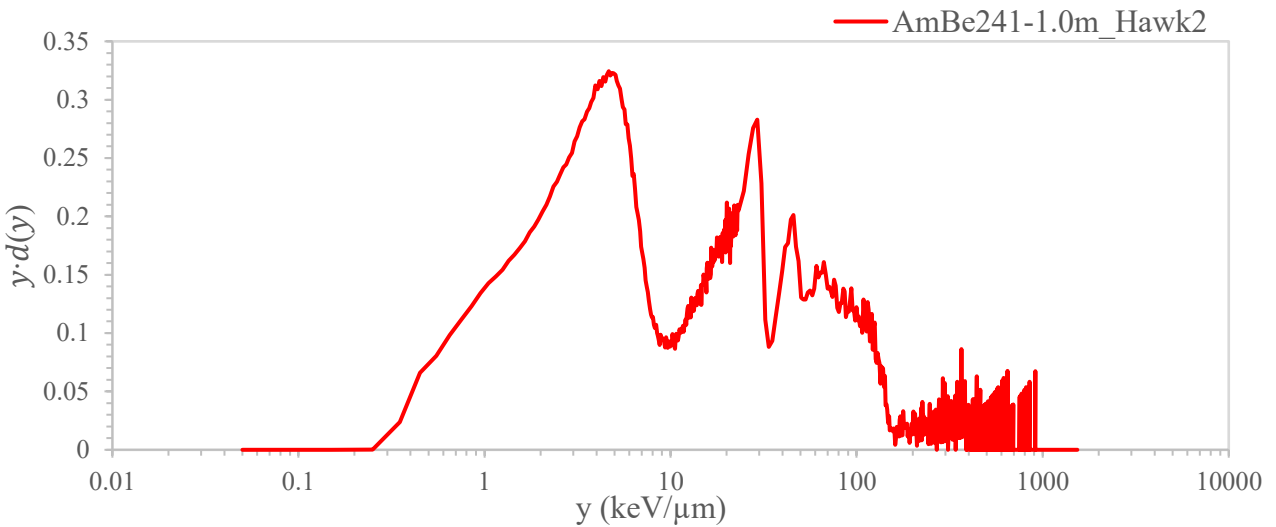


Figure 35. The dose distribution spectrum  $y \cdot d(y)$  by using the measurements done in the *AmBe* calibration experiment.

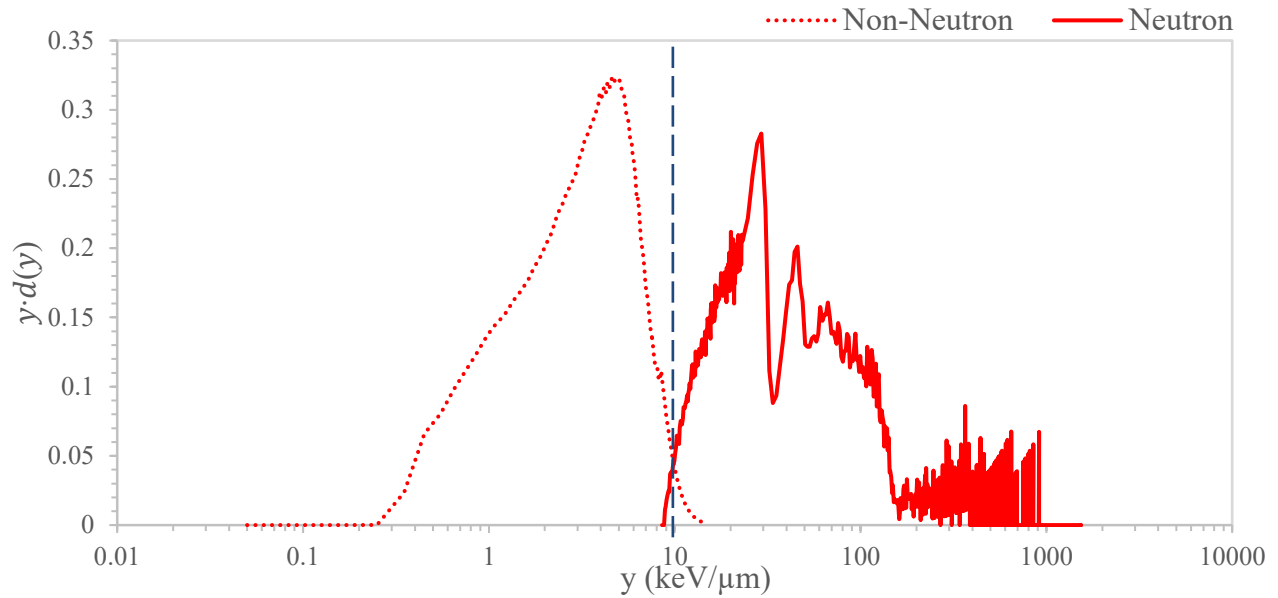


Figure 36. The separation of the non-neutron and neutron dose distribution spectra<sup>35</sup>.

### 3.4.3 Results & Discussion

It is feasible to separate the non-neutron and neutron spectra by using the Fermi-like equation fitted on the electron-edge. It revealed that the dose equivalent contributed from the non-neutron particles from  $9 \text{ keV}/\mu\text{m}$  to  $13 \text{ keV}/\mu\text{m}$  accounts for approximately 1.1 % of the total non-neutron dose. By employing the improved separation technique, MD-1 and MD-2 provide a more precise way to calculate the non-neutron contribution, resulting in more precise dose equivalents. However, it may be difficult to locate the electron-edge in some cases in which the method cannot be applied. The way to calculate the uncertainty involved is under investigation.

<sup>35</sup> The blue dashed line lies on the RMC crossover channel  $y = 10 \text{ keV}/\mu\text{m}$ .

## 4 COSMIC RADIATION DOSE MEASUREMENT

---

Chapter 4 shows the design, method, and results of two sets of experiments done in the project. Section 4.1 reveals a new approach to determine the ambient dose equivalent conversion coefficient. Section 4.2 presents the cosmic rays' dose results from experimental measurements, then employed to calibrate and compare to the analytical results calculated from the CC counts collected in RS250.

### 4.1 CONVERSION COEFFICIENT EXPERIMENT

#### 4.1.1 *Design Idea*

The typical way to determine the ambient dose equivalent conversion coefficient is to expose TEPC to a radioactive source with known  $H^*(10)$ . However, the natural background radiation, i.e., Omni-direction radiation, is totally different from the radiation generated from a point source in a laboratory. Efforts are made to develop a new method to determine the conversion coefficients by using the field measurements to replace the usage of radioactive sources.

As mentioned in Chapter 2, the  $H^*(10)$  is utilized to get consistent and comparable results from the HAWK and RS250.  $H^*(10)$  is specific to the external radiation field, regardless of the type of detectors employed. Both RS250 & HAWK measure gamma doses. The gamma  $H^*(10)$  (i.e., terrestrial gamma dose) calculated from the RS250 0-3 MeV spectra<sup>36</sup> is used as a reference to

---

<sup>36</sup> RS250 outputs the gamma dose (0-3 MeV) in terms of ambient dose equivalent ( $H^*(10)_{\text{TR}}^{\text{RS250}}$ ) directly.

determine the conversion coefficient in HAWK TEPC. Three steps are involved in determining the coefficients. The first step is to calculate the difference in the  $H^*(10)$  due to terrestrial radiation at the two locations by using RS250:

$$\Delta H^*(10)_{TR}^{RS250} = H^*(10)_{1,TR}^{RS250} - H^*(10)_{2,TR}^{RS250} \quad \text{Equation 39}$$

Where  $H^*(10)_{1,TR}^{RS250}$  and  $H^*(10)_{2,TR}^{RS250}$  are the ambient dose equivalent measured by RS250 (0-3 MeV) at location 1 and 2 respectively.

The terrestrial gamma dose at one specific location is equal to the doses measured in the HAWK TEPC low LET spectrum subtracts the dose contributed from cosmic rays. Thus, the dose equivalent ( $H$ ) measured from HAWK is:

$$H_{TR}^{TEPC} = H_{LowLET}^{TEPC} - H_{CR} \quad \text{Equation 40}$$

The difference in  $H$  due to terrestrial radiation at the two locations by using HAWK is:

$$\Delta H_{TR}^{TEPC} = (H_{LowLET}^{TEPC} - H_{CR})_1 - (H_{LowLET}^{TEPC} - H_{CR})_2 \quad \text{Equation 41}$$

The counts and doses contributed from cosmic rays are not changing much (a few percent) within a week (Mok, 2001) (Liu & Zhang, 2018). Within several days, ideally within one day, the differences in the doses contributed from cosmic-rays at ground level can be neglected, which means the difference in the doses measured by HAWK at two different locations is equivalent to the difference in the terrestrial gamma doses. In other words, the difference in  $H_{CR}$  at two locations is minor if the measurements are done on the same day at the same altitude so it

cancels with each other in equation 41. The second step calculates the difference in the  $H$  due to terrestrial radiation at the two locations by using HAWK:

$$\Delta H_{TR}^{TEPC} = H_{1,LET}^{TEPC} - H_{2,LET}^{TEPC} \quad \text{Equation 42}$$

Where  $H_{1,LET}^{TEPC}$  and  $H_{2,LET}^{TEPC}$  are the dose equivalent measured by HAWK at location 1 and 2 respectively.

The last step is to calculate the ambient dose equivalent conversion coefficient:

$$f = \frac{\Delta H_{TR}^{RS250}}{\Delta H_{TR}^{TEPC}} = \frac{H^*(10)_{1,TR}^{RS250} - H^*(10)_{2,TR}^{RS250}}{H_{1,LET}^{TEPC} - H_{2,LET}^{TEPC}} \quad \text{Equation 43}$$

Two paired experiments were designed to determine the coefficient using the improved method above, including the dock-boat experiment (Section 4.1.2) and dock-park experiment (Section 4.1.3). The terrestrial radiation doses detected at the two selected pairs (locations) should be significantly different from each other to calculate the conversion coefficient. For example, a park was chosen because it has lots of soils and rocks that can emit a significant amount of terrestrial radiation. Because water with several meters' depth can efficiently block these gamma rays (Zeb, 2007), experiment done on water or dock was chosen to pair with the park experiment. A boat experiment performed at the centre of a river (i.e., water is depth of water is approximately 90 m) is designed to eliminate most of the contamination from terrestrial radiation. And the terrestrial gamma dose detected on a dock will be partially blocked by the water surrounded it (i.e., depth of water is approximately 3 m).

#### 4.1.2 Dock-Boat Experiment

HAWKs and RS250 were placed on the dock (45.4 N, 75.8 W). The dock was approximately 30 meters away from the shore. The dock was mainly made up of concrete and rocks (Figure 37). After set-up, the instruments were operated for 2 hours, the last 77 minutes of data were used to calculate the dose equivalent to reduce the HAWK stabilization issues.

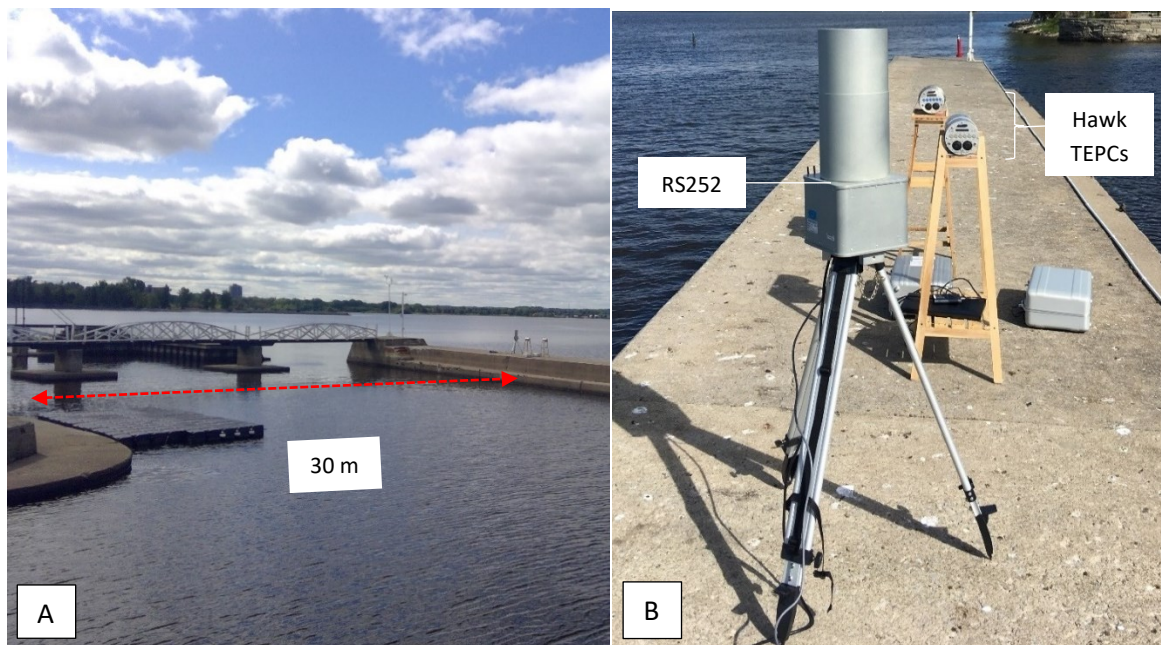


Figure 37. The side by side measurements performed on the dock on 11-Sep-2020 inside the Britannia Yacht Club, Ottawa. A. the distance between the dock and shore is approximately 30 m. B. a photo of the three instruments.

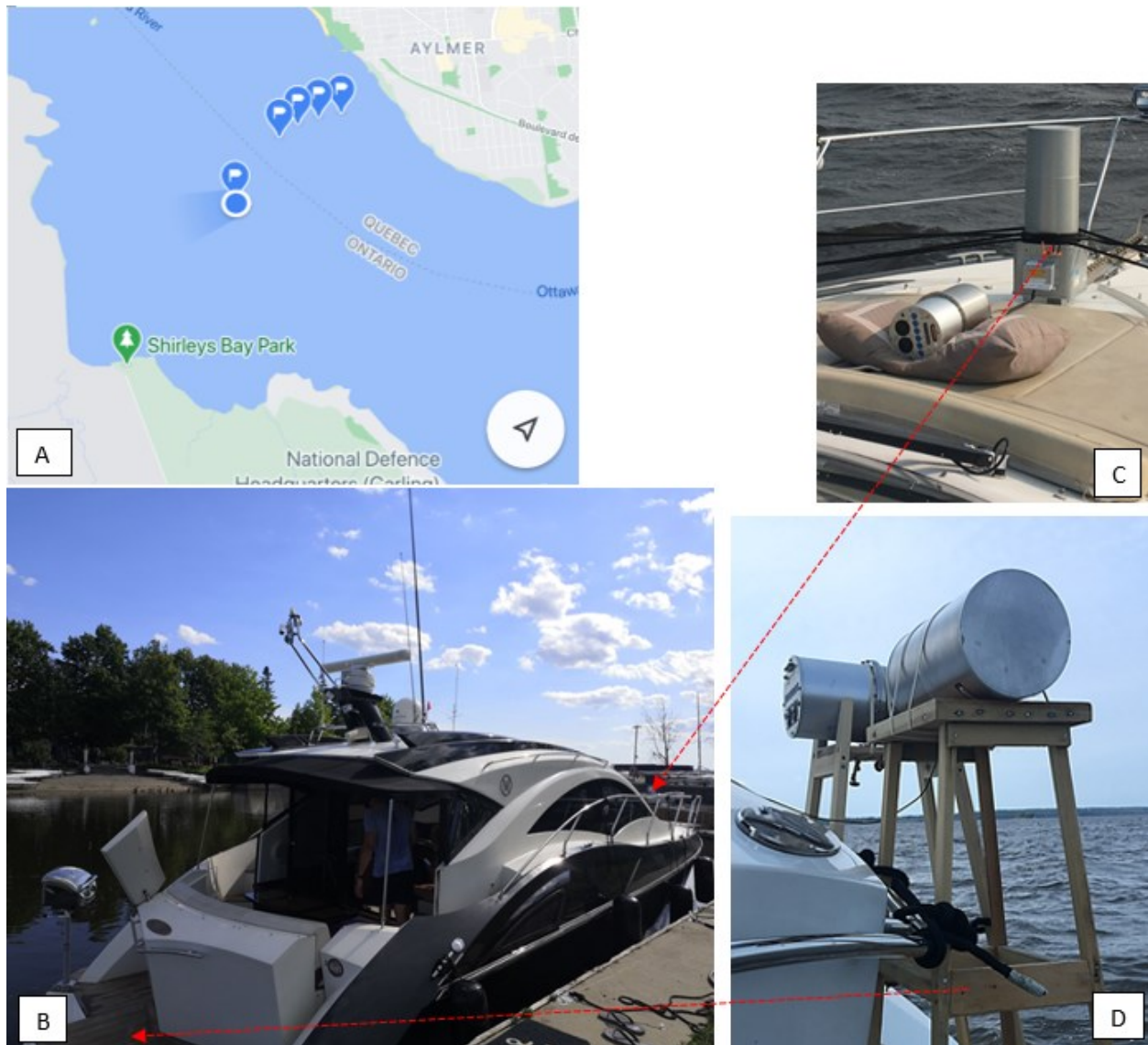


Figure 38. The set-up picture of the boat experiment performed on the centre of the Ottawa river on 16-Sep-2020.

Due to the availability of the boat and the weather condition, the second location, i.e., the boat experiment was not performed on the same day but five days later (Figure 38). Both HAWKs were placed on 1 meter wood stands and tied on the back of the boat (B & D). The RS250 was secured in the front of the boat (B & C). HAWK 2 was moved to the front when the boat arrived

at the centre of the Ottawa river). The RS250 was not successfully stabilized until the boat arrived at the river centre (45.4 N, 75.8 W). All instruments were operated for 2 hours, the last 77 minutes of data were used in the data analysis.

#### *4.1.3 Dock-Park Experiment*

HAWKs and RS250 were placed on the far end of the dock (44.7 N, 76.3 W). The dock was approximately 70 meters away from the shore (Figure 39 A). The dock was mainly made up of wood (Figure 39 B). RS-250 and two HAWKs. All the instruments were secured on 1 meter stand. On 03-Aug-2021, the humidity was 63%, and the day temperature was between 21 °C and 26 °C. The same experiment was performed in the park on the same day (Figure 40). In both settings, the instruments were operated for 3 hours, the last 152 minutes of data were used to calculate the dose equivalent.

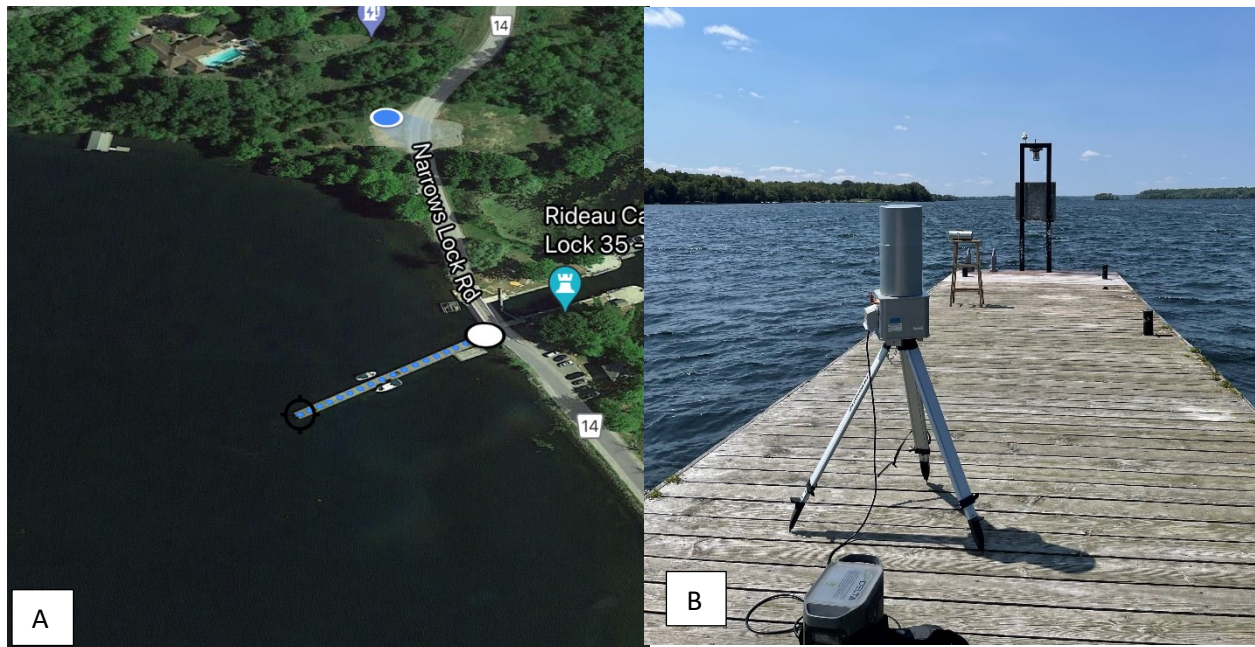


Figure 39. The set-up picture of the field measurements performed on the dock near the Rideau Canal Lock 35-Narrows on 03-Aug-2021.

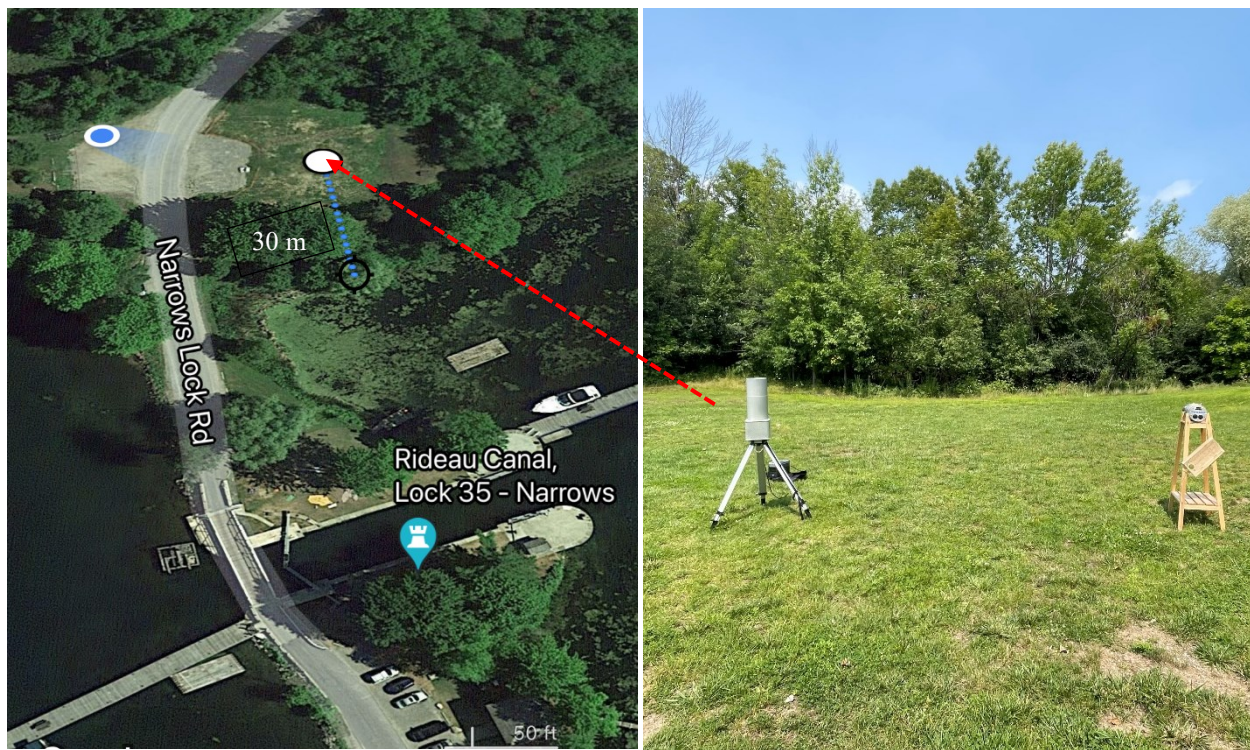


Figure 40. The set-up picture of the field measurements performed in the park near the Rideau Canal Lock 35-Narrows on 03-Aug-2021.

#### 4.1.4 Results

Table 14. The summary of the ambient dose equivalent rates  $H^*(10)$  contributed from terrestrial radiation ( $H^*(10)_{TR}$ ) non-neutron cosmic radiation ( $H^*(10)_{Non-n. CR}$ ) and cosmic radiation including neutron ( $H^*(10)_{With n. CR}$ ) measured at different times and locations by using the counts collected from RS250 in 15 min.

Date			RS250		
			$H^*(10)_{TR}$ (nSv/h)	$H^*(10)_{Non-n. CR}$ (nSv/h)	$H^*(10)_{With n. CR}$ (nSv/h)
#1	11-Sep-2020	Dock	$17.80 \pm 0.36$	$35.9 \pm 1.2$	$46.521 \pm 0.022$
	16-Sep-2020	Boat	$5.77 \pm 0.12$	$37.9 \pm 1.1$	$50.522 \pm 0.022$
	$\Delta H^*(10)$		$12.03 \pm 0.38$	$2.0 \pm 1.6$	$4.001 \pm 0.031$
#2	03-Aug-2020	Dock	$13.29 \pm 0.27$	$37.42 \pm 0.69$	$49.6 \pm 1.4$
	03-Aug-2020	Park	$35.40 \pm 0.71$	$37.72 \pm 0.69$	$50.2 \pm 1.4$
	$\Delta H^*(10)$		$22.11 \pm 0.76$	$0.30 \pm 0.98$	$0.6 \pm 2.0$

Table 14 presents  $H^*(10)$  contributed from terrestrial radiation ( $H^*(10)_{TR}$ ) non-neutron cosmic radiation ( $H^*(10)_{Non-n. CR}$ ) and cosmic radiation including neutron ( $H^*(10)_{With n. CR}$ ) calculated from the counts collected in 15 min from RS250. In the first dock experiment (11-Sep-2020),  $H^*(10)_{Dock}^{RS250}$  contributed from the terrestrial radiation, non-neutron cosmic radiation and total cosmic radiation are  $17.80 \pm 0.36$  nSv/h,  $35.9 \pm 1.2$  nSv/h, and  $46.521 \pm 0.022$  nSv/h respectively. In the boat experiment (16-Sep-2020),  $H^*(10)_{Boat}^{RS250}$  from the terrestrial radiation, non-neutron cosmic radiation and cosmic radiation, including neutron are  $5.77 \pm 0.12$  nSv/h,  $37.9 \pm 1.1$  nSv/h, and  $50.522 \pm 0.022$  nSv/h respectively. The difference between the two  $H^*(10)_{TR}$  results obtained at dock and shore is  $12.03 \pm 0.38$  nSv/h. Also as expected, the difference between the cosmic radiation doses measured at two places within 5

days is not remarkably large: the difference in  $H^*(10)_{Non-n. CR}$  is  $2.0 \pm 1.6 \text{ nSv/h}$ , and the difference in  $H^*(10)_{With n. CR}$  is  $4.001 \pm 0.031 \text{ nSv/h}$ .

In the more recent dock experiment (03-Aug-2021), the RS250  $H^*(10)_{TR}$ ,  $H^*(10)_{Non-n. CR}$  and  $H^*(10)_{With n. CR}$  are  $13.29 \pm 0.27 \text{ nSv/h}$ ,  $37.42 \pm 0.69 \text{ nSv/h}$ , and  $49.6 \pm 1.4 \text{ nSv/h}$  respectively.

In the park experiment (03-Aug-2021), the RS250  $H^*(10)_{TR}$ ,  $H^*(10)_{Non-n. CR}$  and  $H^*(10)_{With n. CR}$  are  $35.40 \pm 0.71 \text{ nSv/h}$ ,  $37.72 \pm 0.69 \text{ nSv/h}$ , and  $50.2 \pm 1.4 \text{ nSv/h}$  respectively (Table 14). The  $H^*(10)_{TR}$  measured at the dock is  $22.11 \pm 0.76 \text{ nSv/h}$  less than the quantity measured at the park. The differences in  $H^*(10)_{Non-n. CR}$  or  $H^*(10)_{With n. CR}$  measured at dock and park on 03-Aug-2021 are less than  $0.7 \text{ nSv/}$  (Table 14).

Table 15 presents dose equivalents ( $H_s$ ) and the difference between them at different locations by using the measurements from HAWK with three analysis methods: RMC, MD-1 and MD-2. The differences between  $H_s$  measured at the Dock (16-Sep-20) and Boat (11-Sep-20), which is the  $H$  contributed from terrestrial radiation, are  $12.8 \pm 1.1 \text{ nSv/h}$  (RMC),  $13.6 \pm 1.1 \text{ nSv/h}$  (MD-1), and  $19.1 \pm 1.1 \text{ nSv/h}$  (MD-2) respectively (Table 15). The ambient dose equivalent conversion coefficients ( $f$ ) is  $0.630 \pm 0.041$  by using the MD-2 method (Table 16), which is smaller than the RMC published  $f$  (Lewis & Desormeaux, 2004) (McCall, 2000). The  $f$ s generated by the MD-1 method ( $0.885 \pm 0.078$ ) and by the RMC method ( $0.94 \pm 0.21$ ) are close to the literature values (Table 16).

For HAWK TEPC, the dose equivalents ( $H$ ) measured on 03-Aug-2021 and calculated from the three different methods (RMC, MD-1 & MD-2) are presented in Table 15. The differences in the dose equivalents, i.e., the dose difference from terrestrial radiation detected at two locations,  $\Delta H_{TR}^{RMC}$ ,  $\Delta H_{TR}^{MD-1}$  and  $\Delta H_{TR}^{MD-2}$  are  $12.63 \pm 0.71$  nSv/h,  $13.50 \pm 0.78$  nSv/h, and  $15.60 \pm 0.80$  nSv/h respectively.

Table 15. The dose equivalent rates  $H$  contributed from non-neutron radiation measured at different time and locations by using HAWK 2 and four different analysis methods (RMC, MD-1, MD-2).

Date		Location	HAWK TEPC		
			$H_{RMC}$ (nSv/h)	$H_{MD-1}$ (nSv/h)	$H_{MD-2}$ (nSv/h)
#1	11-Sep-2020	Dock	$39.40 \pm 0.81$	$43.87 \pm 0.81$	$63.28 \pm 0.83$
	16-Sep-2020	Boat	$26.60 \pm 0.68$	$30.13 \pm 0.68$	$44.18 \pm 0.70$
	$\Delta H_{TR}^{TEPC}$		$12.8 \pm 1.1$	$13.6 \pm 1.1$	$19.1 \pm 1.1$
#2	03-Aug-2021	Dock	$32.0 \pm 0.50$	$36.80 \pm 0.50$	$53.43 \pm 0.51$
	03-Aug-2021	Park	$44.63 \pm 0.50$	$50.30 \pm 0.60$	$69.03 \pm 0.61$
	$\Delta H_{TR}^{TEPC}$		$12.63 \pm 0.71$	$13.50 \pm 0.78$	$15.60 \pm 0.80$

Table 16 shows that the low LET conversion coefficients of RMC, MD-1, MD-2 are larger than the published values from RMC. The ambient dose equivalent conversion coefficients ( $f$ ) are  $1.75 \pm 0.12$ ,  $1.64 \pm 0.11$  and  $1.42 \pm 0.10$  by using the RMC, MD-1, and MD-2 methods respectively.

Table 16. The post-measurement calibration results of the low LET ambient dose equivalent coefficient  $f$  for non-neutron cosmic radiation field by using  $\Delta H^*(10)_{TR}^{RS250} / \Delta H_{TR}^{TEPC}$  (Equation 43).

Experiment	$f$			
	RMC	MD-1	MD-2	RMC Literature Values <sup>37</sup>
Dock-Boat	$0.940 \pm 0.086$	$0.885 \pm 0.078$	$0.630 \pm 0.041$	0.80-0.95
Dock-Park	$1.75 \pm 0.12$	$1.64 \pm 0.11$	$1.42 \pm 0.10$	

#### 4.1.5 Conclusion and Discussion

$\Delta H^*(10)$  measured at two different locations is resulted from the variation in the terrestrial radiation dose. The cosmic radiation dose slightly varies from 11-Sep-2020 to 16-Sep-2020 but is almost unchanged on the same day (03-Aug-2021) (Table 14). Systematic errors are introduced when the measurements at the two comparing locations are not performed on the same day. In other words, the results gained from the Dock-Park experiment done on 03-Aug-2021 involve minor systematic errors.

The low LET ambient dose equivalent conversion coefficients in the paired experience don't agree with the RMC literature value (Table 16). But it shows the potential to determine the ambient dose equivalent conversion coefficient by utilizing Equations 39-43. HAWK in the dock-boat and dock-park experiments was operated for several hours only. The uncertainties will be reduced if the duration of the measurements is longer. More experiments should be done in

<sup>37</sup> The equation  $H^*(10) = 0.87 \cdot H^{TEPC}$  was published by RMC in 2000 (McCall, 2000). The equation  $H^*(10) = 0.95 \cdot H_{Low\ LET}^{TEPC} + 0.80 \cdot H_{High\ LET}^{TEPC}$  was published by RMC in 2004, where 0.95 and 0.80 are the ambient dose equivalent conversion coefficients for low LET and high LET respectively (Lewis & Desormeaux, 2004).

different geographic locations to improve the conversion coefficient results. Because the conversion coefficient experiment by using pair measurements requires further investigations, the conversion coefficients published in RMC will be employed to convert  $H$  to  $H^*(10)$  in the next section.

## 4.2 INTERCALIBRATING EXPERIMENTAL MEASUREMENTS WITH ANALYTICAL DOSE RESULTS

### 4.2.1 Introduction

The goal of the thesis is to calibrate and compare the  $H^*(10)$  obtained from the analytical model using RS250 with the experimental measurement from HAWK TEPC. This section presents the comparison by using the three methods (RMC, MD-1 & MD-2). Eight locations with different geological and geographic features in Ottawa and Gatineau, including one FPS station located at the RPB, are chosen (Table 17).

Table 17. The eight experiments' measurement dates, geological and geographic features.

Date	Location	Land type	Altitude	GPS	Test duration (min)
11-Sep-2020	Britannia Beach (dock)	Concrete dock	65m	45.37 N 75.80 W	81
16-Sep-2020	Ottawa River (centre)	Boat on Water	58m	45.39N 75.86 W	77
22-Jun-2021	Ottawa FPS station- RPB	Concrete	89m	45.37 N 75.68 W	1336
28-Jun-2021	Walter Baker Park	Grassland	96m	45.29N 75.90W	151
29-Jun-2021	Camp fortune, Gatineau Park	Rock & Mountain	264m	45.51N 75.85W	196
03-Jul-2021	Burnt lands provincial park	Grassland	160m	45.26N 76.15W	286
03-Aug-2021	Rideau Canal Narrows (Lock 35- dock)	Wood and Stone	124m	44.70N 76.29W	152
03-Aug-2021	Rideau Canal Narrows (Lock 35- park)	Grassland	127m	44.70N 76.30W	152

#### 4.2.2 Method

##### I. Experimental measurement

The HAWKs and RS250 were installed on a flat and open space, away from the trees and other obstructions. Depending on the weather, the availability and accessibility of the location, the three instruments were operated simultaneously for hours. The data was stored automatically in the SD-cards and downloaded to a PC for analysis. The experiment setup performed in the parking lot on the hill of the Gatineau Park on 29-Jun-2021 was shown (Figure 41).



Figure 41. Set-up picture of the experiments performed on the hill of the Gatineau Park on 29-Jun-2021.

The ambient dose equivalent (rates) contributed from terrestrial radiation was obtained from the 0-3 MeV spectrum of RS250. The conversion coefficients from RMC for low LET (0.95) and high LET (0.80) are employed to convert the measure dose equivalent from HAWK TEPC to  $H^*(10)$  (Lewis & Desormeaux, 2004). The experimental  $H^*(10)$  of non-neutron cosmic radiation can be calculated from:

$$H^*(10)_{Non-n. CR}^{TEPC} = 0.95 \cdot H_{Low LET}^{TEPC} - H^*(10)_{TR}^{RS250} \quad \text{Equation 44}$$

And the experimental cosmic  $H^*(10)$  including the neutron can be calculated from:

$$H^*(10)_{With n. CR}^{TEPC} = 0.95 \cdot H_{Low LET}^{TEPC} + 0.80 \cdot H_{High LET}^{TEPC} - H^*(10)_{TR}^{RS250} \quad \text{Equation 45}$$

Where  $H^*(10)_{Non-n. CR}^{TEPC}$  and  $H^*(10)_{With n. CR}^{TEPC}$  are the experimental  $H^*(10)$  contributed from non-neutron cosmic radiation and cosmic  $H^*(10)$  including the neutron respectively.  $H_{Low LET}^{TEPC}$  is the dose equivalent calculated from the low LET spectrum of HAWK TEPC.  $H_{High LET}^{TEPC}$  is the dose equivalent calculated from the high LET spectrum of HAWK TEPC.  $H^*(10)_{TR}^{RS250}$  is the ambient dose equivalent calculated from the measurements in RS250 from 0-3 MeV. Equation 45 and 46 are derived from equation 14 & 15 (Chapter 1).

## II. FLUKA simulation

FLUKA application was employed to simulate the response of TEPC with exposure to 5 different monoenergetic beams, including muon with kinetic energy of 1 GeV, muon with kinetic energy of 4 GeV, photon with kinetic energy of 200 keV, photon with kinetic energy of 662 keV and photon with kinetic energy of 10000 keV.

After the simulations were done, the natural log of the counts ( $\ln(n(y))$ ) are plotted against the natural log of the lineal energy ( $\ln(y)$ ) to produce the counts distribution spectra. As discussed in section 3.3.4, the count's distribution from  $0.55 \text{ keV}/\mu\text{m}$  to  $1.05 \text{ keV}/\mu\text{m}$  can be fitted as a linear equation. The slopes of the linear best fit equations were calculated to find how it will link to the proportion of the cosmic radiation's dose in the total natural dose (CR and TR), or

similarly,  $\frac{H^*(10)_{CR}}{H^*(10)_{TR}}$ .

#### 4.2.3 Results From the Measurements Done at the Ottawa FPS Station

Figure 42 shows the dose distribution spectrum measured at the Ottawa FPS station, without extrapolations/ corrections. It represents two similar structures in the dose distribution spectra measured at the 8 locations. 1. As discussed in Section 3.3, there are almost no energy deposition events detected below  $0.5 \text{ keV}/\mu\text{m}$  (threshold), which should be corrected using MD-1 & MD-2. 2. There is an e-edge observed at around  $10 \text{ keV}/\mu\text{m}$ . 3. No p-edge can be found. In the dose distribution spectrum above  $150 \text{ keV}/\mu\text{m}$ , the curve becomes a series of "spikes", this results from few (one or two) counts collected in each channel (bin), which are heavily weighted by their dose (i.e.,  $y^2$ ).

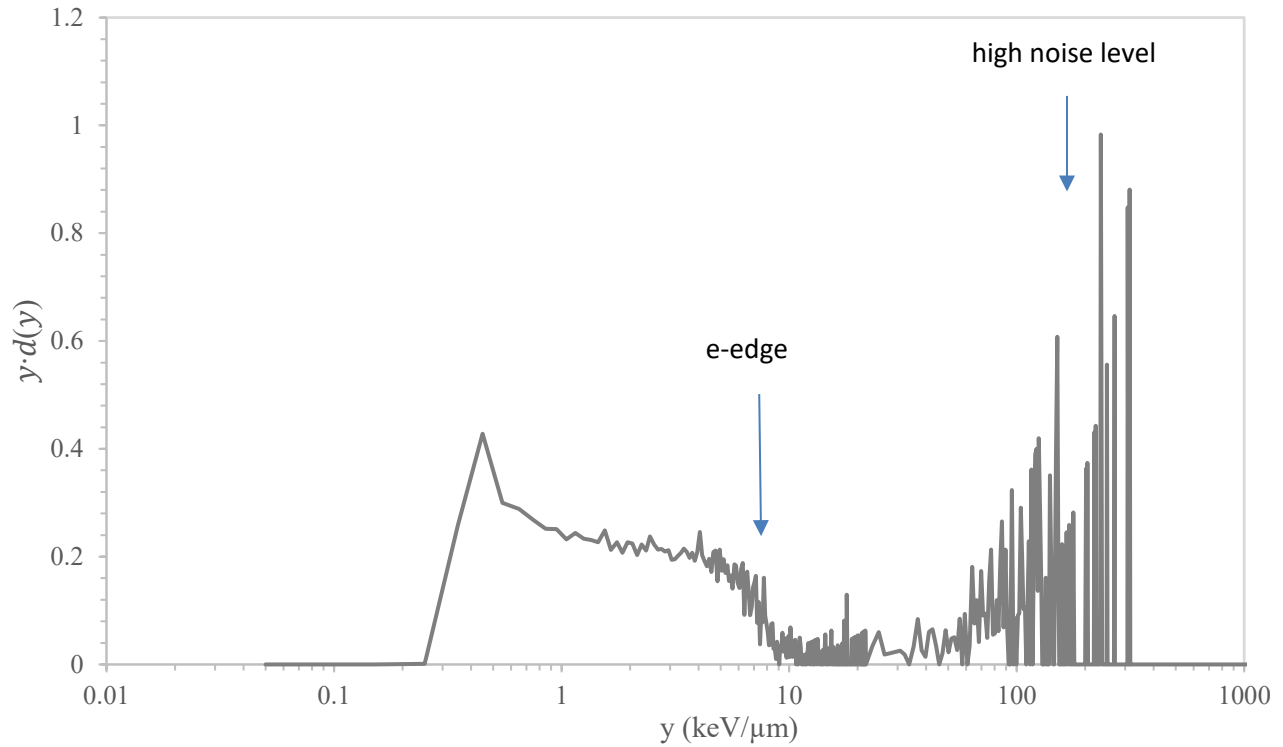


Figure 42. A typical dose distribution spectrum produced from HAWK TEPC by using the experimental measurements for background radiation done at the Ottawa FPS station (RPB) on 22-June-2021.

After corrections, the non-neutron cosmic rays' ambient dose equivalents are  $(16.8 \pm 1.6) \text{ nSv/h}$  and  $(31.5 \pm 4.7) \text{ nSv/h}$  for MD-1 and MD-2 respectively. To have an idea how accurate these dose results are, the experimental results collected at the Ottawa FPS station by HAWK TEPC are compared to some published results. According to the survey done in 2009, the Canadian population-weighted average effective dose contributed from the non-neutron and with neutron cosmic rays were  $30.1 \text{ nSv/h}$  and  $35.4 \text{ nSv/h}$ <sup>38</sup> respectively (Chen, 2009). A similar survey was

<sup>38</sup> The Canadian population-weighted average effective dose contributed from cosmic rays is  $0.31 \text{ mSv/h}$  with 15 % contributed from neutron.

done in Ottawa, and the population-weighted average effective dose contributed from the cosmic rays including neutron was  $40.0 \text{ nSv/h}$  (Grasty & LaMarre, 2004). Because the effective dose is approximately equal to  $H^*(10)$  in the case of cosmic rays' exposure at ground level (Chabot, 2015) (Ellaschuk, 2001). For example, the ratio of effective dose and ambient dose equivalent is between 0.8 and 0.9 for photons with energy ranging from approximately 0.06 MeV to 10 MeV (Chabot, 2015), it can be concluded that the non-neutron cosmic rays  $H^*(10)$  by using MD-2 method agree with the published results.

The cosmic rays' ambient dose equivalents including contributions from neutron are  $(181.3 \pm 3.5) \text{ nSv/h}$  and  $(195.9 \pm 5.6) \text{ nSv/h}$  by using MD-1 and MD-2 respectively. Both  $H^*(10)_{\text{With-n. CR}}^{\text{TEPC}}$  (MD-1 & MD-2) are much higher than the published results  $35.4 \text{ nSv/h}$  in Canada (Chen, 2009) and  $40.0 \text{ nSv/h}$  in Ottawa (Grasty & LaMarre, 2004). Together with the “spikes” observed in the high LET region, it can be concluded that there is a high noise issue in HAWK when measuring the natural background radiation at ground level. The following sections will focus on presenting the  $H^*(10)$  results from non-neutron cosmic rays.

Additionally, the comparisons between the CR/TR ratios by using RS250 & HAWK at all eight locations (Table 25), and the  $H^*(10)$  results relevant to the cosmic radiation including neutron (Table 26 & 27) can be found in the Appendix B.

#### 4.2.4 Analytical Results (RS250) & Experimental Results by Using the RMC Method

Table 18. The CC count rates, analytical  $H^*(10)$ s and the ratio of  $H^*(10)_{CR}^{RS250} / H^*(10)_{TR}^{RS250}$  contributed from non-neutron and with neutron cosmic radiation measured at 8 different locations by using RS250.

Date	Locations	Land type	Count rates (cps)	$\frac{H^*(10)_{Non-n. CR}^{RS250}}{H^*(10)_{TR}^{RS250}}$	$H^*(10)_{CR}^{RS250}$ (nSv/h)	
				CR/TR Ratio <sup>39</sup>	non neutron	including neutron
20210622	RPB	Concrete	2.291 ± 0.050	1.544 ± 0.036	35.84 ± 0.67	46.4 ± 1.3
20200911	Britannia Beach (dock)	Concrete dock	2.294 ± 0.050	2.017 ± 0.061	35.89 ± 0.67	46.5 ± 1.3
20210628	Walter Baker Park	Grassland	2.375 ± 0.051	0.7821 ± 0.0089	36.97 ± 0.68	48.7 ± 1.4
20210803	Rideau Canal Narrows (Lock 35- dock)	Wood and Stone	2.409 ± 0.052	2.82 ± 0.11	37.42 ± 0.69	49.6 ± 1.4
20210803	Rideau Canal Narrows (Lock 35- park)	Grassland	2.431 ± 0.052	1.066 ± 0.016	37.72 ± 0.69	50.2 ± 1.4
20200916	Ottawa River	Boat on Water	2.444 ± 0.052	6.57 ± 0.61	37.88 ± 0.69	50.5 ± 1.4
20210703	Burnt Lands Provincial Park	Grassland	2.490 ± 0.053	1.500 ± 0.032	38.50 ± 0.70	51.8 ± 1.4
20210629	Gatineau Park	Rock & Concrete	2.514 ± 0.053	0.8151 ± 0.0092	38.82 ± 0.70	52.4 ± 1.4

Table 18 summaries the analytical results calculated by using the measurements from RS250, including the count rates from the CC channel (Count rate in cps), the ratio of ambient dose equivalents contributed from non-neutron cosmic radiation to terrestrial radiation

$\left(\frac{H^*(10)_{Non-n. CR}^{RS250}}{H^*(10)_{TR}^{RS250}}\right)$ , the analytical  $H^*(10)$  from cosmic rays (CR) by using equation 12 & 13

(Section 1.4.2). The minimum and maximum cosmic rays' count rate are  $2.291 \pm 0.050$  cps

(Ottawa FPS station (RPB)) and  $2.514 \pm 0.053$  cps (Gatineau Park (Camp fortune)) respectively.

<sup>39</sup> The CR/TR ratio calculated by using the  $H^*(10)$  results from RS250 is applied in figure 44, 46, 48, 49 & 51. The ratio calculated from the cosmic rays' dose measured by HAWK is present in the Appendix B, table 25. The different between the ratios by using the measurements from RS250 and HAWK is not significant.

The ratio of  $\frac{H^*(10)_{Non-n. CR}^{RS250}}{H^*(10)_{TR}^{RS250}}$  ranges from  $0.7821 \pm 0.0089$  (Walter Baker Park) to  $6.57 \pm 0.61$  (Centre of Ottawa River).

Table 19. The summary of experimental  $H^*(10)$  contributed from non-neutron cosmic radiation measured at 8 different locations by using HAWK TEPC and the analysis method (RMC).

Date	Locations	$H^*(10)_{Non-n. CR}^{TEPC, RMC}$ (nSv/h)	$\frac{\Delta H^*(10)_{Non-n. CR}}{H^*(10)_{Non-n. CR}^{RS250}}$
20210622	RPB	$12.72 \pm 0.68$	-64.5 %
20200911	Britannia Beach (dock)	$22.7 \pm 1.0$	-36.7 %
20210628	Walter Baker Park	$3.77 \pm 0.90$	-89.8 %
20210803	Rideau Canal Narrows (Lock 35- dock)	$20.12 \pm 0.80$	-46.0 %
20210803	Rideau Canal Narrows (Lock 35- park)	$10.11 \pm 0.80$	-73.2 %
20200916	Ottawa River	$22.56 \pm 0.92$	-40.4 %
20210703	Burnt Lands Provincial Park	$14.98 \pm 0.76$	-61.1 %
20210629	Gatineau Park	$3.21 \pm 0.84$	-91.7 %

Table 19 summarizes the experimental  $H^*(10)$  contributed from non-neutron cosmic rays (Non-n. CR) using the HAWK measurements, and after correcting with the RMC method, i.e.,

$H^*(10)_{Non-n. CR}^{TEPC, RMC}$ , and the percentage discrepancies<sup>40</sup> between the experimental measurements

and the analytical RS250 dose results, i.e.,  $\frac{\Delta H^*(10)_{Non-n. CR}}{H^*(10)_{Non-n. CR}^{RS250}}$ . Compared to the analytical results

calculated from the CC channel of RS250, all  $H^*(10)_{Non-n. CR}^{TEPC, RMC}$  are low. It reveals that minimum

and maximum discrepancies are -36.7 % (Britannia Beach) and -91.7 % (Gatineau Park) (Table

19). The comparisons are visual in Figure 43 between the experimental (RMC) and analytical

(RS250) cosmic non-neutron  $H^*(10)$ s over count rates of the CC channel in RS250, where the

maximum discrepancy between experimental and analytical results takes place at  $2.514 \pm 0.053$

<sup>40</sup> The percentage discrepancy is calculated by using the experimental  $H^*(10)$  minus the analytical result and divided by the analytical result.

cps, and the minimum discrepancy takes place at  $2.294 \pm 0.050$  cps. The relationship between

$H^*(10)_{Non-n.CR}^{TEPC, RMC}$  and count rate is not linear (Figure 43).

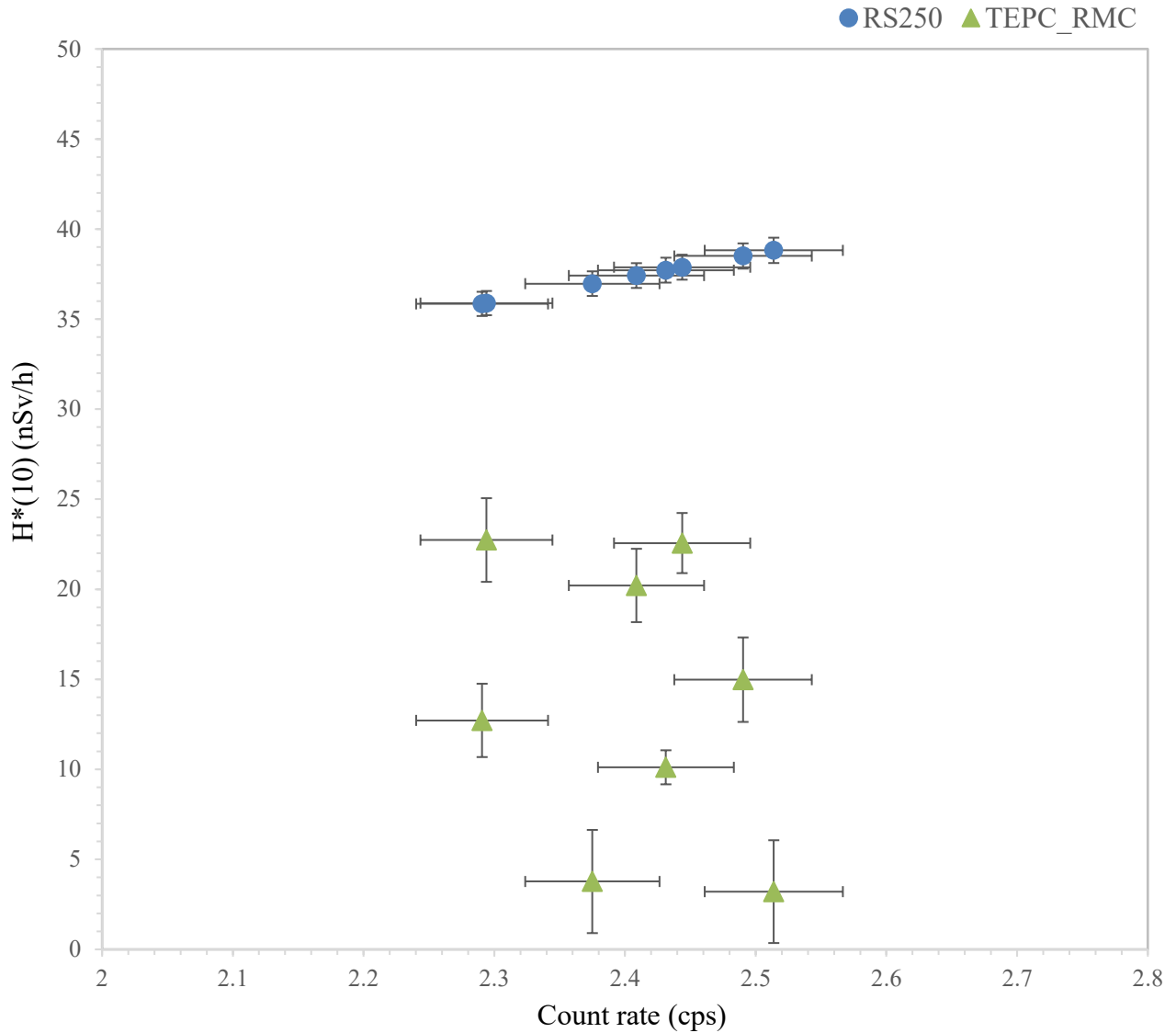


Figure 43. The comparison between experimental and analytical cosmic non-neutron  $H^*(10)s$  with respect to the changes along with the count rate of the CC channel in RS250. Error bars represent the uncertainties on the RS250 CC count rates detected at the 8 locations (x-axis) and  $H^*(10)$  (y-axis) from tables 18 and 19.

The comparisons are also made in Figure 44 between the experimental (RMC) and analytical (RS250) cosmic non-neutron  $H^*(10)$ s over different ratio of  $H^*(10)_{CR}^{RS250}/H^*(10)_{TR}^{RS250}$  (CR/TR), where the maximum discrepancy between experimental and analytical results takes place at  $0.8151 \pm 0.0092$ , and the minimum discrepancy takes place at  $2.017 \pm 0.061$ . The discrepancy between TEPC\_RMC and RS250 increases as the  $H^*(10)$  ratio of CR to TR decreases.

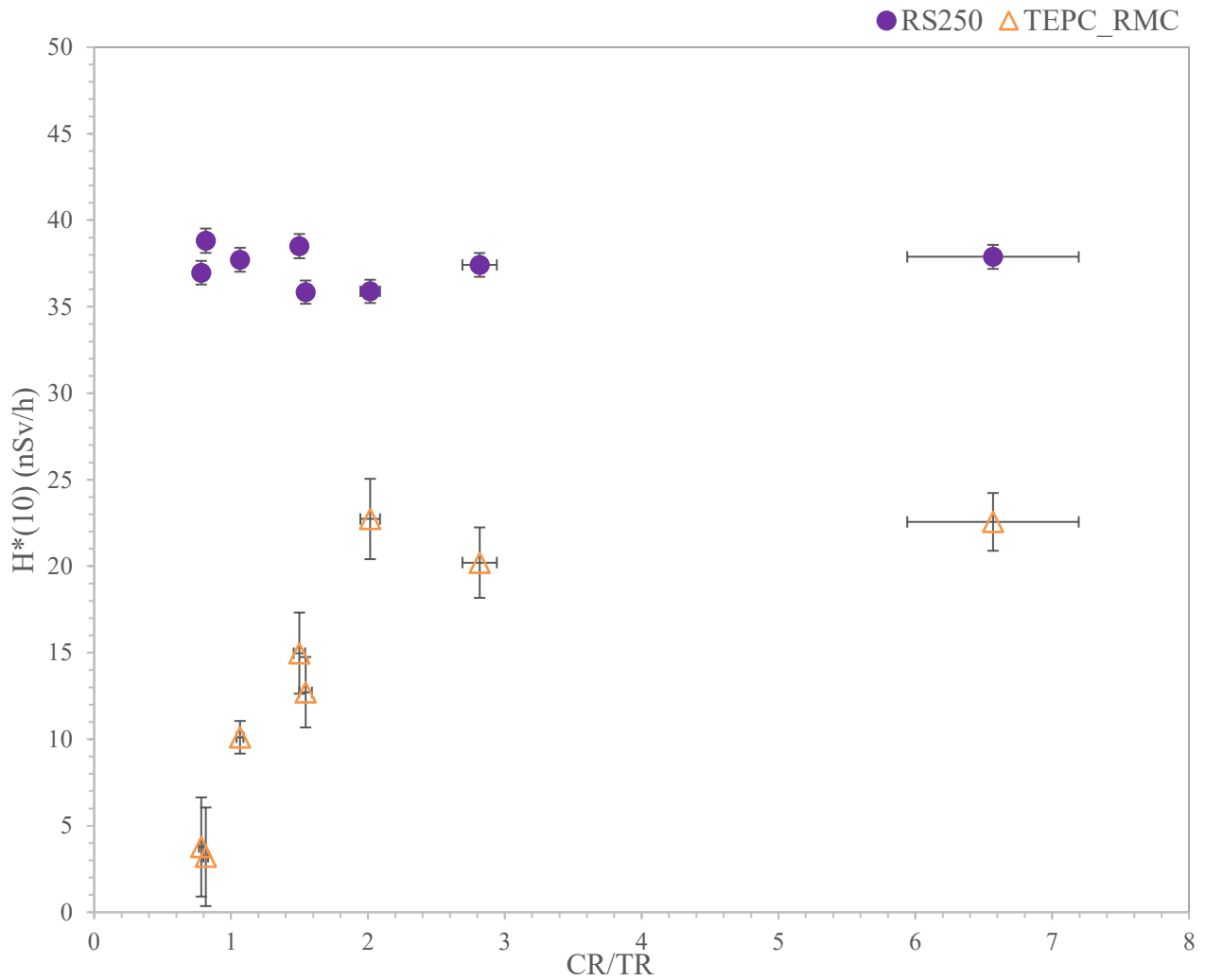


Figure 44. The comparison between experimental and analytical cosmic non-neutron  $H^*(10)$ s with respect to the changes along with the ratio of  $H^*(10)_{Non-n. CR}$  over  $H^*(10)_{TR}$ . Error bars represent the uncertainties on the dose ratios (CR/TR from RS250) at the 8 locations (x-axis) and  $H^*(10)$  (y-axis) from tables 18 and 19.

Compared to the analytical results obtained from RS250, all the cosmic  $H^*(10)$  including neutron by using the RMC method are high (Table 20, Figure 45 & 46). The experimental  $H^*(10)_{With-n. CR}^{TEPC, RMC}$  results are 49 % - 390 % higher than the analytical cosmic radiation doses.

Table 20. The summary of experimental  $H^*(10)$  contributed from cosmic radiation including neutron measured at 8 different locations using HAWK TEPC and the RMC method.

Date	Locations	$H^*(10)_{With-n. CR}^{TEPC, RMC}$ (nSv/h)	$\frac{\Delta H^*(10)_{With-n. CR}}{H^*(10)_{With-n. CR}^{RS250}}$
20210622	RPB	$177.2 \pm 3.2$	280 %
20200911	Britannia Beach (dock)	$150 \pm 11$	220 %
20210628	Walter Baker Park	$239 \pm 11$	390 %
20210803	Rideau Canal Narrows (Lock 35- dock)	$201 \pm 11$	310 %
20210803	Rideau Canal Narrows (Lock 35- park)	$149 \pm 10$	200 %
20200916	Ottawa River	$75.3 \pm 6.2$	49 %
20210703	Burnt Lands Provincial Park	$203.9 \pm 7.4$	290 %
20210629	Gatineau Park	$187.0 \pm 8.5$	260 %

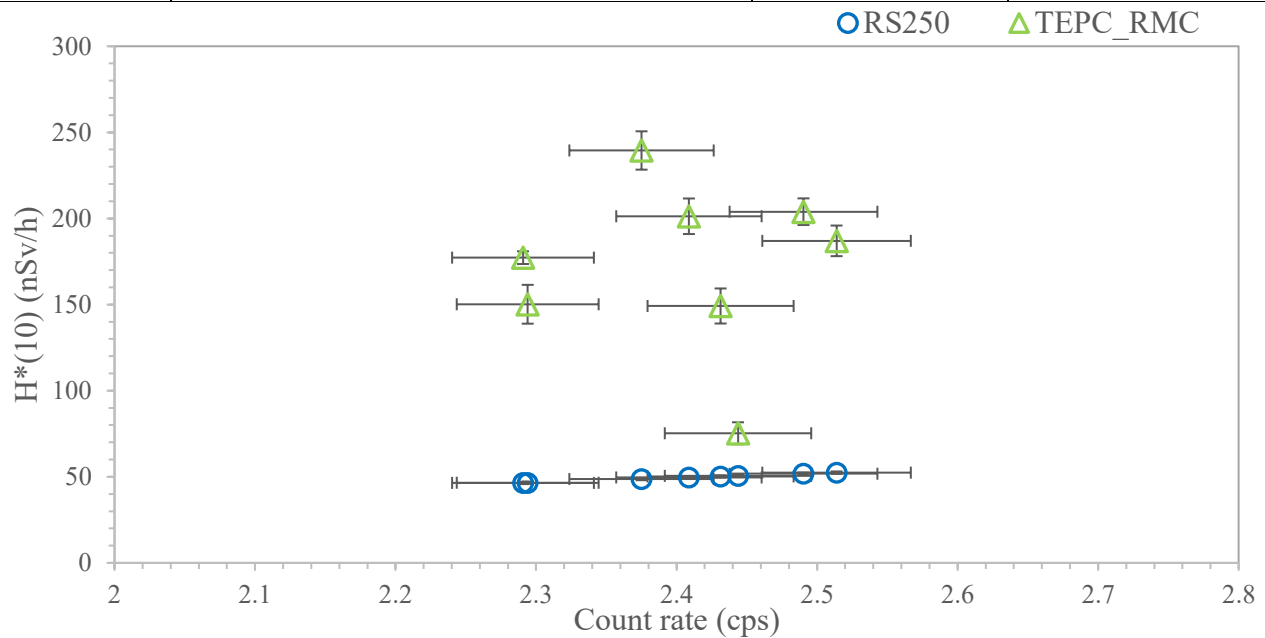


Figure 45. The comparison between experimental and analytical cosmic  $H^*(10)$ s (with neutron) along with the count rate of the CC channel in RS250. Error bars represent the uncertainties on

the RS250 CC count rates detected at the 8 locations (x-axis) and  $H^*(10)$  (y-axis) from tables 18 and 20.

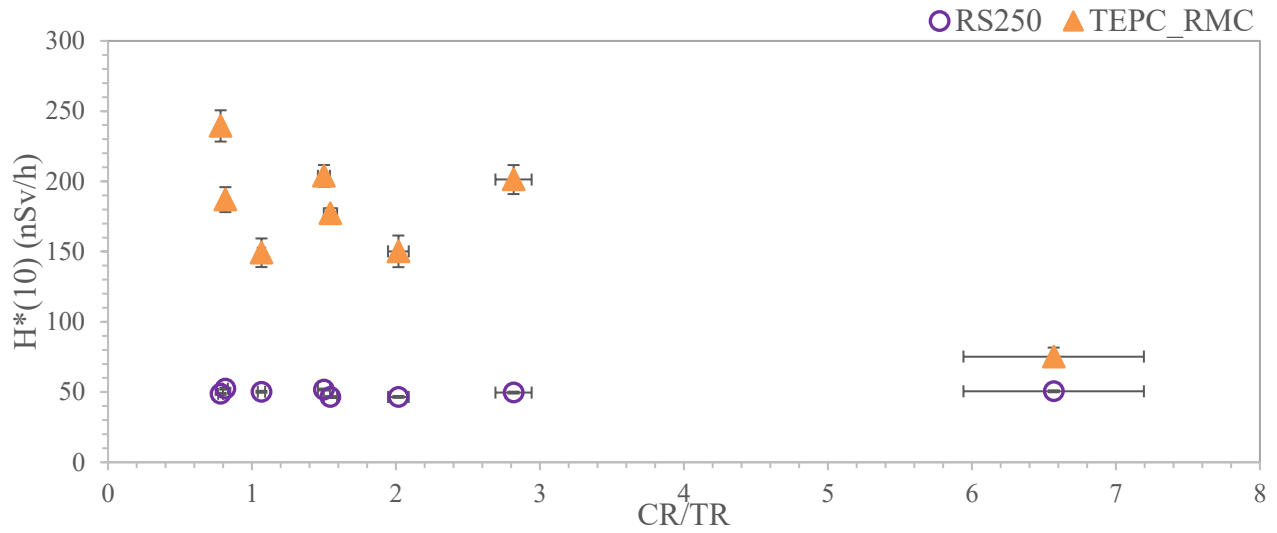


Figure 46. The comparison between experimental and analytical cosmic  $H^*(10)$ s with neutrons with respect to the changes along the ratio of  $H^*(10)_{With-n. CR}$  over  $H^*(10)_{TR}$ . Error bars represent the uncertainties on the dose ratios (CR/TR from RS250) at the 8 locations (x-axis) and  $H^*(10)$  (y-axis) from tables 18 and 20.

4.2.5 Results by Using MD-1 and MD-2 Methods

I. Non-neutron ambient dose equivalent

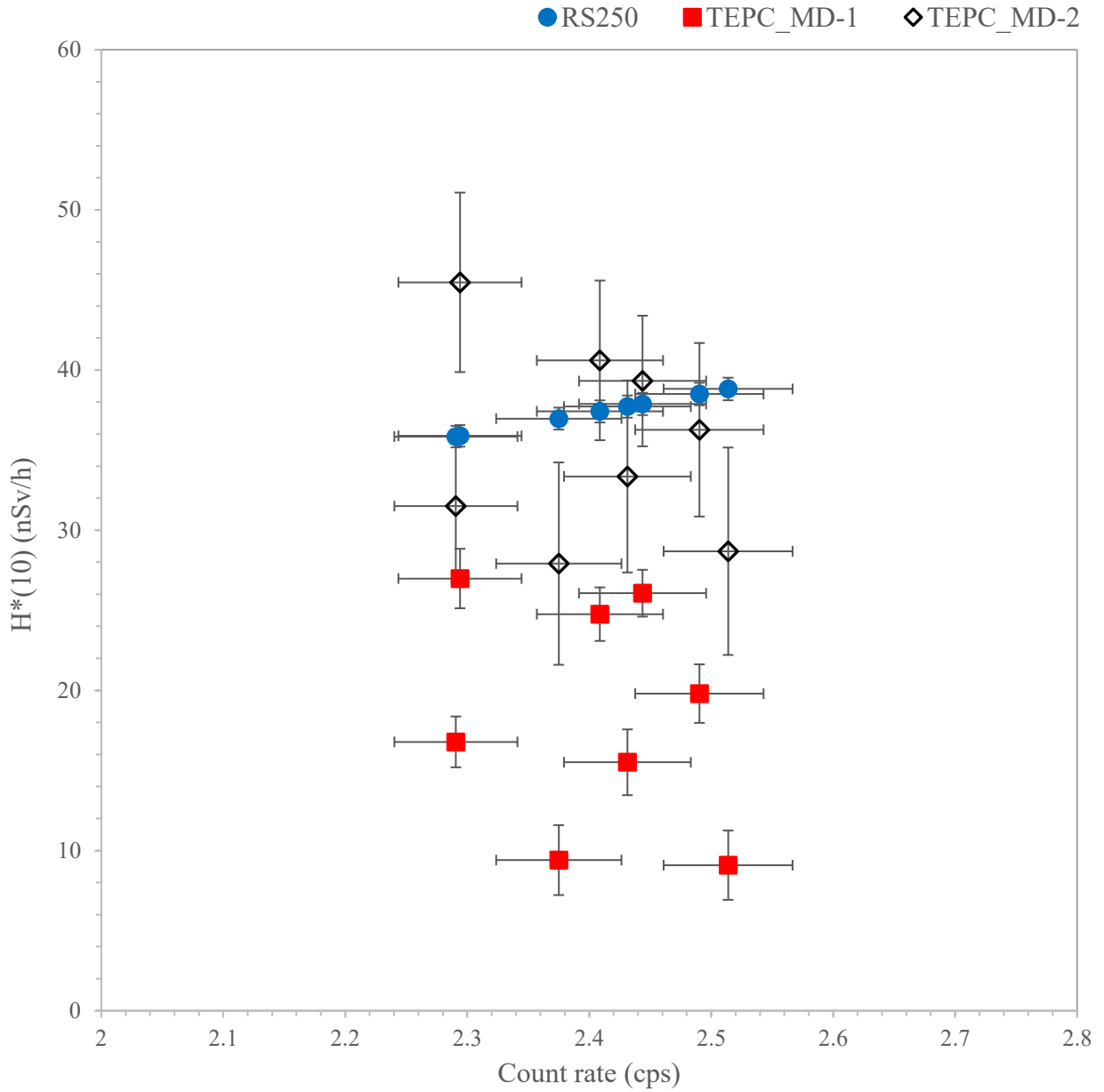


Figure 47. The comparison between experimental and analytical non-neutron cosmic  $H^*(10)$ s along with the count rate. Error bars represent the uncertainties on the RS250 CC count rates detected at the 8 locations (x-axis) and  $H^*(10)$  (y-axis) from tables 18, 21 and 22.

Figure 47 compares the changes in experimental (MD-1) and analytical cosmic non-neutron  $H^*(10)$ s over different CC count rates, where the maximum discrepancy (-76.6 %) between experimental (MD-1) and analytical results (RS250) occurs at  $2.514 \pm 0.053$  cps (Gatineau Park). The minimum discrepancy (-24.8 %) occurs at  $2.294 \pm 0.050$  cps (Britannia Beach). All the non-neutron cosmic  $H^*(10)$  results by using the MD-1 method are lower than the analytical dose results (Figure 47 & Table 21).

Table 21. The summary includes the experimental  $H^*(10)$  contributed from non-neutron cosmic radiation detected at 8 different locations with HAWK and analyzed by using MD-1, the discrepancies with the analytical dose results from RS250, and the slope used for extrapolation below the electronic threshold.

Date	Locations	Slope	$H^*(10)_{Non-n. CR}^{TEPC, MD1}$ (nSv/h)	$\frac{\Delta H^*(10)_{Non-n. CR}}{H^*(10)_{Non-n. CR}^{RS250}}$
20210622	RPB	$-2.435 \pm 0.011$	$16.79 \pm 0.68$	-53.2 %
20200911	Britannia Beach	$-2.435 \pm 0.011$	$27.0 \pm 1.0$	-24.8 %
20210628	Britannia Beach (dock)	$-2.435 \pm 0.011$	$9.40 \pm 0.90$	-74.6 %
20210803	Rideau Canal Narrows (Lock 35- dock)	$-2.435 \pm 0.011$	$24.76 \pm 0.81$	-33.8 %
20210803	Rideau Canal Narrows (Lock 35- park)	$-2.435 \pm 0.011$	$15.51 \pm 0.86$	-58.9 %
20200916	Ottawa River	$-2.435 \pm 0.011$	$26.07 \pm 0.92$	-31.2 %
20210703	Burnt Lands Provincial Park	$-2.435 \pm 0.011$	$19.80 \pm 0.76$	-48.6 %
20210629	Gatineau Park	$-2.435 \pm 0.011$	$9.09 \pm 0.85$	-76.6 %
Average				-50.2 %

Figure 47 also plots the experimental (MD-2) and analytical cosmic non-neutron  $H^*(10)$  versus the CC count rate, where the maximum discrepancy (26.7 %) between experimental (MD-2) and analytical results (RS250) occurs at  $2.294 \pm 0.050$  cps (Britannia Beach), and the minimum discrepancy (3.8 %) occurs at  $2.444 \pm 0.052$  cps (Centre of Ottawa River) (Table 18 & 22). The negative sign in the discrepancies indicates that the experimental  $H^*(10)$  measured by HAWK TEPC is bigger than the analytical dose results calculated from RS250.

Table 22. The summary includes the experimental  $H^*(10)$  contributed from non-neutron cosmic radiation detected at 8 different locations with HAWK and analyzed by using MD-2, the discrepancies with the analytical dose results from RS250, and the slope used for extrapolation below electronic threshold.

Date	Locations	Slope	$H^*(10)_{Non-n. CR}^{TEPC, MD2}$ (nSv/h)	$\frac{\Delta H^*(10)_{Non-n. CR}}{H^*(10)_{Non-n. CR}^{RS250}}$
20210622	RPB	$-2.389 \pm 0.035$	$30.58 \pm 0.68$	$-12.1 \%^{41}$
- 20200911	Britannia Beach (dock)	$-2.54 \pm 0.12$	$45.5 \pm 1.0$	26.7 %
20210628	Walter Baker Park	$-2.400 \pm 0.050$	$27.91 \pm 0.91$	-24.5 %
20210803	Rideau Canal Narrows (Lock 35- dock)	$-2.65 \pm 0.16$	$40.60 \pm 0.81$	8.5 %
20210803	Rideau Canal Narrows (Lock 35- park)	$-2.474 \pm 0.063$	$33.35 \pm 0.87$	-11.6 %
20200916	Ottawa River	$-2.65 \pm 0.17$	$39.31 \pm 0.93$	3.8 %
20210703	Burnt Lands Provincial Park	$-2.510 \pm 0.056$	$36.27 \pm 0.77$	-5.8 %
20210629	Gatineau Park	$-2.426 \pm 0.023$	$28.69 \pm 0.86$	-26.1 %
Average				14.9 %

<sup>41</sup> The negative sign indicates that the experimental  $H^*(10)$  measured by HAWK TEPC is smaller than the analytical dose results calculated from RS250.

The comparisons are also made in Figure 48 between the experimental (MD-1, MD-2) and analytical (RS250) cosmic non-neutron  $H^*(10)$ s along the ratio of CR/TR. It revealed that the discrepancy in  $H^*(10)$ s between MD-1 and RS250 increases as the  $H^*(10)$  ratio of CR to TR decreases, i.e., the proportion of CR's doses in the total natural doses decreases. In MD-2, the correlation between the  $H^*(10)$  and the CR to TR ratio is not very clear.

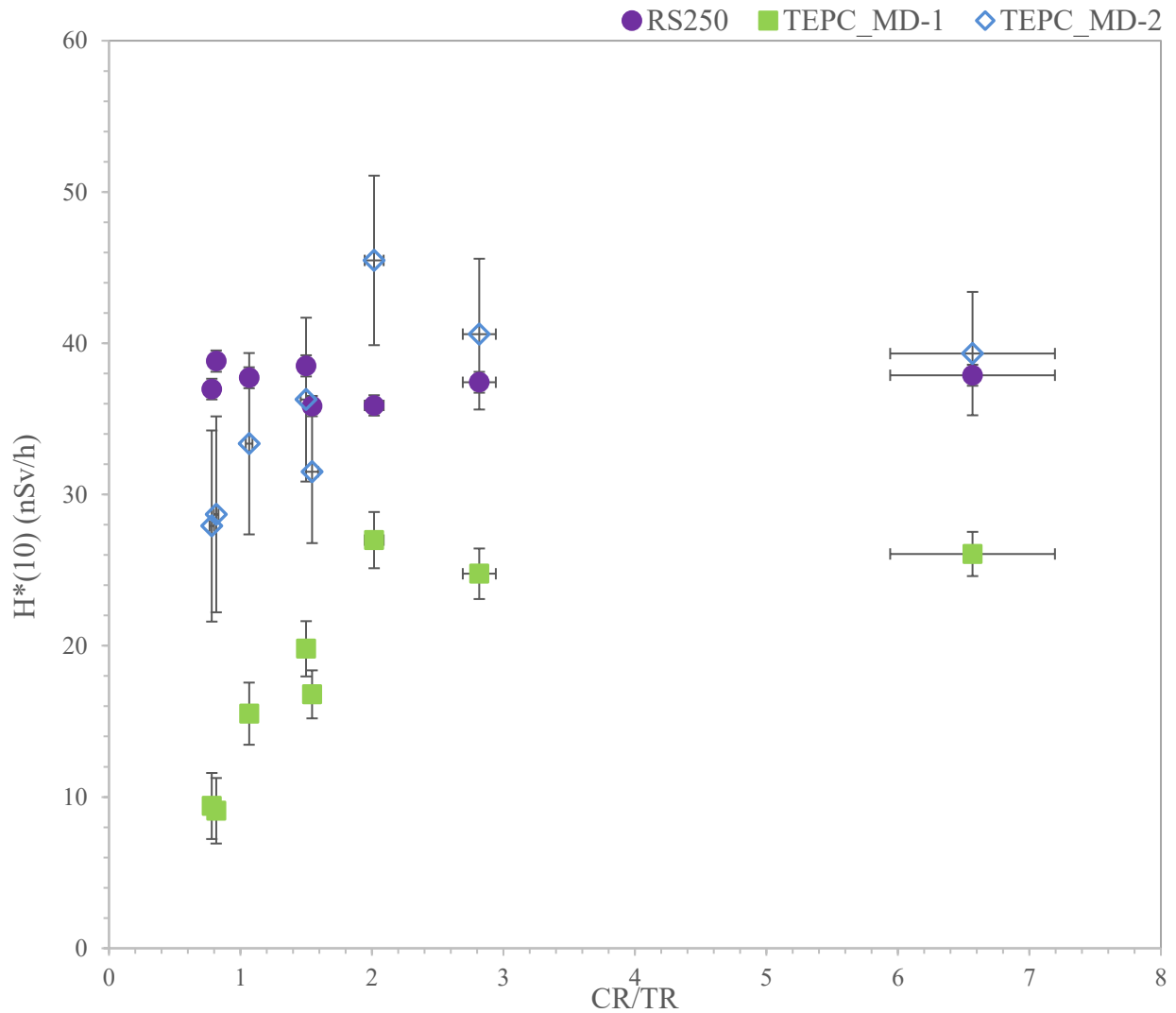


Figure 48. The comparison between experimental and analytical non-neutron cosmic  $H^*(10)$ s along with the ratio of  $H^*(10)_{Non-n. CR}$  over  $H^*(10)_{TR}$ . Error bars represent the uncertainties on the dose ratios (CR/TR from RS250) at the 8 locations (x-axis) and  $H^*(10)$  (y-axis) from tables 18, 21 and 22.

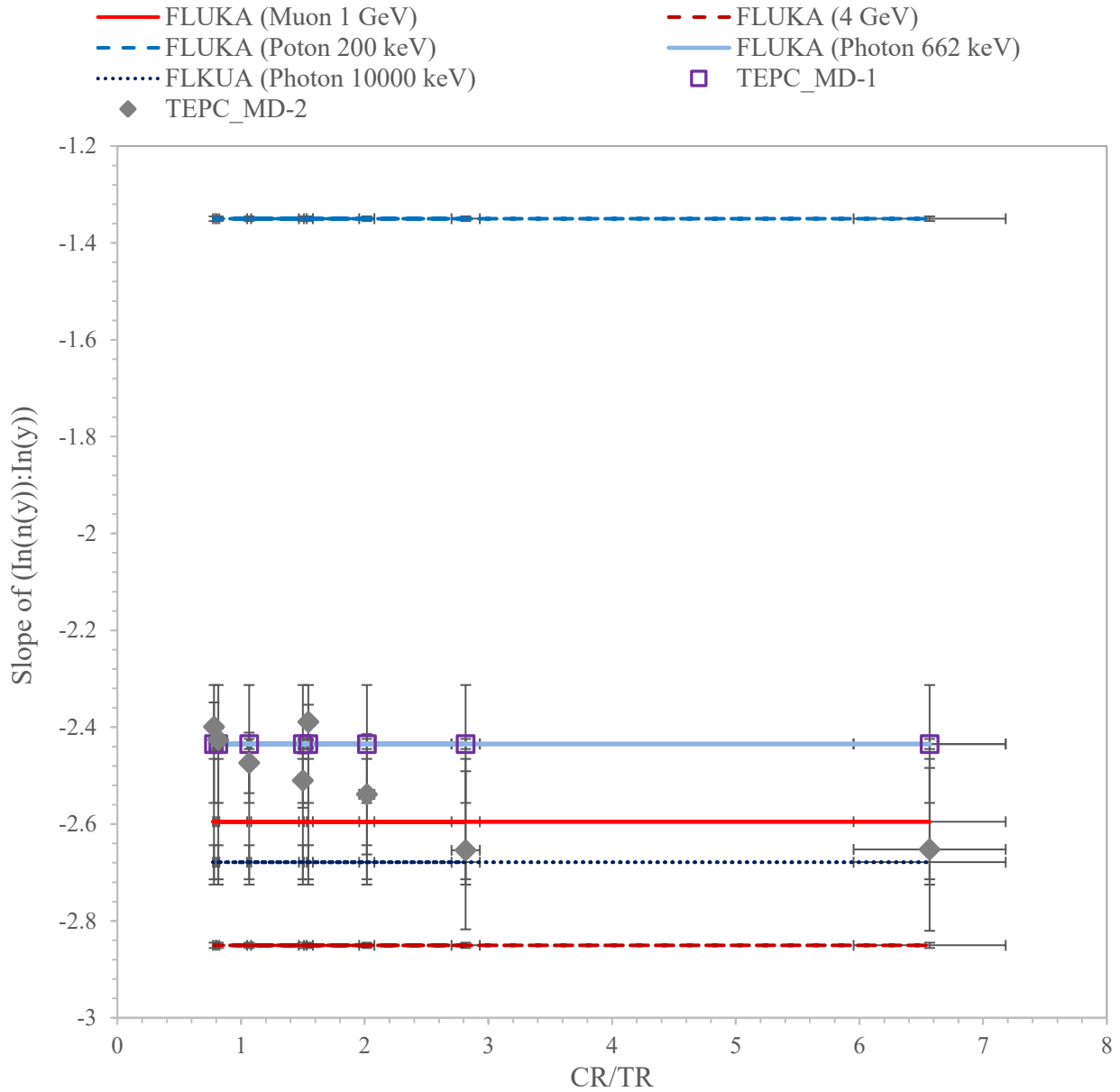


Figure 49. The slopes of the linear best fit equations from  $\ln(n(y))$  vs.  $\ln(y)$  spectra by using experimental measurements from HAWK (MD-1 & MD-2) and FLUKA simulation along with the different ratios of  $H^*(10)_{Non-n.CR}$  over  $H^*(10)_{TR}$ . Error bars represent the uncertainties on the dose ratios (CR/TR from RS250) (x-axis) and slopes ( $\ln(n(y))$  versus  $\ln(y)$  plots) (y-axis) from tables 18, 21 and 22.

Figure 49 visualizes and evaluates how well the extrapolation methods of MD-1 and MD-2 perform in different environment (i.e., different  $H^*(10)_{CR}^{RS250}/H^*(10)_{TR}^{RS250}$  ratio), by comparing the slopes of the linear best fit equations<sup>42</sup> from: 1. the measured  $\ln(\text{counts})$  distribution spectrum (i.e.,  $\ln(n(y))$  vs.  $\ln(y)$ ) and 2. the FLUKA simulated spectrum. The slopes of the linear best fit equation obtained from the simulated spectra (0.55 keV/ $\mu\text{m}$  down to 1.05 keV/ $\mu\text{m}$ ) by using the monoenergetic muons with 1 GeV and 4 GeV (kinetic energy) are  $-2.595 \pm 0.060$ , and  $-2.850 \pm 0.065$  respectively. The slopes of the linear best fit equation obtained from the simulated spectra by using the monoenergetic photons with 200 keV, 662 keV and 10000 keV (kinetic energy) are  $-1.350 \pm 0.083$ ,  $-2.390 \pm 0.010$  and  $-2.679 \pm 0.049$  respectively. The slope used in the MD-1 is constant in all locations, which is equivalent to the slope generated from the simulated photon (662 keV) spectrum. In MD-2, when the  $H^*(10)_{CR}^{RS250}/H^*(10)_{TR}^{RS250}$  gets bigger, the slope used in the MD-2 gets closer to the simulations, including photon with 10000 keV energy, muons with 1 GeV or 4 GeV kinetic energy (Figure 49 & Table 22).

---

<sup>42</sup> The linear best fit equations from 0.55 keV/ $\mu\text{m}$  and 1.05 keV/ $\mu\text{m}$ .

II. Ambient dose equivalent including neutron

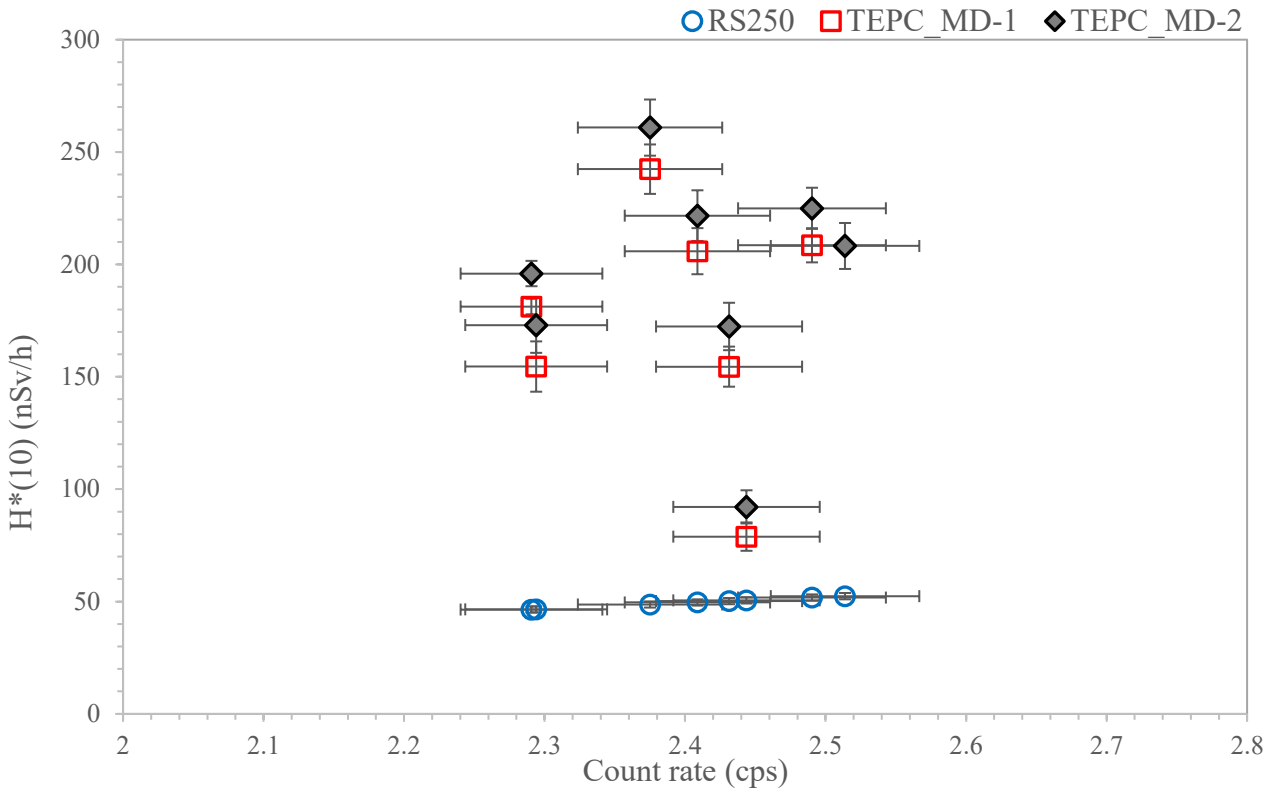


Figure 50. The comparison between experimental and analytical cosmic  $H^*(10)$ s (with neutron) along with the count rate. Error bars represent the uncertainties on the RS250 CC count rates detected at the 8 locations (x-axis) and  $H^*(10)$  (y-axis) from tables 18 and 23.

Table 23. The summary of experimental  $H^*(10)$  contributed from with-neutron cosmic radiation measured at 8 different locations by using HAWK TEPC and two different analysis methods (MD-1 & MD-2).

Date	Locations	$H^*(10)_{With-n. CR}^{RS250}$ (nSv/h)	$H^*(10)_{With-n. CR}^{TEPC}$ (nSv/h)	
			MD-1	MD-2
20210622	RPB	$46.4 \pm 1.3$	$181.3 \pm 3.2$	$195.9 \pm 3.2$
20200911	Britannia Beach	$46.5 \pm 1.3$	$155 \pm 11$	$173 \pm 11$
20210628	Walter Baker Park	$48.7 \pm 1.4$	$242 \pm 11$	$261 \pm 11$
20210803	Rideau Canal Narrows (Lock 35- dock)	$49.6 \pm 1.4$	$206 \pm 11$	$221 \pm 10$
20210803	Rideau Canal Narrows (Lock 35- park)	$50.2 \pm 1.4$	$154.5 \pm 8.7$	$172 \pm 10$
20200916	Ottawa River	$50.5 \pm 1.4$	$78.9 \pm 6.2$	$92.1 \pm 6.2$
20210703	Burnt Lands Provincial Park	$51.8 \pm 1.4$	$208.5 \pm 7.4$	$225.0 \pm 7.4$
20210629	Gatineau Park	$52.4 \pm 1.4$	$188.6 \pm 8.0$	$208 \pm 8.0$

Figure 50 and Table 23 show the comparison of cosmic  $H^*(10)$  including neutron from RS250, and HAWK (corrected by MD-1 & MD-2 methods). The experimental  $H^*(10)_{With\ n.\ CR}^{HAWK, MD1}$  and  $H^*(10)_{With\ n.\ CR}^{HAWK, MD2}$  results are much higher than the analytical  $H^*(10)_{With\ n.\ CR}^{RS250}$ . The discrepancy between the experimental and analytical dose results is the smallest, i.e., 56.2 % in MD-1 and 82.4 % in MD-2, at  $(2.444 \pm 0.052)$  cps (the centre of Ottawa river) with the highest CR/TR ratio  $(6.57 \pm 0.61)$  (Figure 51).

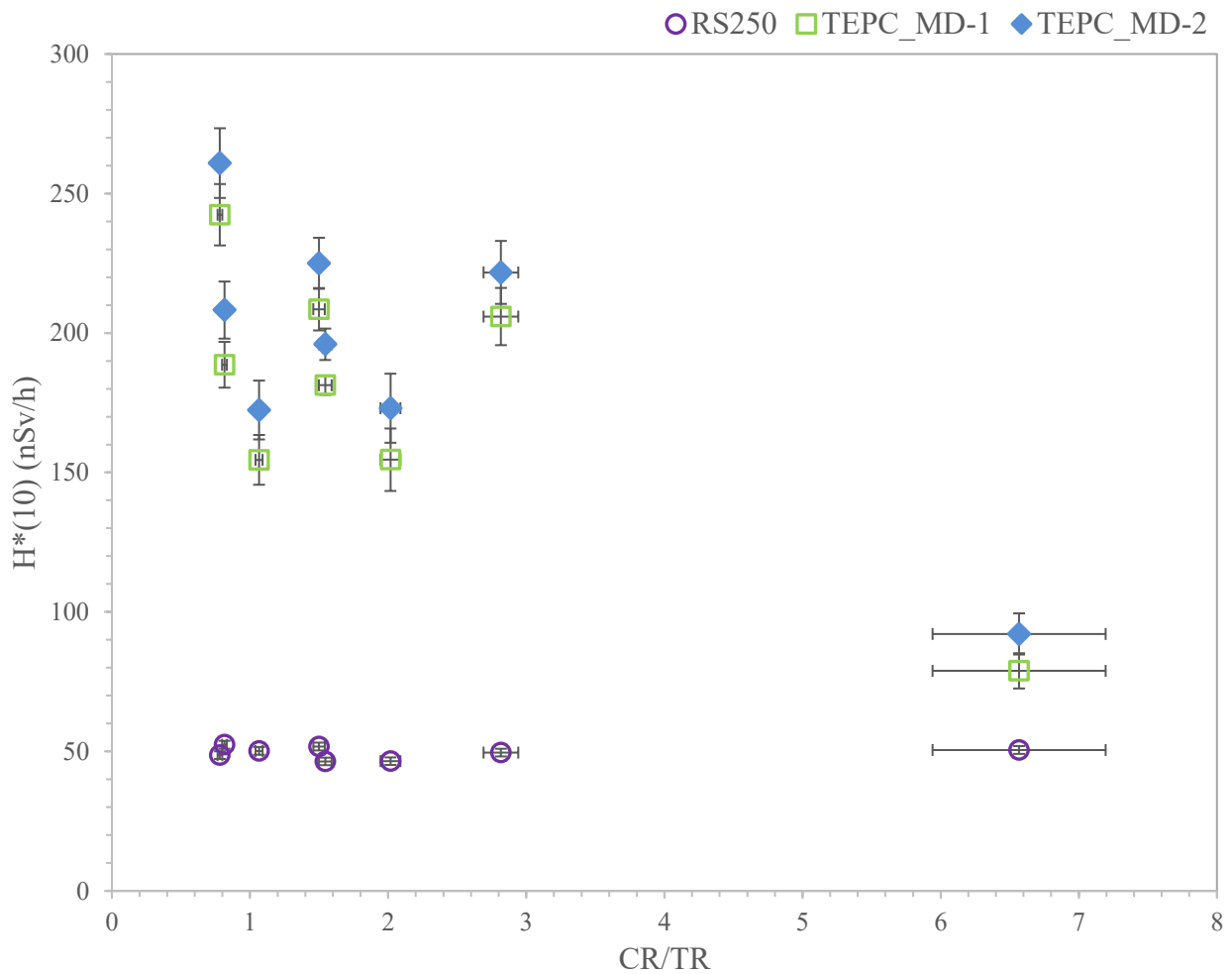


Figure 51. The comparison between experimental and analytical  $H^*(10)$ s along with the ratio of  $H^*(10)_{With\ n.\ CR}$  over  $H^*(10)_{TR}$ . Error bars represent the uncertainties on the dose ratios (CR/TR from RS250) at the 8 locations (x-axis) and  $H^*(10)$  (y-axis) from tables 18 and 23.

#### 4.2.6 Conclusion and Discussion

By employing the data analysis technique from RMC, all the cosmic non-neutron ambient dose equivalents are 36.7 % - 91.7 % lower than the analytical results calculated from the CC channel of RS250 (Table 19 & Figure 43). The underestimated  $H^*(10)$  results are mainly caused by the improper exploitation below the electronic low LET threshold. Because the non-neutron cosmic dose is largely contingent on the extrapolation method, the RMC method is unsuitable for the project.

The average discrepancy between  $H^*(10)_{Non-n. CR}^{RS250}$  and  $H^*(10)_{Non-n. CR}^{TEPC, MD1}$  is 50.2 %, with the maximum discrepancy (76.6 %) occurring at the highest count rate,  $(2.514 \pm 0.053)$  cps, which was measured at Gatineau Park (the highest altitude: 264 m); the minimum discrepancy (24.8 %) occurring at one of the lowest count rate,  $(2.294 \pm 0.050)$  cps, which was measured at the dock in the Britannia Beach Park (the second lowest altitude: 65 m) (Figure 47, Table 19 & 21). The average discrepancy between  $H^*(10)_{Non-n. CR}^{RS250}$  and  $H^*(10)_{Non-n. CR}^{TEPC, MD2}$  is 14.9 %, with the maximum discrepancy (26.7 %) occurring at one of the count rate,  $(2.294 \pm 0.050)$  cps, which was measured at Britannia Beach Park (the second lowest altitude: 65 m); the minimum discrepancy (3.8 %) occurring at the lowest count rate,  $(2.444 \pm 0.052)$  cps, which was measured at the centre of Ottawa river on Boat (the lowest altitude: 58 m) (Figure 47, Table 19 & 22). The results showed that the cosmic rays' dose changes relate to its altitude and geomagnetic latitude. The test conditions, including the geomagnetic and geographic features of the location, the temperature and temperature variation during the test period, humidity, play a role in interfering with the experimental results. It is possible to evaluate how these test conditions could impact the measurements in future project.

When plotting the experimental  $H^*(10)$  versus the ratio of ambient dose equivalents contributed from non-neutron cosmic radiation to terrestrial radiation ( $\frac{H^*(10)_{Non-n. CR}^{RS250}}{H^*(10)_{TR}^{RS250}}$ ), the difference in  $H^*(10)$ s between MD-1 and RS250 increases when the ratio decreases, i.e., the proportion of CR's doses among the total natural doses decreases (Figure 48). It also shows that the  $\Delta H^*(10)_{Non-n. CR}$ , i.e.,  $H^*(10)$ s by using MD-2 fluctuates around the results from RS250 as the CR to TR ratio changes.

Figure 49 provides a new way to evaluate the improved methods. Two conclusions can be drawn after comparing the slopes of the best linear fit equation from the  $\ln(n(y))$  vs.  $\ln(y)$  spectrum:

1. MD-1 cannot reflect the changes in the environment. Because in the extrapolation steps, MD-1 employs the simulated energy spectrum of 662 keV gamma rays, i.e., a fixed slope ( $-2.435 \pm 0.011$ ). As expected, the used in the MD-1 is always close to the one obtained from the simulated photon (662 keV) spectrum no matter how the proportion of the cosmic ray's dose changes in the environment.
2. MD-2 is a feasible method to indicate the changes in the radiation environment and adjust accordingly. Instead of a fixed slope, the slope used in MD-2, i.e., the slope of the best linear fit equation gained from the experimental measurements, changes when the proportion of the cosmic ray's dose changes in the natural environment. Figure 49 shows that the more the dose contributed from cosmic rays, the closer the slope in MD-2 gets to the one from simulated spectrum of high energy photon (10000 keV) and muons (1 GeV and 4 GeV). Equivalently, the MD-2 method is a good indicator of how the radiation

environment changes, i.e., more doses are contributed from muons (cosmic rays) or gamma rays (terrestrial radiation).

The dose equivalents from the natural radiation including neutron may be contaminated by the radiation from the surrounding environment and electronic noise in HAWKs. High noise level was observed in the high LET spectrum of HAWK, which is unavoidable in the natural background radiation measurements at ground level (i.e., relatively low radiation dose and count rate). The reasons that result in elevated cosmic neutron doses are still under investigation, hence this project focuses on the study of low LET spectra, i.e., the non-neutron spectra. The possibilities to improve the high LET results will be discussed in the next Chapter.

## 5 CONCLUSION AND DISCUSSION

---

This project employed a TEPC reference dosimeter to intercalibrate the RS250 cosmic ray dose estimate, which was obtained analytically from the CC channel. The initial goal was to calibrate RS250 with the reference instrument directly. However, it was realized that lots of works needed to be done before the field measurements to validate the performance of HAWK TEPC and correct the energy deposition events that cannot be detected due to electronic limitations. This chapter discusses the most significant accomplishments presented throughout this thesis and provides a general guideline for the improvements and corrections in the future.

Different HAWK data analysis methods have been studied and evaluated, including the RMC, MD-1 (i.e., simulated gamma spectra fit) and an improved method (i.e., MD-2). In MD-2, a new extrapolation method was developed below the electronic threshold (Section 3.3) which largely relies on the empirical slopes, which reflect the changes in the surrounding radiation environment. In addition, we adopted the advanced separation method between non-neutron and neutron spectra, which was applied in both MD-1 & MD-2 (Section 3.4). Compared to RMC and MD-1, MD-2 does a better job of reflecting the changes in the radiation environment and adjusting accordingly. A second reference instrument should be employed in the future to measure and evaluate MD-2. In Section 3.4, the method to separate the non-neutron and neutron spectrum is applicable and practicable. Approximately 1.1 % of the total dose contributed from non-neutron particles are found between  $9 \text{ keV}/\mu\text{m}$  and  $13 \text{ keV}/\mu\text{m}$  when measuring the natural background radiation dose at ground level.

A series of field trials with side-by-side measurements between HAWK and RS250 have been conducted in various environments, including over water, on the dock, and in local park etc. These field trials represent various situations of terrestrial and cosmic ray mixed fields, where the results can be used to test the independence of the comparison between HAWK and RS250. With these measurements, the maximum and minimum discrepancies in the ambient dose equivalents (non-neutron) between RS250 and HAWK with the MD-1 method are 76.6 % and 24.8 %, respectively. The HAWK non-neutron results with the MD-2 method are consistent with RS250 results with a smaller deviation at 26.7 % and 3.8 %, respectively (Section 4.2). According to ICRU (ICRU, 2010), the typical uncertainty combining the calibration uncertainty, the standard deviation, and uncertainty is usually around 15 to 30 %. In conclusion, the discrepancies obtained in this project using the TEPC\_MD-2 are within the acceptable range of uncertainty.

The source of Hawk measurement uncertainty and discrepancy between HAWK and RS250 can be from many aspects such as ambient dose equivalent conversion coefficients, extrapolation methods and RS250 estimation. The followings list these items that could cause a large difference and can be improved in future studies.

The ambient dose equivalent conversion coefficients employed in the project are the literature value published from RMC. Because the conversion coefficients depend on the method used to analyze the TEPC measurements, errors are introduced when different methods (i.e., MD-1 & MD-2) were applied. Section 4.1 shows a potential approach to determine the ambient dose

equivalent conversion coefficient. Improvements can be done on the conversion coefficient experiment to discover the conversion coefficients for MD-1 and MD-2, i.e., further collections on the experimental data to reduce the uncertainty.

In addition, the discrepancy between HAWK and RS250 can be possible contributed from the RS250 estimation. Uncertainty in the RS250 terrestrial dose rate (0-3 MeV) are introduced to the cosmic ray dose calculations. Equations 44 & 45 (Section 4.1) show that the RS250 terrestrial dose was subtracted from the HAWK total dose to get the cosmic ray dose. This uncertainty is minor because RS250 is precise in gamma ray dose detection with  $\pm 5\%$  uncertainty (Radiation solutions Inc. 2020). The analytical model is based on the CC channel of RS250 and EXPACS. It is reported that the doses calculated by EXPACS (PARMA) are consistent with the PHITS-based analytical radiation model in the atmosphere, which has been validated on simulating the cosmic-ray propagation in the atmosphere. The discrepancy in the results (doses) between the EXPACS PARMA and PHITS is 5 % (Sato, 2008).

All the ambient dose equivalent rates calculated from the high LET spectrum of HAWKs are extraordinarily high, compared to the literature values. The cosmic rays' ambient dose equivalents including contributions from neutron should be around  $40.0 \text{ nSv/h}$  in Ottawa (Grasty & LaMarre, 2004). These high values indicate the possible presence of systematic errors in the measurement. High-energy neutrons are rare to detect in a short period, i.e., there are less than 8 neutrons detected by HAWKs in one hour. The uncertainty of cosmic neutron dose measurement is very high with only a few hours of data collection. The current modes (MD-1 &

MD-2) are based on cosmic radiation measurements derived at the eight local sites and over a short sampling period (hours). A long term measurement experiment for several days or weeks could improve the results.

HAWK TEPC performs best at a constant temperature. If the operating temperature changes, i.e., temperature increases by 2°C-8°C when taking measurements in summer, it will affect the gamma counts around 0.5  $keV/\mu m$  to 1.5  $keV/\mu m$  (FWT, 2016). According to the Manufacturer (FWT, 2010), the uncertainty on dose is approximately  $\pm 5\%$  over a modest temperature range of 15°C to 35°C. Future works can be done to remove the temperature effects. For example, the counts may be corrected using a gaussian function to fit the data in the low LET spectrum.

The next step of the work will focus on developing coincidence experiments to detect the dose rate of cosmic muon. Because muon is dominant in the secondary cosmic rays, it is meaningful to study the dose contribution from cosmic muon. Previous research has done the coincidence experiment by using two BC408 plastic scintillators and one RS250 spectrometer by the RPB, it will be valuable to perform a similar experiment by employing BC408 and HAWK 3 (Figure 52) to obtain the BC408 spectrum, TEPC spectrum, a BC408-TEPC coincidence spectrum to find the counts rate and dose of cosmic muons.

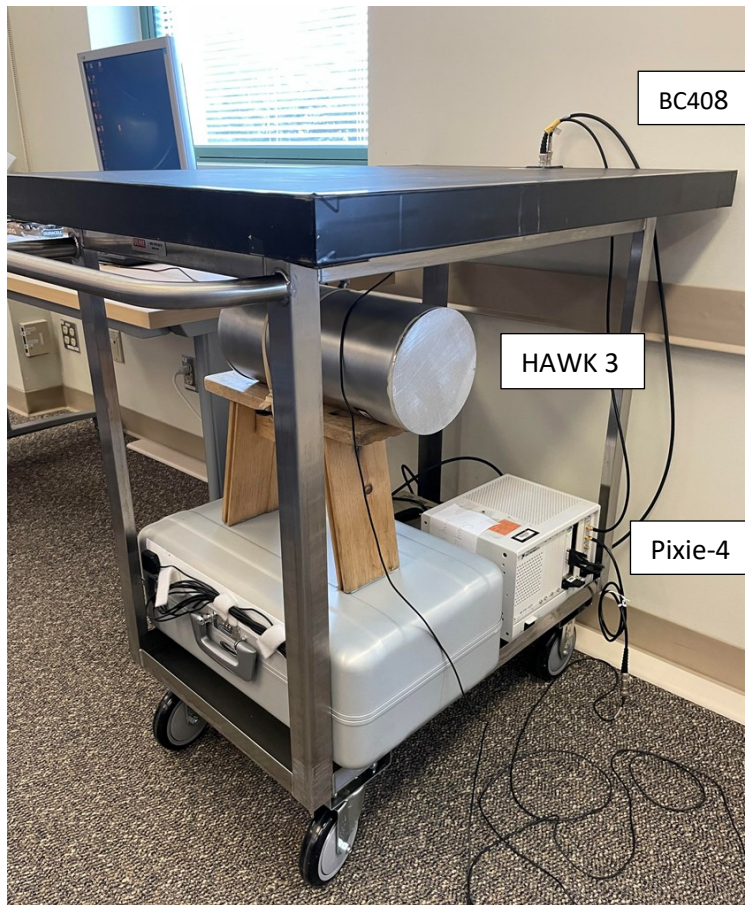


Figure 52. Experiment set-up using the BC408 scintillator, HAWK 3 the 4-channel all digital spectrometer Pixie-4.

Moreover, the project proposes a new method to determine the ambient dose equivalent conversion coefficient by using and comparing the field measurements from HAWK TEPC and RS250 NaI spectrometers (Section 4.1). The new method calculates the conversion coefficient by using the field measurements, i.e., the measurements from mixed Omni-direction radiation fields, rather than a point source in laboratory conditions which are very different from the natural radiation environments. A different reference instrument could be used in the future to calibrate RS250 and compare it to the ambient dose equivalent obtained from HAWK. The work will be further evaluated and applied to the other Fixed Point Surveillance (FPS) stations.

## REFERENCES

---

- Adams, D. A., Howell, L. W. et al. (2007). On the use of lineal energy measurements to estimate linear energy transfer spectra. NASA. Virginia Polytechnic Institute and State University, Blacksburg.
- Al-Bayati, S. N. (2012). The application of experimental microdosimetry to mixed-field neutron-gamma dosimetry. Oshawa: University of Ontario Institute of Technology.
- Ali, F. (2014). Design and characterization of next-generation tissue equivalent proportional counters for use in low energy neutron fields. Oshawa: University of Ontario Institute of Technology.
- Anjomani, Z. (2017). Development of a thick gas electron multiplier-based multi-element microdosimetric detector. McMaster University, Hamilton, Ontario.
- Atri, D., & Melott, A. L. (2013). Cosmic rays and terrestrial life: a brief review . *Astroparticle Physics* 53:, 186-190.
- Badavi, F. F., & Xapsos, M. A. (2009). An analytical model for the prediction of a microdosimeter response function. Christopher Newport University, 1-19.
- Bertolet, A., & Cortés-Giraldo, M. A. (2020). On the concepts of dose-mean lineal energy, unrestricted and restricted dose-averaged LET in proton therapy. *Phys. Med. Biol.*, 65 (2), 075011.
- Bianchi, A. (2017). Toward a novel simplified miniaturized microdosimeter for the clinical environment. University degli Studi di Padova. Anno Accademico.
- Bianchi, A., & Mazzucconi, D. (2021). Lineal energy calibration of a mini-TEPC via the proton edge technique. *Radiation measurement*. 141, 106526.
- Bohlen, T. T. (2014). The FLUKA code: developments and challenges for high energy and medical applications. *Nuclear Data sheets* 120, 211-214.
- Causey, O. I. (2018). Active tissue equivalent dosimeter: development of a dosimeter for the international space station. The Oklahoma State University.
- Chabot, G. (2015). NRC regulatory conference palisades nuclear plant. Effective dose equivalent external (EDEex). United States Nuclear Regulatory Commission.
- Chen, J. & Timmins, R. et al. (2009). An estimation of Canadian population exposure to cosmic rays. *Radiat. Environ. Biophys.* Vol. 48, pp. 317-322.

Colautti, P., & Magrin, G. e. (2020). Characterizing radiation effectiveness in ion-beam therapy part II: microdosimetric detectors. *Frontiers in Physics*. Vol. 8, 1-16.

Collums, T. L. (2012). Comparison of plastics used in tissue equivalent proportional counters (TEPC) and development of a balloon borne TEPC. Oklahoma State University.

Conecici, L. M. et al. (2017). Study of the shielding performances of different materials regarding Electromagnetic Field Interference. *IOP Conf. Ser.: Mater. Sci. Eng.* 200 012045

Cruz, G. A. S. (2016). Microdosimetry: principles and applications. *Reports of Practical Oncology and Radiotherapy*. Vol. 21, pp. 135-139.

Curtis, S. B. & Thomas, D. C. (1992). Effects of low dose and low dose rate radiation. *Advances in Radiation Biology*

Dawn, S., Chatterjee, S., et. al. (2021). Cosmic ray neutron spectrometry and dosimetry at high altitude research laboratory, Gulmarg, Kashmir, India. *Radiation Physics and Chemistry*, Vol. 185, 109523.

Delgado, A. (2001). 10th international congress of the international radiation protection association: mixed field dosimetry. IRPA, CIEMAT. Madrid. SPAIN: Avda Complutense 22,28040.

Ellaschuk, B. M. (2001). Measurement of cosmic radiation exposure to Canadian forces aircrew. Twenty Sixth Annual CNS-CAN Student Conference, Toronto, Ontario, Canada.

Endo, S., & Tanaka, K. (2009). Microdosimetry on a mini-reactor UTR-KINKI for educational uses and biological researches. *J. Radiat. Res.* Vol 50, pp. 83-87.

Fano, U. (1954). Note on the Bragg-Gray cavity principle for measuring energy dissipation. *Radiation Research* 1: 237-239.

Friedberg, W. & Copeland, K. (2011). Ionizing radiation in Earth's atmosphere and in space near earth. Federal Aviation Administration. Oklahoma City, OK 73125

FWT. (2010). Operations and repair manual: Model FWAD-2 & 3 Hawk version 2 & 3 environmental radiation monitor with 5" tissue equivalent proportional counter (TEPC). Far West Technology Inc.

FWT. (2011). A new method using Cs137 as the primary calibration source for the HAWK instrument. Far West Technology Inc.

FWT. (2016). Unit specific test document. Faw West Technology Inc.

Gelman, A. & Hill, J. (2007). Data analysis using regression and multilevel/hierarchical models. Cambridge University Press: Cambridge; New York, pp. 60-61.

- Gersey, B., & Wilkins, R. (2012). Tissue equivalent proportional counter microdosimetry measurements aboard high-altitude and commercial aircraft. 42nd International Conference on Environmental Systems (pp. AIAA 2012-3636). San Diego, California: American Institute of Aeronautics and Astronautics.
- Gluscock, M. D. (2014). Analytical geochemistry/ Inorganic INSTR. analysis. Treatise on Geochemistry. Elsevier Science.
- Grasty, R., & LaMarre, J. R. (2004). The annual effective dose from natural sources of ionising radiation in Canada. *Radiation Protection Dosimetry*, 108 (3), 215-266.
- Grieder, P.K.F., 2001. Cosmic rays at Earth. Elsevier Science, Amsterdam.
- Guinn, V. P. (2003). Radioactivity. *Encyclopedia of Physical Science and Technology*. Academic Press. Pp: 661-674.
- Health Canada. (2015). Special environmental radiation in Canada report on Fukushima accident contaminants. Ottawa: Radiation Protection Bureau.
- Hendry, J. H., & Brahme, A. (2014). *Comprehensive Biomedical Physics: radiation biology and radiation safety*. Elsevier B. V.
- ICRP. (1991). 1990 Recommendations of the international commission on radiological protection. ICRP Publication 60. *Ann. ICRP* (1-3).
- ICRP. (2016). As Endo on behalf of ICRU resport committee 26 on operational radiation protection quantities for external radiation: Operational quantities and new approach by ICRU. *Ann ICRP*.
- ICRP-103. (2007). The 2007 recommendations of the international commission on radiological protection. ICRP Publication 103. *Ann. ICRP* 37, 2-4.
- Knoll, G. F. (2010). *Radiation detection and measurement*. Hoboken, N. J. : Wiley & Sons.
- Leo, W. R. (1994). *Techniques for nuclear and particle physics experiments: a how-to approach*. Springer Berlin/ Heidelberg.
- Lewis, B. J. (1999). Cosmic radiation exposure on Canadian-based commercial airline routes. *Radiation Protection Dosimetry* 86 (1), 7-24.
- Lewis, B. J., & Desormeaux, M. et al. (2004). Assessment of aircrew radiation exposure by further measurements and model development. *Radiation protection dosimetry*. Vol. 111 (2), 151-171.
- Lillhok, J., & Beck, P. et al. (2007). A comparison of ambient dose equivalent meters and dose calculations at constant flight conditions. *Radiation Measurements*. Vol 42, pp. 323-333.

- Lindborg, L., & Kyllonen, J. E., et al. (1999). The use of TEPC for reference dosimetry. *Radiation Protection Dosimetry*. Nuclear Technology Publishing. Vol. 86 (4), pp. 285-288.
- Lindborg, L. & Waker, A. (2017). *Microdosimetry: experimental methods and applications*. CRC Press.
- Liu, C., & Zhang, W. et al. (2018). Development of a national cosmic ray dose monitoring system with Health Canada's fixed point surveillance network. *Journal of environmental radioactivity* 190-191, 31-38.
- Malimban, J. et al. (2019). Characterization of new tissue equivalent proportional counter for dosimetry of neutron and photon fields: comparison of measurements and monte carlo simulations. *Phys. Med. Biol.* 64.
- McCall, M. J. (2000). Development and validation of the predictive code for aircrew radiation exposure (PC-AIRE). National library of Canada: The Royal Military College of Canada.
- Mok, H. M., & Cheng, K. M. (2001). The day-night variation of cosmic rays intensity at sea level under the influence of meteorological fronts and troughs. Saiwanho Health Centre, HKSAR Government, China.
- Moro, D., & Chiriotti, S. (2015). Lineal energy calibration of a spherical TEPC. *Radiation Protection Dosimetry*. Vol. 166 (1-4), 233-237.
- Nakamura, T. (2008). Cosmic-ray neutron spectrometry and dosimetry. *Journal of Nuclear Science and Technology*, Supplement 5, p. 1-7.
- Nam, U., & Lim, C. H. et al. (2013). Development and characterization of tissue equivalent proportional counter for radiation monitoring in international space station. *J. Astron. Space Sci.* Vol. 30 (2), pp. 107-112.
- Northum, J. D. & Guetersloh, S. B. et al. (2012). FLUKA capabilities for microdosimetric analysis. *Radiation Research*. Vol. 177, pp. 117-123.
- Radiation solutions Inc. (2020). Gamma stationary monitoring system. Retrieved from [www.radiationsolutions.com](http://www.radiationsolutions.com)
- Rollet, S., & Autischer, M. et al. (2007). Measurement and simulation of lineal energy distribution at the CERN high energy facility with a tissue equivalent proportional counter. *Radiat. Prot. Dosimetry*. Vol. 125 (1-4), 425-428.
- Rossi, H. H., & Rosenzweig, W. (1955). A device for the measurement of dose as a function of specific ionization. *Radiology*, vol. 64, 404-411.

- Sato, T. (2015). Analytical model for estimating terrestrial cosmic ray fluxes nearly anytime and anywhere in the world: extension of PARMA/EXPACS. PLOS ONE 10(12), e0144679.
- Sato, T., & Yasuda, H. et al. (2008). Development of PARMA: PHITS-based analytical radiation model in the atmosphere. Radiation Research. Vol. (170), pp. 244-259.
- Sauli, F. (2014). Gaseous Radiation Detectors: Fundamentals and Applications (Cambridge Monographs on Particle Physics, Nuclear Physics and Cosmology). Cambridge: Cambridge University Press.
- Shahbazi-Gahrouei, D., Gholami, M. et al. (2013). A review on natural background radiation. Advanced Biomedical Research. Vol. 2 (1). Medknow Publications and Media Pvt. Ltd.
- Taylor, J. R. (1996). An Introduction to Error Analysis: The Study of Uncertainties in Physical Measurements. Sausalito, California: University Science Books.
- Taylor, G. C. & Bentley, R. D. (2002). The evaluation and use of a portable TEPC system for measuring in-flight exposure to cosmic radiation. Radiation Protection Dosimetry. Vol. 99 (1-4), pp. 435-8.
- Tsuboi, K., & Sakae, T., et al. (2020). Proton Beam Radiotherapy: Physics and Biology. Springer Nature Singapore Pte Ltd. Singapore.
- UN. (1966). Twenty-first session, supplement No. 14 (A/6314). In Reports of the United Nations scientific committee on the effects of atomic radiation. New York: United Nations.
- UNSCEAR. (2008). Sources and Effects of Ionizing Radiation: United Nations: United Nations scientific committee on the effects of atomic radiation 2008 report. New York: United Nations.
- Vasconcelos, F. (2019). Poisson statistics. MIT Department of Physics.
- Wijesinghe, P. I. (2007). Energy deposition study of low-energy cosmic radiation at sea level. Department of Physics and Astronomy, Georgia State University.
- Wissmann, et al. (2004). A mobile TEPC-based system to measure the contributions to  $H^*(10)$  at flight altitudes. Radiation Protection Dosimetry 110 (1-4), 347-9.
- Wissmann, F. (2006). Long-Term measurements of  $H^*(10)$  at aviation altitudes in the northern hemisphere. Radiation Protection Dosimetry. Vol. 121 (4), pp. 347-357.
- Zeb, J. & Arshed, W. et al. (2007). Radiation dose reduction by water shield. Radiation protection and dosimetry. Vol. 40 (2), pp. 1-32.
- Ziegler, J. F. (1996). Terrestrial cosmic rays. IBM. J. RES. DEVELOP. Vol. 40 (1), 19-39.
- Zyla, P. A. (2020). PDG Cosmic rays. Prog. Theor. Exp. Phys., 083C01.

Zylaet P.A. al.(Particle Data Group) (2020). Prog. Theor. Exp. Phys.2020, 083C01

## APPENDICES

### Appendix A. HAWK 3 Lineal Energy Calibration Results

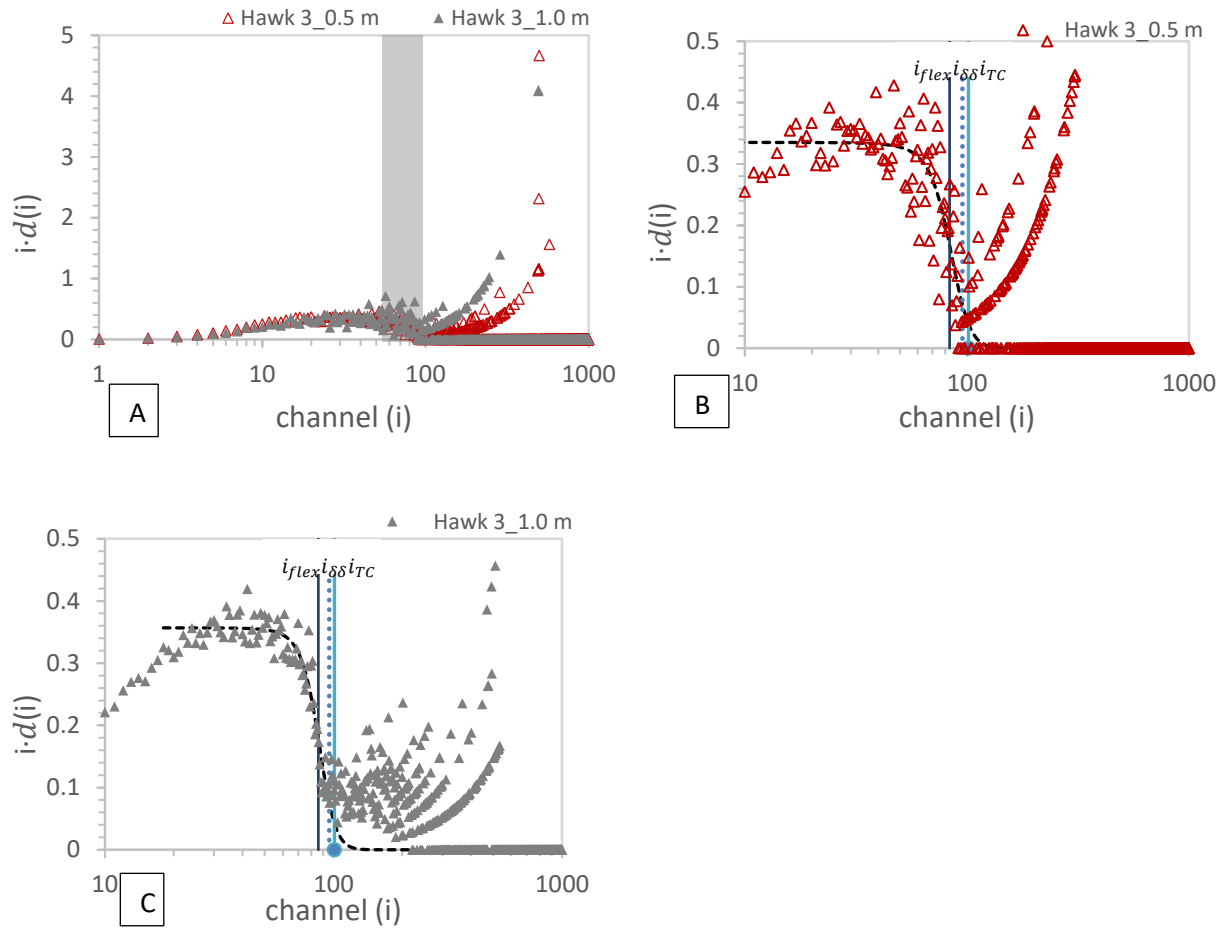


Figure 53. The *AmBe* high LET spectrum measured from the HAWK 2 at site size  $D = 2 \mu\text{m}$ .

The HAWK 3 detector was placed 0.5 m (B) and 1.0 m (C) away from the neutron source, the corresponding measurements were labelled by red and grey triangles respectively. The proton edge region is highlighted by grey. The dashed line represents the Fermi-like function fitted to the measured data. (B): The fitting range is from channel 23-110, Correlation = 0.88, RSME = 0.062. (C): The fitting range is from channel 32-135, Correlation = 0.94, RSME = 0.041.

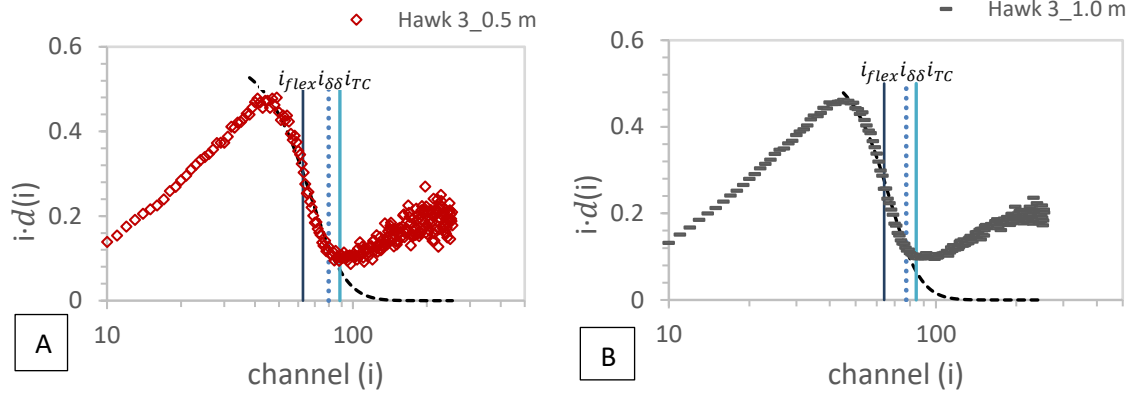


Figure 54. The  $AmBe$  low LET spectrum measured from the HAWK 2 at site size  $D = 2 \mu m$ .

The HAWK 3 detector was placed 0.5 m (A) and 1.0 m (B) away from the neutron source, the corresponding measurements were labelled by red and grey rectangles respectively. The proton edge region is highlighted by grey. The dashed line represents the Fermi-like function fitted to the measured data. (A): The fitting range is from channel 42-92, Correlation = 0.99, RSME = 0.025. (B): The fitting range is from channel 42-92, Correlation = 0.99, RSME = 0.025.

## Appendix B. Additional Experimental Results

Table 24. The summary of the dose equivalent rates (H) calculated from the FLUKA spectra by using the simulated data and RMC; the percentage differences between the raw FLUKA doses and the results after extrapolations.

FLUKA mixed spectra $\mu: \gamma$	H (nSv/h)		% difference <sup>43</sup>
	FLUKA	RMC	
1:20	55.78 ± 0.49	33.19 ± 0.47	-40.5
1:10	51.22 ± 0.46	28.82 ± 0.43	-43.7
1:8	50.32 ± 0.45	27.92 ± 0.42	-44.5
1:6	49.42 ± 0.44	26.98 ± 0.41	-45.4
1:4	48.54 ± 0.43	26.21 ± 0.40	-46.0
1:2	47.72 ± 0.41	24.95 ± 0.39	-47.7
1:1	47.38 ± 0.41	24.32 ± 0.38	-48.7
2:1	94.64 ± 0.57	47.82 ± 0.53	-49.5
4:1	189.68 ± 0.79	94.49 ± 0.74	-50.2
6:1	285.18 ± 0.96	140.94 ± 0.89	-50.6
8:1	381.0 ± 1.1	187.3 ± 1.0	-50.8
10:1	477.2 ± 1.2	233.5 ± 1.1	-51.1
20:1	961.6 ± 1.7	464.0 ± 1.6	-51.7
Average			47.7

<sup>43</sup> The percentage difference is calculated by using the difference in dose equivalents between the result after applying the extrapolation correction method of RMC and the simulated dose results divided by the simulated results.

Table 25. The ratios of ambient dose equivalents contributed from non-neutron cosmic radiation to terrestrial radiation ( $\frac{H^*(10)_{Non-n. CR}}{H^*(10)_{TR}^{RS250}}$ ).

Date	Locations	CR/TR Ratio		
		$\frac{H^*(10)_{Non-n. CR}^{RS250}}{H^*(10)_{TR}^{RS250}}$	$\frac{H^*(10)_{Non-n. CR}^{TEPC, MD1}}{H^*(10)_{TR}^{RS250}}$	$\frac{H^*(10)_{Non-n. CR}^{TEPC, MD2}}{H^*(10)_{TR}^{RS250}}$
20210622	RPB	1.544 ± 0.036	0.723 ± 0.070	1.36 ± 0.21
20200911	Britannia Beach	2.017 ± 0.061	1.52 ± 0.11	2.56 ± 0.32
20210628	Walter Baker Park	0.7821 ± 0.0089	0.199 ± 0.046	0.59 ± 0.13
20210803	Rideau Canal Narrows (Lock 35- dock)	2.82 ± 0.11	1.86 ± 0.15	3.06 ± 0.40
20210803	Rideau Canal Narrows (Lock 35- park)	1.066 ± 0.016	0.438 ± 0.058	0.94 ± 0.17
20200916	Ottawa River	6.57 ± 0.61	4.52 ± 0.49	6.82 ± 0.95
20210703	Burnt Lands Provincial Park	1.500 ± 0.032	0.771 ± 0.073	1.41 ± 0.21
20210629	Gatineau Park	0.815 ± 0.010	0.191 ± 0.046	0.60 ± 0.14

Table 26. The summary including the experimental  $H^*(10)$  contributed from cosmic radiation including neutron measured at 8 different locations with HAWK and analyzed by using MD-1, the discrepancies with respect to the analytical dose results from RS250, and the slope used for extrapolation below electronic threshold.

Date	Locations	Slope	$H^*(10)_{With\ n.\ CR}^{TEPC,\ MD1}$ (nSv/h)	$\frac{\Delta H^*(10)_{With\ n.\ CR}}{H^*(10)_{RS250\ With\ n.\ CR}}$
20210622	RPB	$-2.435 \pm 0.011$	$181.3 \pm 3.5$	290 %
20200911	Britannia Beach	$-2.435 \pm 0.011$	$155 \pm 11$	232 %
20210628	Britannia Beach (dock)	$-2.435 \pm 0.011$	$242 \pm 11$	398 %
20210803	Rideau Canal Narrows (Lock 35- dock)	$-2.435 \pm 0.011$	$205.9 \pm 8.9$	315 %
20210803	Rideau Canal Narrows (Lock 35- park)	$-2.435 \pm 0.011$	$154.5 \pm 8.9$	208 %
20200916	Ottawa River	$-2.435 \pm 0.011$	$78.9 \pm 6.3$	56.1 %
20210703	Burnt Lands Provincial Park	$-2.435 \pm 0.011$	$208.5 \pm 7.6$	303 %
20210629	Gatineau Park	$-2.435 \pm 0.011$	$188.6 \pm 8.2$	260 %

Table 27. The summary including the experimental  $H^*(10)$  contributed from cosmic radiation including neutron measured at 8 different locations with HAWK and analyzed by using MD-2, the discrepancies with respect to the analytical dose results from RS250, and the slope used for extrapolation below electronic threshold.

Date	Locations	Slope	$H^*(10)_{With\ n.\ CR}^{TEPC, MD2}$ (nSv/h)	$\frac{\Delta H^*(10)_{With\ n.\ CR}}{H^*(10)_{RS250\ With\ n.\ CR}}$
20210622	RPB	$-2.435 \pm 0.011$	$195.9 \pm 5.6$	322 %
20200911	Britannia Beach	$-2.435 \pm 0.011$	$173 \pm 12$	272 %
20210628	Britannia Beach (dock)	$-2.435 \pm 0.011$	$261 \pm 12$	436 %
20210803	Rideau Canal Narrows (Lock 35- dock)	$-2.435 \pm 0.011$	$222 \pm 11$	347 %
20210803	Rideau Canal Narrows (Lock 35- park)	$-2.435 \pm 0.011$	$172 \pm 11$	243 %
20200916	Ottawa River	$-2.435 \pm 0.011$	$92.1 \pm 704$	82.3 %
20210703	Burnt Lands Provincial Park	$-2.435 \pm 0.011$	$225.0 \pm 9.2$	335 %
20210629	Gatineau Park	$-2.435 \pm 0.011$	$208 \pm 10$	297 %

Appendix C. Data analysis worksheet (RMC)

1	Name	Hawk_2_Dock_RMC	min		Low LET/High Gain		Low LET/lineal energy		adjusted		adjusted		HI LET/High Gain
2	Duration	HI LET 1.5keVum	keVum	low LET ch	Chn# (Low LET ch)	y/(keVum)	counts (n)	y/(n)	y/(n)	n/(y)	Chn# (HI LET ch)		
3					0	0.05	0	0	0	0	0	0	
4	Crossover	channel	21.75	218	1	0.15	0	0	0	759.55	5063.667	1	
5	low LET	sum up to	21.75	15570	2	0.25	12	3	3	759.55	3038.2	2	
6	high LET	sum up to	21.75	15570	3	0.35	4943	1730.05	2170.143	759.55	3038.2	3	
7	Quantities	Total Cts=	33497.89841	0	4	0.45	4297	1933.65	759.55	1687.889	4	4	
8	All total counts	Sum y(n)	1445.8	0	5	0.55	1381	759.55	759.55	1381	5	5	
9		Sum y^2(n)	278728.125	0	6	0.65	920	598	598	920	6	6	
10	mean y	yfbar=Sum(y)/Total Counts=	0.430349386	0	7	0.75	657	492.75	492.75	657	7	7	
11	mean dose	ydbar=Sum(y^2(n))/(Sum(y))=	19.3349051	0	8	0.85	438	423.3	423.3	438	8	8	
12	absorbed dose	D=0.204*Sum(y(n))/(27e5*2)=	1.82331E-07	0	9	0.95	282	296.1	296.1	282	9	9	
13	dose equivalent	H=0.204*Sum(y(n))/(27e5*2)=	8.44562E-07	0	10	1.05	247	284.05	284.05	247	10	10	
14	mean Q	Q=H/D=	4.632015384	0	11	1.15	181	226.25	226.25	181	11	11	
15	counts rate	sum/duration	185.0712519	cpm	12	1.25	106	174.9	174.9	106	12	12	
16	bsobed dose rat	sum/duration	60.44134908	nGy/h	13	1.35	141	204.45	204.45	141	13	13	
17	dose equiv rate	sum/duration	279.9652588	nSv/h	14	1.45	156	210.6	210.6	156	14	14	
18	pure dose equiv rate				15	1.55	126	195.3	195.3	126	15	15	
19					16	1.65	106	174.9	174.9	106	16	16	
20					17	1.75	100	175	175	100	17	17	
21					18	1.85	117	216.45	216.45	117	18	18	
22					19	1.95	76	148.2	148.2	76	19	19	
23					20	2.05	70	143.5	143.5	70	20	20	
24	Gamma Quantities	Total Cts=	33463.99841	0	21	2.15	48	103.2	103.2	48	21	21	
25	All total counts	Sum y(n)	11976.4	0	22	2.25	51	114.75	114.75	51	22	22	
26		Sum y^2(n)	20003.88	0	23	2.35	43	101.05	101.05	43	23	23	
27	mean y	yfbar=Sum(y)/Total Counts=	0.357890181	0	24	2.45	48	117.6	117.6	48	24	24	
28	mean dose	ydbar=Sum(y^2(n))/(Sum(y))=	1.387635789	0	25	2.55	39	99.45	99.45	39	25	25	
29	absorbed dose	D=0.204*Sum(y(n))/(27e5*2)=	1.51478E-07	0	26	2.65	30	79.5	79.5	30	26	26	
30	dose equivalent	H=0.204*Sum(y(n))/(27e5*2)=	1.51508E-07	0	27	2.75	23	91.2	91.2	23	27	27	
31	mean Q	Q=H/D=	1.000198065	0	28	2.85	20	59	59	20	28	28	
32	counts rate	sum/duration	184.8834166	cpm	29	2.95	15	125.05	125.05	15	29	29	
33	bsobed dose rat	sum/duration	50.21363873	nGy/h	30	3.05	11	72.45	72.45	11	30	30	
34	dose equiv rate	sum/duration	50.22358431	nSv/h	31	3.15	23	72.45	72.45	23	31	31	
35					32	3.25	31	100.75	100.75	31	32	32	
36					33	3.35	27	90.45	90.45	27	33	33	
37					34	3.45	29	100.05	100.05	29	34	34	
38					35	3.55	21	74.55	74.55	21	35	35	
39	neutron Quantities	Total Cts=	34	0	36	3.65	26	97.5	97.5	26	36	36	
40	All total counts	Sum y(n)	2439.4	0	37	3.75	21	76.65	76.65	21	37	37	
41		Sum y^2(n)	258724.245	0	38	3.85	18	63.3	63.3	18	38	38	
42	mean y	yfbar=Sum(y)/Total Counts=	71.74705882	0	39	3.95	16	63.2	63.2	16	39	39	
43	mean dose	ydbar=Sum(y^2(n))/(Sum(y))=	17.947269332	0	40	4.05	25	101.25	101.25	25	40	40	
44	absorbed dose	D=0.204*Sum(y(n))/(27e5*2)=	3.08536E-08	0	41	4.15	16	66.4	66.4	16	41	41	
45	dose equivalent	H=0.204*Sum(y(n))/(27e5*2)=	6.93054E-07	0	42	4.25	22	93.5	93.5	22	42	42	
46	mean Q	Q=H/D=	22.46266921	0	43	4.35	15	65.25	65.25	15	43	43	
47	counts rate	sum/duration	0.187845304	cpm	44	4.45	18	84.55	84.55	18	44	44	
48	bsobed dose rat	sum/duration	10.222771036	nGy/h	45	4.55	11	51.15	51.15	11	45	45	
49	dose equiv rate	sum/duration	229.7416745	nSv/h	46	4.65	7	33.95	33.95	7	46	46	
50					47	4.75	15	71.25	71.25	15	47	47	
51					48	4.85	7	33.95	33.95	7	48	48	
52					49	4.95	11	54.45	54.45	11	49	49	
53					50								
54					51								
55					52								

	HI LET lineal energy	counts (n)	lineal energy Y (keV/um)	total counts (n)	*dy*	14415.8	8.468	26.55399	19.3349051
	Y (keV/um)		Y (keV/um)	counts (n)	f(y)=Cts/ dy*Total	ln(y)	d(y)=y/f(y)/ Ybar	yd(y)	yd(y)dy
1									
2									
3									
4									
5	0.75	0	0.05	15191	4.534913359	759.55	0.526887	0.026344	0.002634436
6	2.25	118	0.15	5063.666667	1.51163712	759.55	0.526887	0.079033	0.007903307
7	3.75	13712	0.25	3038.2	0.906982272	759.55	0.526887	0.131722	0.013172179
8	5.25	1353	0.35	2170.142857	0.64784448	759.55	0.526887	0.184411	0.018441051
9	6.75	342	0.45	1687.888889	0.50387904	759.55	0.526887	0.237099	0.023709922
10	8.25	39	0.55	1381	0.412264669	759.55	0.526887	0.289788	0.028978794
11	9.75	3	0.65	920	0.274644095	598	0.414823	0.269635	0.026963471
12	11.25	3	0.75	657	0.196131707	492.75	0.341812	0.256359	0.025635934
13	12.75	0	0.85	498	0.148666043	423.3	0.293636	0.249591	0.024959073
14	14.25	0	0.95	360	0.107469429	342	0.23724	0.225378	0.022537771
15	15.75	0	1.05	282	0.084184386	296.1	0.2054	0.21567	0.021566961
16	17.25	0	1.15	247	0.073735969	284.05	0.197041	0.226597	0.022659686
17	18.75	0	1.25	181	0.05403324	226.25	0.156946	0.196182	0.019618231
18	20.25	0	1.35	156	0.046570086	210.6	0.14609	0.197221	0.019722211
19	21.75	0	1.45	141	0.042092193	204.45	0.141824	0.205644	0.020564415
20	23.25	0	1.55	126	0.0376143	195.3	0.135476	0.209988	0.020998835
21	24.75	0	1.65	106	0.031643776	174.9	0.121325	0.200187	0.02001866
22	26.25	0	1.75	100	0.029852619	175	0.121395	0.212441	0.021244052
23	27.75	2	1.85	117	0.034927564	216.45	0.150148	0.277773	0.027777335
24	29.25	1	1.95	76	0.02268799	148.2	0.102804	0.200468	0.020046754
25	30.75	0	2.05	70	0.020896833	143.5	0.099544	0.204064	0.020406429
26	32.25	0	2.15	48	0.014329257	103.2	0.071588	0.153914	0.015391445
27	33.75	0	2.25	51	0.015224836	114.75	0.0796	0.1791	0.017910036
28	35.25	0	2.35	43	0.012836626	101.05	0.070097	0.164727	0.016472724
29	36.75	0	2.45	48	0.014329257	117.6	0.081577	0.199864	0.019986404
30	38.25	3	2.55	39	0.011642521	99.45	0.068987	0.175916	0.017591636
31	39.75	0	2.65	30	0.008955786	79.5	0.055148	0.146142	0.014614173
32	41.25	0	2.75	37	0.011045469	101.75	0.070582	0.194101	0.019410126
33	42.75	0	2.85	32	0.009552838	91.2	0.063264	0.180302	0.018030217
34	44.25	2	2.95	20	0.005970524	59	0.040927	0.120736	0.012073558
35	45.75	1	3.05	41	0.012239574	125.05	0.086745	0.264573	0.026457255
36	47.25	1	3.15	23	0.006866102	72.45	0.050257	0.158311	0.015831067
37	48.75	1	3.25	31	0.009254312	100.75	0.069889	0.227138	0.022713793
38	50.25	1	3.35	27	0.008060207	90.45	0.062744	0.210191	0.021019125
39	51.75	0	3.45	29	0.00865726	100.05	0.069403	0.23944	0.023944041
40	53.25	0	3.55	21	0.00626905	74.55	0.051714	0.183585	0.018358502
41	54.75	0	3.65	21	0.00626905	76.65	0.053171	0.194074	0.019407352
42	56.25	0	3.75	26	0.007761681	97.5	0.067634	0.253628	0.025362796
43	57.75	0	3.85	18	0.005573471	69.3	0.048072	0.185078	0.018507818
44	59.25	1	3.95	16	0.004776419	63.2	0.043841	0.173171	0.01731711

